

Oxide dispersion, microstructure, texture and radiation stability of high Cr ODS alloys

By

Sumita Santra

Enrolment No.: PHYS02 2011 04 012

Indira Gandhi Centre for Atomic Research, Kalpakkam, India.

A thesis submitted to

The Board of Studies in Physical Sciences

In partial fulfillment of requirements for the Degree of

**DOCTOR OF PHILOSOPHY
Of
HOMI BHABHA NATIONAL INSTITUTE**

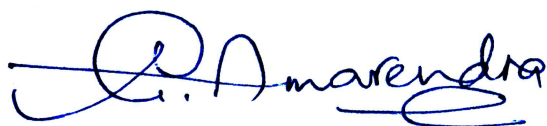


February 2020

Homi Bhabha National Institute

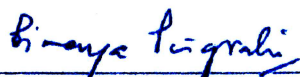
Recommendations of the Viva Voce Committee

As members of the Viva Voce Committee, we certify that we have read the dissertation prepared by Sumita Santra entitled "Oxide dispersion, microstructure, texture and radiation stability of high Cr ODS alloys" and recommend that it may be accepted as fulfilling the thesis requirement for the award of Degree of Doctor of Philosophy.



Chairman: Dr. G. Amarendra

Date: April 7, 2021



Guide/ Convener: Dr. B.K. Panigrahi

Date: 7-04-2021

by VC for R. Raj 07/04/2021

External Examiner: Prof. D. C. Kothari

Date:



Member 1: Dr. Arup Dasgupta

Date: 07/04/2021



Member 2: Dr. S. Amirthapandian

Date: 7-04-2021



Member 3: Dr. B. Sundaravel


Date: 7/04/2021

Final approval and acceptance of this thesis is contingent upon the candidate's submission of the final copies of the thesis to HBNI.

I hereby certify that, I have read this thesis prepared under my direction and recommend that it may be accepted as fulfilling the thesis requirement.

Date: 7-04-2021

Place: Kalpakkam



Dr. B. K. Panigrahi

(Guide)

Statement by Author

This dissertation has been submitted in partial fulfillment of requirements for an advanced degree at Homi Bhabha National Institute (HBNI) and is deposited in the Library to be made available to borrowers under rules of the HBNI.

Brief quotations from this dissertation are allowable without special permission, provided that accurate acknowledgement of source is made. Requests for permission for extended quotation from or reproduction of this manuscript in whole or in part may be granted by the Competent Authority of HBNI when in his or her judgment the proposed use of the material is in the interests of scholarship. In all other instances, however, permission must be obtained from the author.

Date: 20/02/2020

Place: Hyderabad


(Sumita Santra)

Declaration

I, hereby declare that the investigation presented in the thesis has been carried out by me. The work is original and has not been submitted earlier as a whole or in part for a degree / diploma at this or any other Institution / University.


(Sumita Santra)

List of Publications

(a) Journal

1. *Effect of Ti and Cr on dispersion, structure and composition of oxide nano particles in model ODS alloys*, A. J. London, **S. Santra**, S. Amirthapandian, B.K. Panigrahi, R.M. Sarguna, S. Balaji, R. Vijay, C.S. Sundar, S. Lozano-Pereza, C.R.M. Grovenor, *Acta Materialia* 97 (2015) 223-233
2. *Ion irradiation stability of oxide nano particles in ODS alloys: TEM Studies*, **Sumita Santra**, Amirthapandian, S. Balaji, B. K. Panigrahi, Yves Serruys, C. Robertson, *Journal of Nuclear Materials*, in press (2019), <https://doi.org/10.1016/j.jnucmat.2019.151861>

(b) Conferences:

1. *Effect Of Displacement Damage On The Stability Of Oxide Nanoparticles In Model ODS Alloys: TEM Studies*, **Sumita Santra**, S. Balaji, B. K. Panigrahi, Yves Serruys, C. Robertson, Alamo Ana, C. S. Sundar : AIP conference proceedings **1447**, 1315 (2012)
2. *Comparison of atom probe tomography and transmission electron microscopy analysis of oxide dispersion strengthened steels*, A. J. London, S. Lozano-Perez, **S. Santra**, S. Amirthapandian, B.K. Panigrahi, C.S. Sundar and CRM Grovenor, Electron Microscopy and Analysis Group Conference 2013 (EMAG2013), *Journal of Physics: Conference Series* 522 (2014) 012028
3. *TEM studies on the refinement of particle size in model Oxide Dispersion Strengthened Alloys*, **Sumita Santra**, S. Balaji, B. K. Panigrahi, C. Robertson, S. Amirthapandian, R. Vijay, C. S. Sundar. International Conference on Nano Science and Technology (ICONSAT), 20th – 23rd January, 2012, ARCI, Hyderabad, India (Oral presentation)
4. *Comparison of Atom Probe Tomography and Transmission electron Microscopy Analysis of Oxide Dispersion Strengthened Steels*, A. London, P. Bagot, **S. Santra**, S. Amirthapandian, B. K. panigrahi, C. S. Sundar and C. R. M. Grovenor. 53rd International Field Emission Society 2012 (IFES2012) Field Emission Symposium, May 21-25, 2012, University of Alabama, USA (Poster presentation)
5. *TEM investigation on ion irradiation stability of oxide nano particles in model ODS alloys*, **Sumita Santra**, S. Amirthapandian, S. Balaji, B. K. Panigrahi, Yves Serruys, C. Robertson C. S. Sundar Swift Heavy Ions in materials engineering and characterisatiobn (SHIMEC), 9th – 12th October, 2012, IUAC, New Delhi, India (Poster presentation)
6. *TEM investigation on irradiation stability of oxide nano particles in model ODS alloy Fe-14Cr- 0.2 Ti-0.3 Y₂O₃*, **Sumita Santra**, S. Amirthapandian, S. Balaji, B. K. Panigrahi, Yves Serruys, C. Robertson, C. S. Sundar, *The Materials Research*

Society of India (MRSI), 11th – 13th February, 2013, IGCAR, Kalpakkam, India
(Poster presentation)

7. *TEM and nano indentation Studies of dual beam irradiated ODS alloys*, B. K. Panigrahi, **Sumita Santra**, S. Amirthapandian, S. Balaji, Yves Serruys, C. Robertson, C. S. Sundar, IAEA 56th General Conference, 17th – 21st September, 2012, Vienna International Centre, Vienna (Poster presentation)
8. *Irradiation stability of oxide nano particles in model ODS alloys Fe-0.2Ti-0.3Y₂O₃, Fe-14Cr-0.2Ti-0.3 Y₂O₃*, S. Amirthapandian, **Sumita Santra**, S. Balaji, B. K. Panigrahi, C. S. Sundar, International Conference on Electron Microscopy and the XXXIV Annual Meeting of the Electron Microscope Society of India (EMSI), 3rd – 5th July, 2013, SINP, Kolkata, India (Poster presentation)
9. *Synergistic effect of cold work and annealing temperature in texture of 18-Cr ODS*, **Sumita Santra**, S. V. Ramana Rao, and Komal Kapoor, 12th Asia-Pacific Microscopy Conference (APMC-2020) and 40th AGM meeting of EMSI, 3rd-7th February, 2020, HICC, Hyderabad, India (Oral presentation)



Sumita Santra

*I dedicate this thesis to my son Swaprabho, my husband Sanway and my
guide Dr. B. K. Panigrahi*

Acknowledgements

First and foremost, I take this opportunity to thank my guide Dr. B. K. Panigrahi for his motivation, constant support and encouragement. I want to convey my heartfelt thanks to him for guiding me with the possibilities of accomplishing this thesis even when I could not think it possible anymore. I feel gratitude for all the quality time that he has spent for designing my research program and correcting the manuscripts with extreme care in spite of his busy schedule.

I am very much grateful to Dr. S. Amirthapandian for introducing me to the transmission electron microscopy technique that has been the indispensable part for materializing this thesis. I am grateful for all his advices and guidance throughout my research career and help to wade through the tough times of pursuing research. His advices were very much valuable for completion of my synopsis as well as publishing the manuscripts.

I thank Dr. Gurpreet Kaur for all her help and guidance in completion of my synopsis and helping me submit all documents to HBNI in time.

I thank Dr. P. Jegadeesan for all his help that has accelerated my thesis writing process and helped me a lot during modification of the thesis with all corrections.

I am extremely thankful to Dr. R. Vijay, ARCI for providing all the ODS samples studied in this thesis and express my gratitude to Mr. M. Ramakrishna for assisting with EELS measurements for probing thickness of the irradiated samples.

I thank Mr. Sanway Deb for carrying out the vacuum annealing of the ODS samples.

I express special thanks to Dr. Komal Kapoor and Shri S. V. Ramana Rao for providing me 18 Cr ODS samples for study and helping me with the EBSD facility.

I express my gratitude to Dr. Manikrishna, BARC for helping me understanding the misorientation relationship between deformed matrix and nucleus for studying the texture evolution.

I am grateful to Dr. Arup Dasgupta and Dr. Chanchal Ghosh for their valuable teachings which have helped me a lot to learn and use transmission electron microscopy technique.

I sincerely thank Dr. G. Amarendra, chairman, for his encouragement and constant support.


Sumita Santra

Table of contents

List of Publications	v
<i>Acknowledgements</i>	viii
Abstract	x
Table of contents	xiii
List of Figures	xvi
List of tables	xx

Chapter 1 Introduction 1

1.1. Background	1
1.2. Concept of Generation IV Reactors	1
1.3. Materials Development	2
1.4. Radiation Damage	5
1.4.1. Displacement damage	5
1.4.2. Formation of transmutation products	9
1.5. Radiation effects	9
1.5.1. Irradiation Creep & Growth	10
1.5.2. Helium Embrittlement	10
1.5.3. Void Swelling	11
1.5.4. Irradiation hardening	12
1.6. Alloy Design with alloying additions	12
1.6.1. Yttria and Titanium	12
1.6.2. Tungsten	13
1.6.3. Aluminum and zirconium	13
1.6.4. Chromium	13
1.7. Texture	14
1.7.1. Representation of Texture	15
1.7.1.1. Pole Figure	15
1.7.1.2. Orientation Distribution Function (ODF)	17
• Euler Angles	18
1.8. Motivation	20

Chapter 2 Experimental..... 25

2.1. Materials	25
2.1.1. Fabrication Process	25
2.2. Methods	27
2.2.1. Sample Preparation	27
2.2.1.1. 18 Cr ODS	27
2.2.1.2. Model ODS alloys	27

2.2.2. Field Emission Gun Scanning Electron Microscopy (FEGSEM) and Electron Back Scattered Diffraction (EBSD).....	28
2.2.3. Transmission electron microscopy (TEM).....	31
2.2.4. Vickers Hardness Test.....	32
2.2.5. SRIM (Kinchin Pease to NRT consideration in TRIM) for irradiation damage study.....	33
2.2.6. Ion irradiation facility: JANNuS	35
2.2.7. Cold Rolling	36
2.2.8. Vacuum annealing.....	37

Chapter 3 Study of microstructure and texture in high Cr ODS alloys38

3.1. Introduction.....	38
3.2. Experimental.....	38
3.3. Results.....	40
3.3.1. Model ODS alloys.....	40
3.3.1.1. Hardness study.....	40
3.3.1.2. Microstructure and recrystallization	41
3.3.1.3. Texture study	44
3.3.2. Commercial 18Cr ODS Alloy	46
3.3.2.1. Hardness Study	46
3.3.2.2. Effect of cold work and annealing temperature.....	48
3.3.2.3. Effect of cold work and annealing temperature on texture.....	56
3.4. Discussion.....	63
3.4.1. Model ODS Alloys.....	63
3.4.2. 18 Cr-ODS Alloy	63
3.5. Conclusions.....	67

Chapter 4 Role of Cr and Ti in oxide particle dispersion, crystal structure and composition of ODS Alloys68

4.1. Introduction.....	68
4.2. Experimental.....	69
4.3. Results.....	70
4.3.1. Effect of alloying element in particle size distribution	70
4.3.2. Effect of alloying element in crystal structure of oxide nano particles..	73
4.4. Discussion.....	77
4.5. Conclusion	79

Chapter 5 Irradiation response of the nano-particles in Fe-0.2Ti-0.3Y₂O₃ and Fe-14Cr-0.2Ti-0.3Y₂O₃ ODS Alloys.....81

5.1. Introduction.....	81
5.2. Experimental.....	83

5.3. Results.....	85
5.4. Discussion.....	91
5.4.1. Stability of particles.....	91
5.4.2. Effect of Alloying element in particle dissolution process	95
5.5. Conclusions.....	96
Chapter 6 Summary and scope for future work.....	97
6.1. Summary	97
6.2. Scope for future work	99
References	102

List of Figures

Figure 1.1	Maximum hoop deformation of different grades of austenitic Phénix claddings and ferrite-martensitic materials versus dose at temperatures between 400 °C and 550 °C [11].	4
Figure 1.2	Comparison between a Fe-18Cr conventional alloy and a Fe-18Cr ODS alloy during a creep test at 650 °C and 180 MPa. The rupture time is below 10 min for the non-reinforced material against few thousands of hours for the ODS one [21].	4
Figure 1.3	Vacancies and self-interstitial atoms in a cascade generated by neutron irradiation [9].	5
Figure 1.4	Typical energy loss behavior of ions with respect to energy in solid [32]	7
Figure 1.5	Difference in damage morphology, displacement efficiency (ϵ) and average recoil energy (T) for 1MeV particles of different type incident on nickel [35]	8
Figure 1.6	Secondary defects formed from clustered irradiation-induced primary defects [9].	11
Figure 1.7	Fe-Cr Binary phase diagram [www.calphad.com]	13
Figure 1.8	(a) Grains are crystallographically similarly arranged, (b) grains are crystallographically differently arranged, and (c) some grains are crystallographically similarly and some are differently arranged [56].	15
Figure 1.9	Schematic showing construction of a (100) pole figure [56]	16
Figure 1.10	(001) Pole figure showing (110) fiber along (a) ND, (b) RD, (c) TD and (d) typical texture fibers in fcc and bcc materials[59]	17
Figure 1.11	Orientation of the crystal axis system (X_{ci}) and the sample axis system {RD, TD, ND}; s is the intersection of the planes (RD–TD) and ([100]–[010]) [63].	18
Figure 1.12	Definition of Euler angles, ϕ_1 , Φ and ϕ_2 , in Bunge convention [64].	19
Figure 1.13	Representation of Euler space with Euler angles showing Various fibre textures that are of relevance for rolling and annealing textures in fcc and bcc alloys [65].	19
Figure 1.14	Some ideal orientations used for texture description in cubic materials plotted in ϕ_2 =constant sections of the Euler space [66].	20
Figure 2.1	ODS Alloy tube manufacturing process [20]	26
Figure 2.2	TEM sample preparation process [89].	28
Figure 2.3	Set-up and principle of data acquisition for EBSD measurement in a polycrystalline material.; Overview of EBSD indexing procedure showing pattern capture through to determination of crystal orientation [90].	30
Figure 2.4	Shows (a) TEM schematic [33] and (b) TEM instrument used in the present study.	32

Figure 2.5	Vickers hardness tester (a) schematic of indentation process [92] and (b) the instrument	33
Figure 2.6	JANNUS ion irradiation facility [103]	36
Figure 2.7	Cold rolling process schematic	37
Figure 2.8	Vacuum furnace used for annealing in present study.	37
Figure 3.1	EBSD-OIM map from (a), (c) longitudinal and (b), (d) transverse section of the ODS alloy of composition Fe-0.3Y ₂ O ₃ and Fe-0.2Ti-0.3Y ₂ O ₃ respectively.	42
Figure 3.2	EBSD-OIM map from Fe-14Cr-0.2Ti-0.3Y ₂ O ₃ alloy (a) longitudinal and (b) transverse section, and (c) at higher magnification which shows fine grain band.	43
Figure 3.3	Grain size distribution histograms for alloy (a) Fe-0.3Y ₂ O ₃ , (b) Fe-0.2Ti-0.3Y ₂ O ₃ and (c) Fe-14Cr-0.2Ti-0.3Y ₂ O ₃ respectively	44
Figure 3.4	Pole figure obtained from (a) Fe-0.3Y ₂ O ₃ ; (b) Fe-0.2Ti-0.3Y ₂ O ₃ and (c) Fe-14Cr-0.2Ti-0.3Y ₂ O ₃ ODS alloy for {100}, {110} and {111} planes and ODF $\phi_2 = 45^\circ$ section of (d) Fe-0.3Y ₂ O ₃ ; (e) Fe-0.2Ti-0.3Y ₂ O ₃ and (f) Fe-14Cr-0.2Ti-0.3Y ₂ O ₃ ODS alloy.	45
Figure 3.5	EBSD-OIM map from longitudinal section of (a) extruded and annealed rod, after (b) 30 %, (c) 40 % and (d) 50 % CW respectively	49
Figure 3.6	(a), (c), (e) Electron back scattered diffraction generated Orientation Imaging maps (EBSD-OIM) maps and corresponding (b), (d), (f) recrystallization mapping showing recrystallized portion in blue, subgrain in yellow and deformed portion in red of 30 % cold worked 18Cr-commercial ODS alloy after annealed at 1050, 1150 and 1250 °C respectively.	51
Figure 3.7	(a), (c) and (e) Electron back scattered diffraction generated Orientation Imaging maps (EBSD-OIM) maps and corresponding (b), (d) and (f) recrystallization mapping showing recrystallized portion in blue, subgrain in yellow and deformed portion in red of 40 % cold worked 18Cr-commercial ODS alloy after annealed at 1050, 1150 and 1250 °C respectively.	53
Figure 3.8	(a), (c) and (e) Electron back scattered diffraction generated Orientation Imaging maps (EBSD-OIM) maps and corresponding (b), (d) and (f) recrystallization mapping showing recrystallized portion in blue, subgrain in yellow and deformed portion in red of 50 % cold worked 18Cr-commercial ODS alloy after annealed at 1050, 1150 and 1250 °C respectively.	55
Figure 3.9	Orientation used for texture description in cubic materials plotted in (a) $\Phi_2 = 45^\circ$ and (b) $\Phi_2 = 0^\circ$ sections of the Euler space[66].	56
Figure 3.10	(a) Euler-X map with IPF legend in inset and (b) $\Phi_2 = 45^\circ$ section of the ODF in the extruded and annealed (1100 °C for 1h) 18Cr ODS bar sample.	57

Figure 3.11	$\Phi_2=45^\circ$ section of the ODF after (a)30%, (b)40 % and (c) 50 % CW.	58
Figure 3.12	ODF in the 30% CW ODS alloy after annealing at (a) 1050 °C - $\Phi_2=45^\circ$ section, (b) 1150 °C - $\Phi_2=0^\circ$ section and (c) 1250 °C - $\Phi_2=0^\circ$ section respectively.	59
Figure 3.13	ODF in the 40% CW ODS alloy after annealing at (a) 1050 °C - $\Phi_2=45^\circ$ section, (b) 1150 °C - $\Phi_2=0^\circ$ section and (c) 1250 °C - $\Phi_2=0^\circ$ section respectively.	60
Figure 3.14	ODF in the 50% CW ODS alloy after annealing at (a) 1050 °C - $\Phi_2=45^\circ$ section, (b) 1150 °C - $\Phi_2=0^\circ$ section and (c) 1250°C - $\Phi_2=0^\circ$ section respectively.	61
Figure 4.1	BF- TEM images and particle size distribution histogram of alloy (a), (b) Fe-0.3Y ₂ O ₃ ; (c), (d) Fe-0.2Ti-0.3Y ₂ O ₃ and (e),(f) Fe-14Cr-0.2Ti-0.3Y ₂ O ₃ respectively. The average particle size was 11 nm, 8 nm and 4 nm respectively for Fe-0.3Y ₂ O ₃ , Fe-0.2Ti-0.3Y ₂ O ₃ and Fe-14Cr-0.2Ti-0.3Y ₂ O ₃ respectively.	72
Figure 4.2	(a) HRTEM image from Fe-0.3Y ₂ O ₃ with an embedded oxide particle; (b) the FFT taken from the highlighted region and with various planes and angles indexed as bcc Y ₂ O ₃ , (c) IFFT .	74
Figure 4.3	(a) HRTEM image from Fe-0.2Ti-0.3Y ₂ O ₃ with an embedded particle, (b) the FFT taken from the highlighted region indexed as fcc Y ₂ Ti ₂ O ₇ ; (c) IFFT.	75
Figure 4.4	(a) HRTEM image from Fe-14Cr-0.2Ti-0.3Y ₂ O ₃ with an embedded particle of size 8 nm; (b) the FFT taken from the highlighted region indexed as orthorhombic Y ₂ TiO ₅ and (c) IFFT.	76
Figure 5.1	The implanted ion (in red) profile and damage (in blue) profile of 5 MeV Ni ²⁺ ions in Fe matrix calculated through SRIM. The TEM observation was carried out at the surface -highlighted in green showing the sample surface facing irradiation[151]	84
Figure 5.2	Low magnification bright field TEM images of the Fe-14Cr-0.2Ti-0.3Y ₂ O ₃ alloy (a) as-prepared; 5 MeV Ni ²⁺ ion irradiated alloy samples for the dose of (b) 40 dpa at 600 °C; (c) 40 dpa at 700 °C; and (d) annealed at 700 °C for 6 h. (scale bar shown in (a) applies for (b) and (d) also); (e),(f) SAED patterns obtained from (c) type regions showing indexed spots from different possible planes of matrix-M (bcc Fe) and particle-P (orthorhombic Y ₂ TiO ₅) oxide crystal structures.	86
Figure 5.3	Low magnification bright field TEM images of the Fe-0.2Ti-0.3Y ₂ O ₃ alloy (a) as-prepared; 5 MeV Ni ²⁺ ion irradiated alloy samples for the dose of (b) 40 dpa at 600 °C; (c) 40 dpa at 700 °C; and (d) annealed at 700 °C for 6 h. (scale bar shown in (a) applies for all the images)	88
Figure 5.4	Oxide particle size distribution of Fe-0.2Ti-0.3Y ₂ O ₃ alloy (a) as-prepared, and 5 MeV Ni ²⁺ ion irradiated alloy samples for the dose of 40 dpa (c) at 600 °C; (e) at 700 °C. Oxide particle size distribution of Fe-14 Cr-0.2Ti-0.3Y ₂ O ₃ alloy (b) as-prepared and 5 MeV Ni ²⁺ ion irradiated alloy samples for the dose of 40 dpa (d) at 600 °C; (f) at 700 °C.	90

Figure 5.5 The oxide dispersion in the DY ODS steel following 600 hour neutron irradiation, showing halos of smaller particles around larger particles: (a) before irradiation, (b) after irradiation at 532 °C to 78.8 dpa, (c) after irradiation at 580 °C to 30.5 dpa. (BF-TEM micrographs scale bar of (c) applies for (a) and (b) also)[172]. 92

List of tables

Table 2.1	Composition of the Alloys used in the present study (bulk oxygen, carbon and nitrogen content of the four alloys (in weight percent) measured using ICPMS).	25
Table 3.1	Alloy composition with bulk oxygen, carbon and nitrogen content of the four alloys (in weight percent) measured using ICPMS.	40
Table 3.2	Hardness values of three different model ODS alloys	41
Table 3.3	Hardness of the 18Cr ODS alloys with different conditions of cold work and heat treatment conditions	48
Table 3.4	Misorientation and recrystallization fraction for different conditions	56
Table 3.5	Evolution of texture in the 18 Cr ODS samples with 30, 40 and 50 % cold work when annealing is carried out at different temperatures of 1050, 1150 and 1250 °C	62
Table 3.6	Misorientation between nucleus at higher temperature and deformed grain of 30 % CW 18Cr ODS sample	65
Table 3.7	Misorientation between nucleus at 1050°C and deformed grain of 40 % CW sample	65
Table 3.8	Misorientation between nucleus at higher temperature and deformed grain of 40 % CW sample	65
Table 3.9	Misorientation between nucleus at 1050°C and deformed grain of 50 % CW sample	66
Table 3.10	Misorientation between nucleus at higher temperature and deformed grain of 50 % CW sample	66
Table 4.1	Alloy compositions with measurements of the bulk oxygen, carbon and nitrogen content of the three alloys in weight percent using ICPMS.	70
Table 4.2	Number density and average size of the particle in three ODS alloys	73
Table 4.3	Crystal structural consistency through comparison between measured and standard structure d spacing and interplanar angles	77
Table 4.4	Summary of HRTEM results from individual particles studied in the three ODS alloys including the size range of particles identified.	77
Table 5.1	Alloy composition with measurements of the bulk oxygen, carbon and nitrogen content of the three alloys in weight percent using inductively coupled plasma mass spectrometry.	83
Table 5.2	Analysis of SAED patterns obtained from Fe-14Cr-0.2Ti-0.3Y ₂ O ₃ alloy irradiated up to 40 dpa at 700 °C with fine dots showing measured d spacing values consistent with different possible planes of matrix (Fe-bcc) and orthorhombic Y ₂ TiO ₅ oxide crystal structures.	87
Table 5.3	Particle Size, density and volume fraction of the as-prepared and ion irradiated ODS alloys [151].	91

Chapter 6

Summary and scope for future work

6.1. Summary

High Cr ODS steels have been identified as a promising candidate structural material for Generation IV fission and fusion reactors because of their superior high-temperature mechanical properties, corrosion resistance and improved radiation resistance compared to conventional ferritic/martensitic steels. These properties are achieved by introducing stable oxide dispersoids into the ferritic matrix which act as obstacles for dislocation motion, sinks for radiation-induced point defects and also limit the grain growth.

The manufacturing process of ODS cladding tubes, involves a series of cold-rolling and intermediate annealing process during which the microstructure of alloy gets severely affected and different types of texture are formed. Microstructure and texture study during cold-rolling and the following annealing are essential for optimizing the fabrication procedure in order to obtain the materials with high performances. Cr plays a vital role as a bcc ferrite (matrix) stabilizer as well as adding good corrosion resistance. There have been several reports on the effect of alloying element in nano oxide particle size distribution and composition. And it is widely accepted that the presence of Ti makes the oxide particle dispersion finer, however, only a limited amount of work has been performed to probe the role of Cr in affecting the dispersion and crystal structure of the oxide particles. Further, these high Cr ODS alloys when used as reactor core structural materials will be exposed to high neutron fluence and hence irradiation stability of the oxide nano particles in high Cr ODS is of crucial importance for performance of these materials for nuclear application.

This thesis deals with study of high Cr ODS alloys from three different aspects 1. effect of alloy composition and cold work with annealing , in texture and microstructure; 2. role of alloying elements (Ti, Cr) in alloy microstructure and oxide particle dispersion, oxide particle crystal structure and composition of ODS alloys; 3. stability of oxide nano-particles upon irradiation.

A summary of the results obtained in this thesis are presented below

1. Study of microstructure and texture in ODS alloys

EBSD study of the model ODS alloys showed that the Cr added Fe-14Cr-0.2Ti-0.3Y₂O₃ has finer microstructure (with fine grain bands) as compared to the Fe-0.3Y₂O₃ and Fe-0.2Ti-0.3Y₂O₃ alloy. Though recrystallization fraction increased in this alloy dominant structure was found deformed except the fine grain bands. This indicated that not only recrystallization but some other factor in presence of Cr was responsible for fine grain structure in the alloy. Typical alpha texture with $\langle 110 \rangle \parallel \text{RD}$ is present in the Fe-0.3Y₂O₃ and Fe-0.2Ti-0.3Y₂O₃ alloy. But texture reduces near to random in case of the Fe-14Cr-0.2Ti-0.3Y₂O₃ alloy. The finer grain bands were found to be recrystallized which could be the cause for removal of texture from the alloy.

Temperature plays a crucial role in deciding the texture of the 18 Cr ODS alloy. Deformed structure was found to develop alpha and gamma fibre texture with excitation of different components depending on amount of cold work. A shift in microstructure from deformed towards substructure or recrystallized form was noticed from 1150 °C. With increase in recrystallization, the texture also transformed from alpha/gamma fibre to near Goss/Brass orientation. The mechanism of the texture transformation is suspected to be aided by high energy boundaries with high mobility associated with a misorientation range of 15-45 °.

2. Role of Cr and Ti in oxide particle dispersion, crystal structure and composition of ODS Alloys

TEM study of oxide particle size distribution in ODS alloys of composition Fe-0.3Y₂O₃, Fe-0.2Ti-0.3Y₂O₃ and Fe-14Cr-0.3Ti-0.3Y₂O₃ showed that refinement of particle size takes place upon addition of Ti and a further refinement is observed in presence of Cr.

In presence of Ti in the alloy, the particles are detected to be complex oxide type in nature. The analysed particles were structurally consistent with either orthorhombic Y₂TiO₅ or fcc Y₂Ti₂O₇. In the Cr added alloy, majority of the particles got detected with Y₂TiO₅ type along with a few consistent with fcc Y₂Ti₂O₇. Particles of orthorhombic Y₂TiO₅ type structure were in the size range of 4-16 nm and similar sized particles were also detected with fcc Y₂Ti₂O₇ type structure. This shows that there is no specific correlation between composition and size of a particle.

3. Irradiation response of the nano particles in Fe-0.2Ti-0.3Y₂O₃ and Fe-14Cr-0.2Ti-0.3Y₂O₃ ODS Alloys

Ion irradiation response of two model ODS alloys of composition Fe-0.2Ti-0.3Y₂O₃ and Fe-14Cr-0.2Ti-0.3Y₂O₃ were studied. Evolution of oxide particles under ion irradiation was investigated for a damage level of 40 dpa at irradiation temp of 600 and 700 °C. It is found that the average particle size decreases at 40 dpa in both the Fe-0.2Ti-0.3Y₂O₃ and Fe-14Cr-0.2Ti-0.3Y₂O₃ alloy irradiated at 700 °C, but histogram tail of the particle size distribution is quite distinct for the Fe-0.2Ti-0.3Y₂O₃ and Fe-14Cr-0.2Ti-0.3Y₂O₃ alloy. In the Cr alloy the limited range of initial particle size distribution compress the histogram width appreciably after irradiation. But, in the Fe-0.2Ti-0.3Y₂O₃ alloy, frequency of larger particles lessens but is found to exist. Hence, Cr makes a substantial impact in dissolution of the coarser particles present in the ODS alloy. The preferred dissolution of particles in Cr alloy could be explained through the following:

I) In as received condition, Cr added alloy had finer particles as compared to those present in Fe-0.2Ti-0.3Y₂O₃ alloy. The fraction of the larger particles (with diameter >20 nm) was 1.5% and 0.4% in the Fe-0.2Ti-0.3Y₂O₃ and Fe-14Cr-0.2Ti-0.3Y₂O₃ alloy respectively. Under irradiation, these coarser particles will start dissolving increasing the frequency of the finer ones. The process of gradual dissolution of these coarser particles (at the same irradiation dose and temperature) will enhance the frequency of the finer particles much faster in that alloy which offers initial coarse particles of comparatively smaller size [151]. Thus dissolution process can be speedy in alloy containing Cr offering relatively finer particles.

II) The Cr rich shell structure of the oxide particles and less value of displacement energy of Cr (34 eV) as compared to Fe (40 eV) helps in easy production of vacancies around the oxide particles of Cr alloy under irradiation. This suggests that presence of Cr in the ODS alloy can help in particle dissolution upon irradiation.

The increase in hardness derived from particle size refinement (as estimated in section 5.4.1-last paragraph) with increase in number density can improve high temperature creep properties of the alloy components during service.

6.2. Scope for future work

In the thesis, texture study of 18 Cr ODS alloy as a function of cold work and annealing temperature showed that texture transforms from alpha/gamma fibre to near

Goss/Brass orientation at 1150 °C. Study of texture at intermediate temperatures between 1050 °C and 1150 °C in steps will be interesting to trace the gradual evolution of texture. Further, after 30% Cold worked and annealed sample can be given further cold work followed by annealing for studying the effect of multiple step cold rolling like the real fabrication process for clad tube. Further, TEM study of the 18 Cr ODS alloy after different cold work and heat treatment can be carried out for studying the oxide particle stability. High temperature annealing like at 1150 °C and 1250 °C can be carried out on the sample annealed at lower temperature like at 1050 °C and 1150 °C to trace the effect of double annealing on texture evolution.

The present study showed the effect of Ti and Cr in oxide particle formation. It will be worth studying the effect of other alloying elements like Al, Zr etc. The formation energies of constituent elements of nanoclusters in Zr and Al containing ODS alloys were computed and binding energies of solute atoms with vacancy, Oxygen, Oxygen-vacancy and Yttrium-Oxygen-vacancy were studied [186]. It is reported that among all the selected configurations, the Zr containing clusters have higher binding energy compared to Al containing clusters. This emphasizes that when both Zr and Al together are present in a ferrite matrix with Yttrium and Oxygen, formation of Y-Zr-O clusters is preferred instead of Y-Al-O clusters. TEM and HRTEM studies can be carried out in similar model ODS alloys to verify the calculated results. Also the effect of Zr and Al on alloy texture formation will be an interesting study.

The present study showed irradiation hardening and particle dissolution into matrix at 700 °C in Ti and Cr added model alloys. In-Situ TEM and atom probe tomography can be carried out to have a deeper understanding about the stages of gradual dissolution process along with re precipitation of the oxide particles. Characterization as a function of depth in irradiated sample will give the evolution as a function of damage i.e. dose. APT, cross-sectional TEM and Positron annihilation studies is planned to get these information. Creep study of the irradiated samples can be performed to probe the improvement in creep properties in presence of very fine particles upon Cr addition in the Fe-0.2Ti-0.3Y₂O₃ alloy to substantiate the present understanding. In addition, to mimic Gen IV and fusion reactor conditions, dual beam irradiation using 5 MeV Ni ion and He ions can be interesting to have a better understanding of real irradiation response of the ODS steels. Also actual neutron irradiation to study the effect will be interesting but to produce similar dose will take a very long time and such studies are planned.

It will be worth studying ODS alloys with different strong texture components and near random texture upon irradiation. This can show how the preferred crystal orientation or texture influences the irradiation response of the alloys. Correspondingly the process route of tube fabrication can be optimized in order to produce final tubes with beneficial texture.

Abstract

ODS steels have been identified as a promising candidate structural material for Generation IV and fusion reactors because of their superior high-temperature mechanical properties and improved radiation resistance compared to conventional ferritic/martensitic steels. These properties are achieved by introducing stable oxide dispersoids into the ferritic matrix which act as pinning sites for dislocations, sinks for radiation-induced point defects and also limit the grain growth.

The thesis deals with studying ODS alloys from different aspects like a) effect of alloy composition and cold work with annealing temperature in texture and microstructure, b) role of alloying element (Ti, Cr) in oxide particle size distribution, crystal structure and chemistry, c) ion irradiation stability of oxide nano-particles in ODS alloys.

Recrystallization and texture formation in 1) Fe-0.3Y₂O₃, 2) Fe-0.2Ti-0.3Y₂O₃ and 3) Fe-14Cr-0.2Ti-0.3Y₂O₃ (model alloys) and a commercial ODS steel was studied. EBSD observation showed finer grain structure in Cr added alloy. The recrystallization and texture formation in a commercial 18Cr ODS steel as a function of cold work and annealing temperature was studied. Samples cold rolled by 30, 40 and 50% were heat treated at 1050, 1150 and 1250 °C in vacuum. Dominant deformed structure with abnormally grown grains at 1050 °C retained strong alpha fibre but with different components excited with respect to different cold work %. Substructure formation was prominent at 1150 °C. From 1150 °C, the texture transformation was observed towards Goss or Brass orientation.

Model ODS alloys were studied to probe the role of alloying element like Ti and Cr in alloy microstructure and oxide particles dispersion, crystal structure and composition. For this, three ODS alloys with the composition 1) Fe-0.3Y₂O₃, 2) Fe-0.2Ti-0.3Y₂O₃ and 3) Fe-14Cr-0.2Ti-0.3Y₂O₃ were chosen. Particle size distribution was checked from TEM images. Effect of Ti in reducing the particle size was observed consistent with earlier reports by different authors. Further, the present study showed that addition of Cr leads to even finer distribution of oxide nano particles. The crystal structure analysis of the particles was attempted from HRTEM images and consistency was found with Y₂TiO₅ and Y₂Ti₂O₇ where majority of particles were found consistent with Y₂TiO₅ crystal structure.

Irradiation response of the oxide nano particles in the Fe-0.2Ti-0.3Y₂O₃ and Fe-14Cr-0.2Ti-0.3Y₂O₃ alloys was studied using ion irradiation up to a surface dose of 40 dpa at 600 and 700 °C. Two different model ODS alloys of composition Fe-0.2Ti-0.3Y₂O₃, Fe-14Cr-0.2Ti-0.3Y₂O₃ were irradiated using 5 MeV Ni²⁺ ion beam up to a peak dose of 150 dpa at 700 °C and 600 °C at JANNUS (Saclay, France) irradiation facility giving a dose of 40 dpa at the surface. At a dose of 40 dpa, slight reduction in the particle size is observed in the Fe-0.2Ti-0.3Y₂O₃ alloy at 600 °C. A further reduction was found at 700 °C. In case of the alloy Fe-14Cr-0.2Ti-0.3Y₂O₃, at 40 dpa and 600 °C, average particle size remained nearly same when compared to the un-irradiated alloy. But at 700 °C, a drastic reduction in particle size was observed. Particle number density and volume fraction increased after irradiation in both the alloys. In alloy Fe-0.2Ti-0.3Y₂O₃ increase in particle number density and volume fraction with temperature along with finer particle size distribution suggested irradiation induced dissolution and high temperature aided re-precipitation. In Fe-14Cr-0.2Ti-0.3Y₂O₃ alloy at 600 °C, volume fraction and particle number density increased and at 700 °C volume fraction decreased but particle number density increased. The reduction in volume fraction supports dissolution. But the simultaneous increase in particle number density can be explained only when the particles become extremely fine. This suggests that parent particles get nearly dissolved and the ejected atoms re-nucleate. Thus dissolution of the particles upon irradiation via ballistic effect (producing recoils) and re-precipitation assisted by diffusion at higher temperature played a key role in evolution of the oxide particles upon irradiation.

Chapter 1

Introduction

1.1. Background

Nuclear power generation is a proven technology in spite of the acute challenges it faces like cost, safety, proliferation and waste management. It is anticipated to play an indispensable key role in the world to meet future energy needs without emitting carbon dioxide (CO₂) and other atmospheric pollutants for decades to come. The generation of electricity in fossil fuel power plants burn natural gas, coal and oil producing carbon dioxide, a major contributor to global warming. The carbon free nuclear option can be preserved and continued in the long run only with proper planning and developmental efforts for major expansion. This will ensure a future in which nuclear energy is a safer, economical and is a secure means of power generation [1].

To envisage the goal of realizing nuclear power with enhanced thermal efficiency, the structural materials have to withstand high operational temperature, high energy neutron irradiation, and corrosive environment. Hence the candidate structural materials have to satisfy stringent criteria for prolonged lifetime as demanded for better economical performance of the nuclear reactors [2]. Oxide dispersion strengthened (ODS) ferritic steels are one amongst the most potential candidates for nuclear fission reactors, fusion reactors and accelerator driven systems for nuclear waste incineration due to the outstanding microstructural stability, extraordinary high temperature property and irradiation damage resistance [3].

1.2. Concept of Generation IV Reactors

Generation IV International Forum (GIF) is widely recognized as international collaborative endeavor that was initiated to promote research and development works to assess the feasibility and performance abilities in next generation nuclear energy systems. The primary objectives of the Generation IV designs are to use fuel more efficiently, reduce radioactive waste production, be economically viable and meet stringent safety standards and ensure proliferation resistance [4]. With these goals set, around 100 experts evaluated 130 reactor concepts [5] before GIF selected six nuclear energy systems for further R&D. These include: the gas-cooled fast reactor (GFR), lead-cooled fast reactor (LFR), molten salt reactor (MSR), supercritical water-cooled reactor (SCWR), sodium-cooled fast reactor (SFR), and very high temperature reactor (VHTR) [6].

Scenario in India:

India adopted a sequential three-stage Nuclear Power Program. This program has water-cooled reactors in the first stage, fast breeder reactors in the second stage, and thorium-based reactors in the third stage. The first stage, with 18 pressurized heavy water reactors (PHWRs) in operation and many under construction and in the planning stages, has become commercially mature and successful [7]. The second stage begins with the commissioning of prototype fast breeder reactor (PFBR). Late in the second stage the program would utilize thorium as the fertile material along with plutonium so as to produce ^{233}U for the third stage for proper utilization of large Thorium resource of India [7]. The third stage reactors are proposed to be breeder reactors and are planned to operate entirely on a ^{233}U -Th fuel cycle. The molten salt breeder reactor (MSBR) is being considered as an attractive model for large-scale deployment during the third stage, in addition to sodium fast reactors (SFRs) [7]. The reactors presently being designed have goals alike Gen-III+ concepts [6].

1.3. Materials Development

The structural and clad tube materials of a nuclear reactor are of crucial importance because these are the component which ensure safe containment of the nuclear fuel and fission products and makes energy production a reality. The next generation nuclear reactors are designed for increased efficiency, safety, life of operation, and economic viability compared to existing nuclear reactors. So, they have to operate at higher neutron doses with higher temperatures, and under extremely corrosive environments [8]. In order to maintain functionality and safety of the components exposed to such challenging environmental conditions, properties that have to be satisfied by the component materials include:

- High tensile strength, adequate fracture toughness at room and operating temperature
- High temperature creep strength
- High thermal conductivity and low thermal dilatation
- Excellent corrosion resistance and compatibility with coolant
- Low activation (for fusion reactor materials)
- Tolerance towards high irradiation dose at high temperatures [9]

The structural materials which are being used in present light water and boiling water reactors become unfit to meet these criteria. Hence, extensive study and test efforts

are absolutely necessary for selection of advanced materials fit for the purpose of Gen IV [10]. At the same time, deployed nuclear reactors have to be affordable in view of construction and maintenance cost to survive as a competitive source of power generation. Hence, the materials chosen for construction can be utilized for their specific purposes at a reasonable cost, as well as be sustainable for longer life, requiring that the material damage is minimal with ruled out possibilities of failures.

The maximum target burn-up of FBR has been aimed as high as 250 GWd/t which will reduce the fuel cycle cost considerably for better economical performance. This imposes challenging requirements on swelling resistance of clad tubes at higher dose as well as its high temperature strength in the temperature range 600-700°C. For such demanding applications, austenitic stainless steels have been ruled out because of their propensity towards void swelling above a dose ~120 dpa. Figure 1.1 shows maximum hoop deformation of different grades of austenitic Phénix claddings and ferrite-martensitic materials versus dose at temperatures between 400 °C and 550 °C [11]. From Fig. 1.1, it is clear that ferritic steel becomes an obvious choice for fuel-clad material as bcc structure is more resistant against irradiation compared to fcc crystal structure [12,13]. But ferritic steels lack high temperature (above 550-600 °C) creep strength. This limits the applicability of these steels for clad-tubes in FBRs. The idea of introducing nano level dispersoids in ferritic/martensitic steel matrix has made the breakthrough to improve the creep resistance of such beyond 650°C, without sacrificing the inherent advantages like high thermal conductivity and swelling resistance of these steels [14,15]. This scenario lead to the development of oxide dispersion strengthened (ODS) steels. Figure 1.2 compares the creep behavior of a Fe-18Cr conventional alloy with a Fe-18Cr ODS alloy at 650 °C and 180 MPa. The rupture time for the non-reinforced material is <10 min against few thousands of hours for the ODS steel. The ODS steels specifically, are of ultimate importance to the development of the SFR program. They are currently being considered as potential candidate material for use as cladding tubes [16]. The neutron flux in current light water reactors (LWRs) cladding can go up to a value of 1 MW/m². This requires fuel cladding materials to have high creep strength at high temperatures and under exposure to corrosive liquid metal coolant [17]. The greatest obstacle for SFR fuel cladding is radiation-induced void swelling due to high neutron fluence under elevated temperatures [18]. ODS steels are ideal for this application as they have fine grain structure and fine dispersion of nano particles both act as sinks for point defects and obstacles for

dislocation motion, trap He in fine-scale bubbles opposing void stabilization that lead to material degradation [19,20].

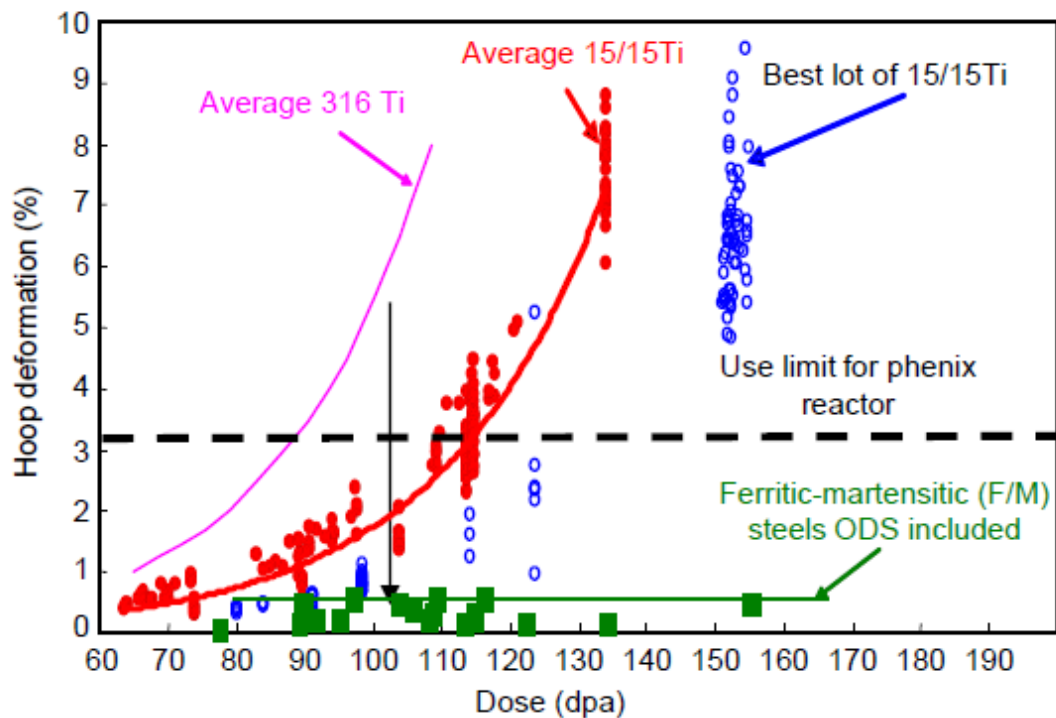


Figure 1.1 Maximum hoop deformation of different grades of austenitic Phénix claddings and ferrite-martensitic materials versus dose at temperatures between 400 °C and 550 °C [11].

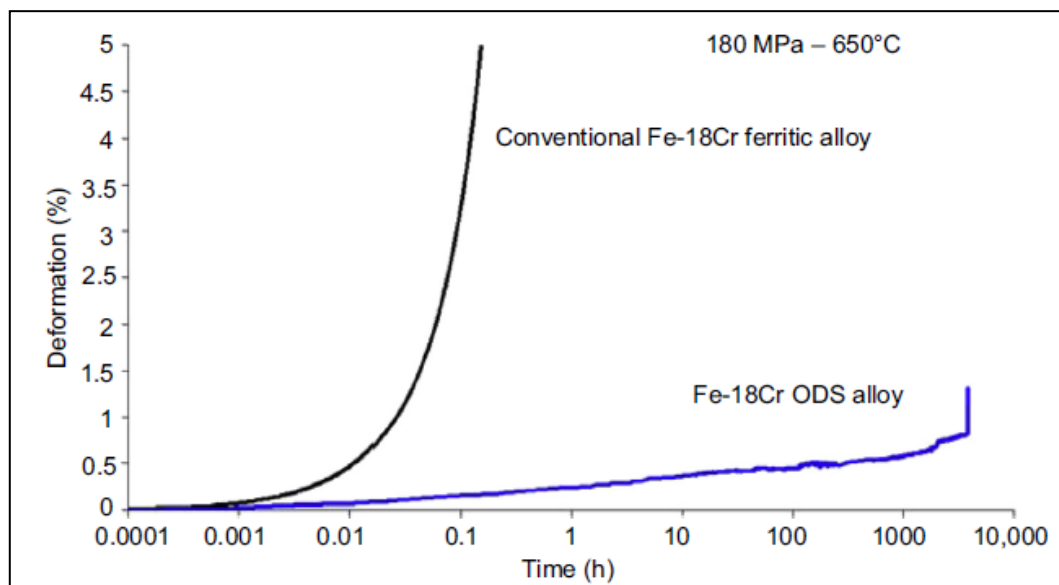


Figure 1.2 Comparison between a Fe-18Cr conventional alloy and a Fe-18Cr ODS alloy during a creep test at 650 °C and 180 MPa. The rupture time is below 10 min for the non-reinforced material against few thousands of hours for the ODS one [21].

This thesis deals with (1) study of microstructure and texture in high Cr ODS alloys, that has bearing on mechanical properties, (2) role of Cr and Ti in oxide particle dispersion, crystal structure and composition of ODS alloys, (3) irradiation of oxide nano particles in 14 Cr ODS alloys.

This chapter gives an introduction to the thesis. Starting with the various damage production mechanism in materials used in reactor core due to energetic neutrons, it introduces the effect of the damage production on materials such as void swelling, irradiation creep and helium embrittlement. Development of oxide dispersion strengthened steel (ODS) as a candidate cladding material is presented. The impact of various alloying element and subsequent compositional optimization of ODS alloy through literature survey is given. Finally, the scope and objective of the present thesis is presented. The effective and faster way to simulate neutron induced radiation damage is by ion irradiation. In view of this, a detailed introduction to the basic ion solid interaction is given along with discussion about energy loss process (both nuclear and electronic) and damage production during ion irradiation.

1.4. Radiation Damage

1.4.1. Displacement damage

During operation, nuclear reactor components get continuously bombarded with energetic neutrons. As a consequence of the interaction, matrix atoms gets knocked out from their original stable locations resulting from the energy transfer towards the atom and lattice defects are created. These primary knock-on atoms (PKA) can move on to hit other atoms generating more recoiling atoms and vacancies [22–24] as shown in Fig. 1.3. Synergistic effects of such collision sequence can eventually lead to the formation of displacement cascades, giving rise to further damage throughout the material [17].

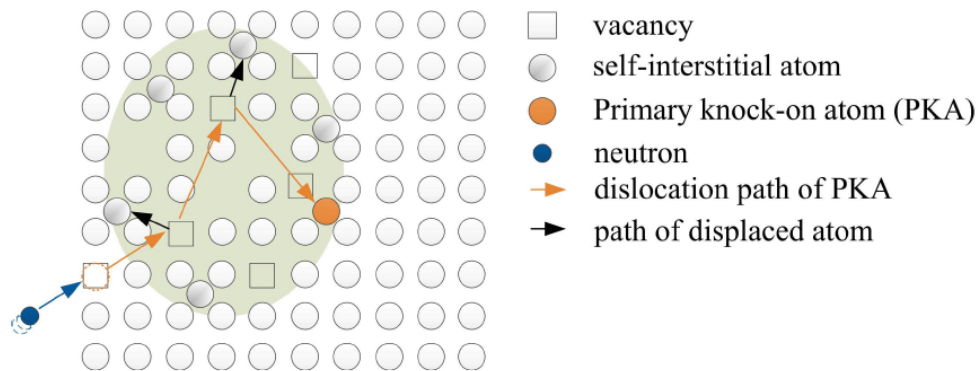


Figure 1.3 Vacancies and self-interstitial atoms in a cascade generated by neutron irradiation [9].

The radiation damage caused to the material from these collisions can be quantified through displacements per atom (dpa) concept, where 1 dpa implies that on an average each atom is displaced once from its lattice position [25,26]. In reality, expected damage in cladding tubes in Gen IV fission reactors range between 90 dpa and 200 dpa and can reach up to 200 dpa in case of the fusion reactor blankets[27]. The self interstitial atoms (SIA) and irradiation-induced vacancies constitute the primary damage state. A high density of such primary defects can be found approximately 0.5 ps after the first collision event [28].

SIA and vacancies diffuse away from the cascade (SIA diffuse faster as compared to vacancies) and part of them gets annihilated at sinks i.e. grain boundaries [28,29] or phase boundaries [30]. Recombination also takes place for some part of the SIA with existing thermal vacancies. Due to the high diffusion coefficient of SIA ($9 \times 10^{-11} \text{ m}^2 \text{ s}^{-1}$ at 300 °C [30]), recombination happens at the 10 μs time scale. A part of vacancies will find SIA and recombines. This occurs at 100 s time scale (four orders of magnitude slower than for SIA) because of lower diffusion coefficient of vacancies ($4 \times 10^{-16} \text{ m}^2 \text{ s}^{-1}$ at 300 °C [30]). The phenomena of production and loss of point defects at the same time results in a steady state concentration of vacancies and SIA, depending on neutron flux, temperature, and sink density. The steady state concentration of vacancies is orders of magnitude larger than the vacancy concentration at thermal equilibrium. This results in enhanced vacancy-assisted diffusion of the solute atoms. The role of SIA on SIA-assisted solute atom diffusion is similar but for most of the solutes (except Mn), vacancy-assisted diffusion presides. Vacancy-enhanced solute atom diffusion lead to formation of solute clusters like Cu-clusters in reactor pressure vessel steels, or equilibrium-phase particles, for example α' -phase particles in >9%Cr steels [31]. This typically happens at time scales from hours to years, depending on the nature of solute. Further, clustering of SIA or vacancies form dislocation loops and voids through vacancy coalescence.

Similar damage can be simulated by irradiation with ions (e.g. Fe ions). As an ion travels through a solid, it loses its energy by inelastic electronic excitations as well as by elastic collisions with the target atoms. The former process is called electronic excitation and the latter is known as the nuclear stopping. Electronic loss dominates at high energies whereas nuclear stopping stands over as the ion slows down. The typical energy loss behavior of the projectile ion with respect to energy is shown in Fig. 1.4.[26,32]

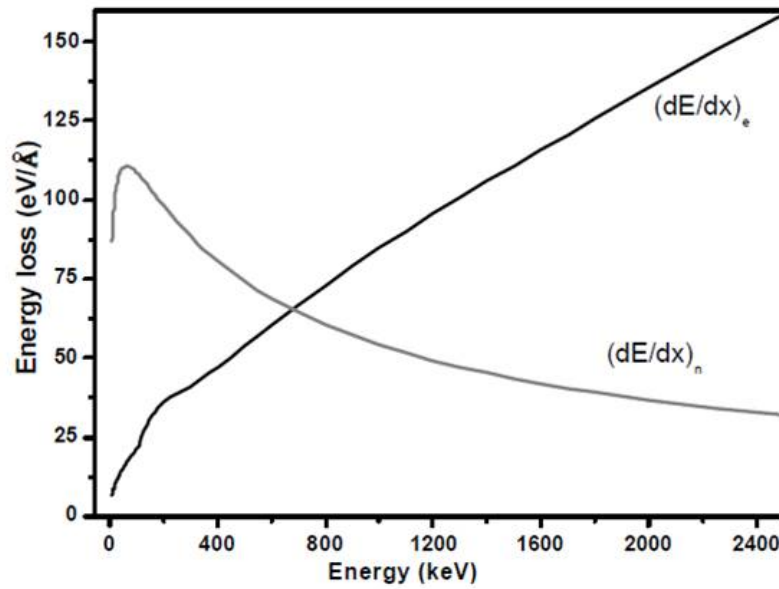


Figure 1.4 Typical energy loss behavior of ions with respect to energy in solid [32]

The average energy loss per unit path length (stopping power) arises out of the collision with the atoms in the medium. The total energy loss is a combined effect of both the processes. The total stopping power is given as follows:

$$\frac{dE}{dx} = \left(\frac{dE}{dx}\right)_e + \left(\frac{dE}{dx}\right)_n$$

Equation 1.1

The electronic stopping involves (1) momentum exchange due to collisions between the incident ion and a free electron in the target, (2) ionization of the incident ion, (3) electron capture by the incident ion, (4) de-excitation of the incident ion, (5) de-excitation of the target atom and (6) ionization of the target atom. The incident ion velocity decides the significance of these processes [33].

Nuclear stopping refers to the sum of energy losses of an ion to elastic collisions with the target nuclei. When the ions interact with target nuclei, there is a direct transfer of kinetic energy to the target atoms by elastic collisions between the projectile nucleus and the target nuclei. A common feature for all ions is that the nuclear stopping has a maximum at low energies (~ 1 keV/nucleon) and it decreases as the energy of the ions increases [33].

For experimental studies the use of ions instead of neutrons has a number of advantages[34] as follows:

- Damage rate is $10^2 - 10^4$ times more than that of typical neutron irradiation. For example, 200 dpa can be produced in days instead of decades.
- Little or no material activation under ion irradiation (Easy sample handling)
- Ease of availability of ion sources
- Precise control on irradiation conditions (temperature, damage rate, damage level)
- In-situ observation is possible

But, there are some basic differences in the damage structure produced by different types of particles. Light ions like electrons and protons create damage in form of isolated Frenkel pairs or in small clusters. Heavy ions and neutrons produce damage in large clusters as illustrated in Fig. 1.5 [26]. For 1MeV particle irradiation of nickel, half the recoils for protons are produced with energies less than $\sim 1\text{keV}$ but with an average energy of 60eV while the same number for Kr occurs at about 30keV with an average energy of 5keV [26].

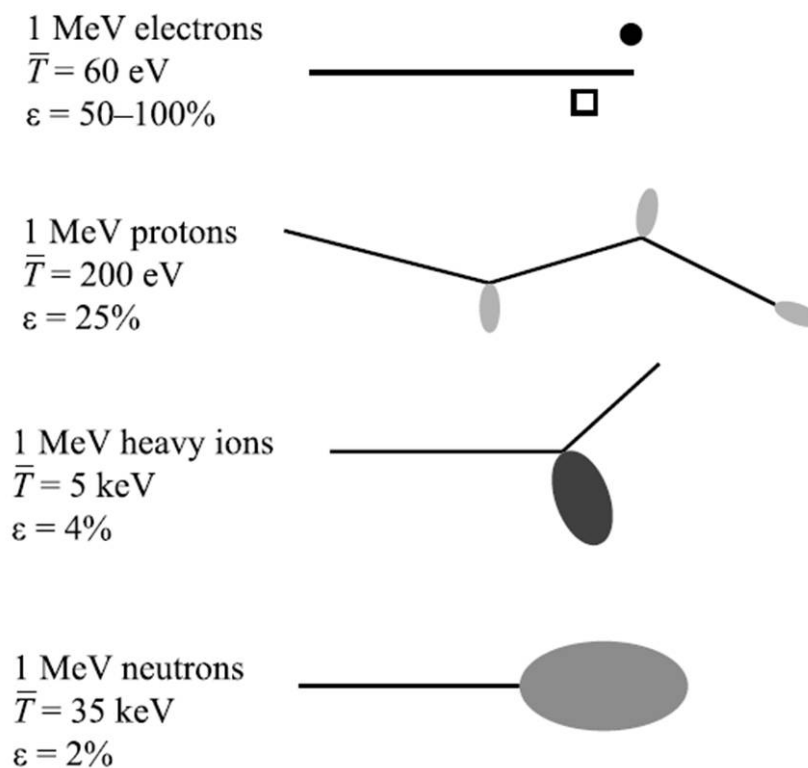


Figure 1.5 Difference in damage morphology, displacement efficiency (ϵ) and average recoil energy (\bar{T}) for 1MeV particles of different type incident on nickel [35]

Although ion irradiation was found to be a reasonable way to mimic in-reactor

conditions, the correspondence is still limited due to the typical variation in the neutron flux, spectrum and temperature within one and between several cycles in a nuclear reactor. These are difficult to imitate by ion irradiation. Further, the shallow damage profile obtained by ion irradiation and the even smaller zone free of extrinsic effects is a challenge for post-irradiation characterization. Was et al. reported the zone free of extrinsic effects to be present in a depth of 500-700 nm after ion-irradiation with 5 MeV Fe^{2+} up to 188 dpa at 460 °C. Here, a surface effect (up to 300 nm in depth) and the suppression of void swelling by the injected SIA beyond a depth of 700 nm were taken into account. In the remaining zone the observed damage was very similar to that produced in a nuclear reactor under neutron irradiation [34]. In reference [36], microstructural evolution, damage production, and steady state for high fluence are discussed in view of emulation of neutron damage using ion-irradiation. Was et al. showed that in a ferritic–martensitic steel, defect structures similar to that caused by neutrons can indeed be produced using ion irradiation with a precise control of experimental parameters [37].

1.4.2. Formation of transmutation products

Nuclear reaction with lattice atoms in structural materials leads to conversion of fraction of the original elements producing new isotopes which is known as nuclear transmutation. As a result of this, material composition changes because of formation of new elements. The important nuclear reactions in this aspect are those forming helium and hydrogen. In a thermal flux spectrum, the main source of helium is neutron reaction with B^{10} (since boron in steel is mostly found at grain boundaries, the generated helium can readily result in the formation of grain boundary bubbles) [38]. Once B^{10} is burned out, helium generation will be determined by a two-step nuclear reaction with Ni^{58} [38]. Thus a very rapid rate of helium production from B^{10} followed by a steady increase in its concentration by neutron reactions with Ni^{58} is typical characteristic.

1.5. Radiation effects

The point defects produced by irradiation migrate, recombine and produce larger defect clusters like interstitial and vacancy loops, voids and has a large effect on stability of phases in the material. The irradiation also produces new phases and precipitates. These defects give rise to radiation effect that has important bearing in material behaviors. Some of these are described below.

1.5.1. Irradiation Creep & Growth

Creep represents high temperature time-dependent irreversible deformation of a material experiencing constant load. Creep can be of different types that occur in metallic materials. However, irradiation creep is a prime concern in nuclear environment induced by intense neutron irradiation. When a reactor is operational, fuel clad gets pressurized with dose and as the defects are generated keeps on accumulating, the creep rate increases and occurs faster over reactor cycle. Generation IV nuclear reactors are designed to operate at above 500 °C where irradiation creep is expected to be a major concern. At $<0.3T_m$ (T_m : melting point) where dislocation glide is rate controlling mechanism, Creep rate decrease because of irradiation induced high defect density leading to irradiation hardening. At higher temperature where climb controlled glide become rate controlling, creep rate increase as irradiation induced excess vacancies assist dislocation climb controlled glide and reduces the temperature for glide. Irradiation growth also takes place via SIPN (Stress Induced Preferential Nucleation): I-loop normal to tensile stress & V-loop parallel (solid length increases along stress direction) and SIPA (Stress Induced Preferential Absorption) mechanism [26].

1.5.2. Helium Embrittlement

Helium (He) is present in nuclear reactors because of the (n, α) transmutation reactions [22]. The amount of He produced per dpa is a function of the neutron energy, and alloy composition which can have typical values like < 1 appm/dpa, 10 appm/dpa and 100 appm/dpa in a fast fission spectrum, fusion spectrum [39–41] and spallation targets [41] respectively. Unlike hydrogen, which also generates through (n,p) transmutation reactions [41], He has extremely low solubility in solids. Mobility of interstitial He is very high, even at a temperature much less than room temperature (RT) [42]. He when combines with vacancies gets immobilized once a critical size is reached [43]. Matrix defects, such as grain boundaries or dislocations can also trap He. Dai et al. [43] reported that He atoms bind very well with vacancies. Because of the extremely low solubility, He tends to accumulate forming molecular helium precipitate in the form of gas bubbles. In presence of heterogeneities like He, planar vacancy clusters form nano voids, which in turn act as a sinks for excess vacancies [24] (Fig. 1.6). When temperature rises to $T > 0.5 T_m$ even trapped He is becomes mobile and form bubbles through agglomeration [44]. These serve as nucleation site for voids. These bubbles gather at grain boundaries and grows (by attracting further produced He) forming cracks at grain boundaries. This leads

to intergranular fracture and weakening through helium embrittlement caused by intragranular bubbles. Phase boundaries acts are effective sink for He. If these sites are present with high density, number of helium bubbles formed in the matrix decreases [43,45]. Therefore, a high number density of microstructure features like nano particles can be introduced into the material which can serve to disperse helium accumulation.

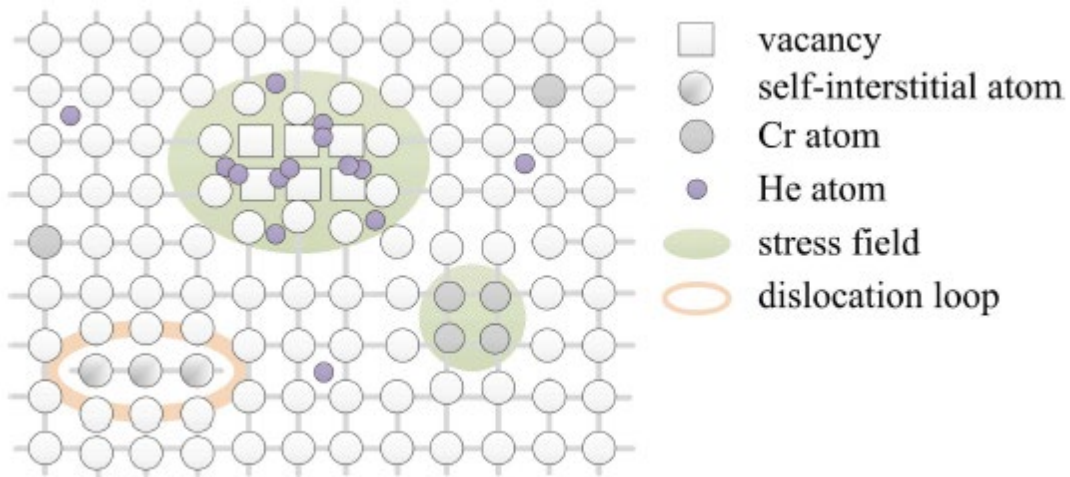


Figure 1.6 Secondary defects formed from clustered irradiation-induced primary defects [9].

1.5.3. Void Swelling

Void swelling presents the volumetric expansion of materials upon irradiation. This kind of dimensional instability is of great concern in fast reactors in only several years because of the much higher neutron flux as compared to the LWRs where similar exposure needs irradiation by decades [46]. Void is formed through vacancy agglomeration. Upon irradiation, the total concentration of vacancies exceeds the thermal equilibrium concentration value creating vacancy supersaturation [26]. This acts as a driving force for void nucleation. At low temperature, the growth of voids is limited by low defect mobility and at high temperature loss of supersaturation decides the void growth. Void swelling usually exhibits an incubation period for initiation with very less amount of swelling. Beyond this period/dose, swelling becomes liner and rapid. Thus a primary focus lies in extending the incubation/transient regime [47]. Vacancies and self-interstitials are created in equal numbers during irradiation and a major fraction of vacancies and interstitials are lost by mutual recombination. The preferential bias of interstitials to dislocations as a consequence of the differing strain fields associated with these point defects compared with vacancies, results in excess vacancies. Surviving vacancies cluster in association with gas atoms (generally helium produced by transmutation) to form embryonic

cavities. There is thus a net excess vacancy flux into the void embryos, viz., a bias-driven void growth takes place, leading to a steady swelling [26]. Swelling decreases with decreasing dislocation bias. Ferritic-bcc steels have lower bias compared with fcc austenitic stainless steels [48] due to both differences in the defect relaxation volumes [20] and the dominance of screw dislocations in bcc alloys [49]. Further, high self-diffusion (and solute diffusion) coefficients D_{sd} reduce swelling and radiation-enhanced diffusion. Ferritic-martensitic bcc alloys have higher D_{sd} than do fcc austenitic stainless steels [48]. High D_{sd} increases the flux of vacancies that drive processes toward equilibrium by increasing recombination. Moreover, solute atoms in ferritic steels are efficient recombination sites and create atmospheres around dislocations, limiting the trapping effect of interstitial [50].

1.5.4. Irradiation hardening

When a material is subjected to irradiation, the yield stress value is found to increase with associated decrease in uniform and total elongation. This is called irradiation hardening which is pronounced when the irradiation temperature is less than $0.3T_m$. Irradiation induced defects, dislocations, impurity-defect cluster complexes play a major role in this hardening process [26].

1.6. Alloy Design with alloying additions

Several variants of ODS alloys are developed using different chemical compositions and consolidation techniques which tailor the microstructure and in turn the mechanical properties to improve the alloy performance. The consolidation method followed and alloy composition shows remarkable impact on the alloy corrosion resistance, grain size, morphology, particle size distribution etc. Optimization of these properties is necessary in order to have satisfactory resistance towards radiation and temperature induced degradation in service. For instance, fabrication with pure Y_2O_3 shows an initial improvement in mechanical properties of the alloy when compared to conventional steel. Each element added as well as any step taken up in fabrication schedule serves to induce, enhance, or decrease some physical property of the alloy. Importance and effect of the most common elements added in the context of ODS alloys are detailed below:

1.6.1. Yttria and Titanium

Y_2O_3 and Ti form very small Y-Ti-O nano particles which substantially improves the mechanical strength of the alloy. Addition of pure Y_2O_3 significantly increases

mechanical properties and isotropy of particle distribution. But in presence of Ti, very fine clusters of Y-Ti-O complex oxides get stabilized. Average oxide particle size is reported as 10 nm and 3 nm in without and with Ti respectively. This refinement in particle greatly enhances the creep rupture properties [51].

1.6.2. Tungsten

Tungsten is added for solution hardening; But more than 2 wt% can be detrimental due to formation of laves phases that induces irradiation/thermal embrittlement. It is suggested that molybdenum (one of the earlier additions) should be replaced with tungsten for better isotropy and activation properties in the alloy [10].

1.6.3. Aluminum and zirconium

Al is used for improving corrosion resistance of ODS alloys, but can also have detrimental effects on irradiation embrittlement resistance and high-temperature strength of the alloy [52]. However Zr addition along with Al has beneficial effects.

1.6.4. Chromium

Chromium content decides the phase of the alloy, for example a 9wt%Cr-ODS is martensitic while 12wt%Cr-ODS alloys are usually fully ferritic (Fig. 1.7).

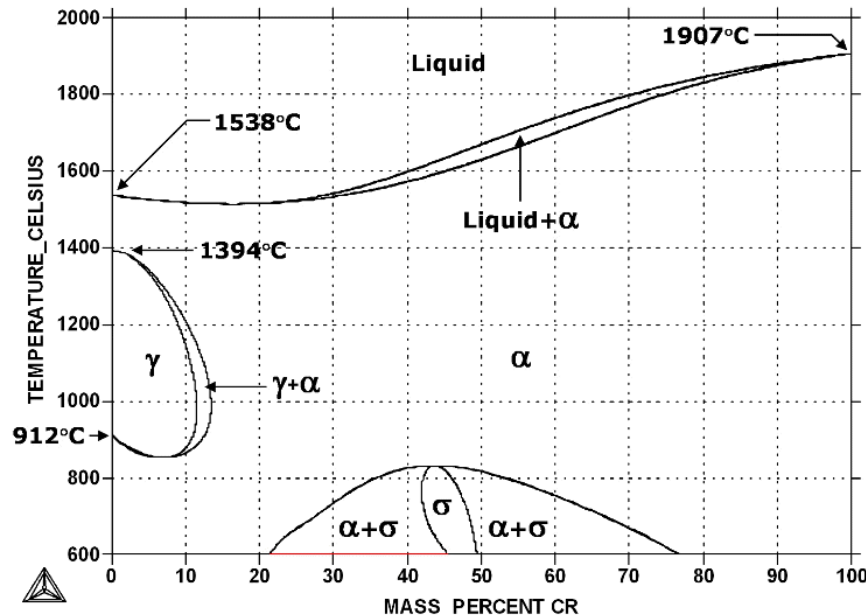


Figure 1.7 Fe-Cr Binary phase diagram [www.calphad.com]

It is well known that for high corrosion resistance, 13-18 wt% chromium concentration is desired as the α -Ferritic bcc phase is dominant at all temperatures [53]. However, 9Cr ODS with lower chromium concentration permits to obtain a ferritic-martensitic microstructure which has an improved resistance to high temperature creep as well as void

swelling. But high chromium ferritic ODS material has certain drawbacks too. High chromium favors formation of the α' phase in the temperature range of 400°C - 550°C causing thermal embrittlement. A comparison study of 14 Cr, 16 Cr, and 19 Cr ferritic ODS steels [54] showed that the degree of thermal embrittlement can be correlated to the phase separation. For application at temperatures lower than 800 °C fully martensitic steels can be opted, but at higher temperatures they undergo a phase transformation and become prone to corrosion due to less amount of chromium.

Chromium helps in improving corrosion resistance, but can lead to embrittlement at much high concentrations (>20%) due to the formation of the α' -phase [54]. This can be desired for certain nuclear applications which are nowhere connected to embrittlement. One such process is spent fuel reprocessing which requires the dissolution of uranium or plutonium oxide in nitric acid, high chromium alloys are resistant to the corrosion caused by the nitric acid on containment materials [16].

1.7. Texture

Most metals are polycrystalline materials whose properties depend on the directionality of their crystals. The statistical distribution of crystallite orientation within a polycrystalline material is commonly referred to as texture [55]. In a polycrystalline material, three different possibilities can exist where, (a) the individual grains are crystallographically similarly arranged, (b) the individual grains are differently arranged or (c) some of the grains are crystallographically similarly arranged and some are differently arranged [56]. The three ways of arrangement in the materials are respectively named as textured, randomized or partially textured materials. The three conditions of a material are depicted in Fig. 1.8 [56]. The orientation of crystallites within a polycrystalline material is not necessarily constant. Texture of a material can get affected with thermo mechanical processing.

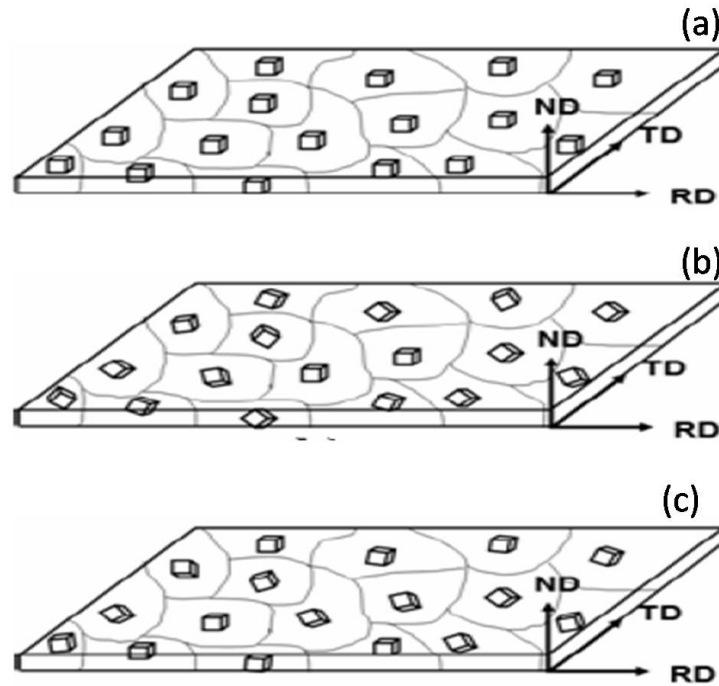


Figure 1.8 (a) Grains are crystallographically similarly arranged, (b) grains are crystallographically differently arranged, and (c) some grains are crystallographically similarly and some are differently arranged [56].

1.7.1. Representation of Texture

In order to represent the orientation of grains in a material some external frame of reference is chosen. For flat products like sheets and plates this frame of reference consists of rolling direction (RD), a normal direction (ND) and transverse direction (TD) [56]. The texture or the preferred orientation is designated by $\{h\ k\ l\}$ $[u\ v\ w]$ where $\{h\ k\ l\}$ represents the plane parallel to the sheet plane and $[u\ v\ w]$ represents the direction parallel to rolling direction [57,58]. Texture of a material is characterized using pole figure or orientation distribution function.

1.7.1.1. Pole Figure

The pole figure is the most common method for representing conventional textures. A pole figure is generated following the principle of stereographic projection [59,60] where positions and intensities for specific crystallographic orientations are plotted with respect to the relation hold with specimen's frame of reference. Fig. 1.9 shows a schematic of (100) pole figure. In Fig. 1.9 (a), the Stereographic projection of (100) poles is shown and the projection of (100) poles of one grain on the equatorial plane is represented in Fig. 1.9 (b). Fig. 1.9 (c) represents the Projection of the (100) poles of a randomly oriented polycrystalline material.

Figure 1.9(d) shows the projection of (100) poles in case of a textured polycrystal. Normally, this is represented using contour maps – as shown in Fig. 1.9(e).

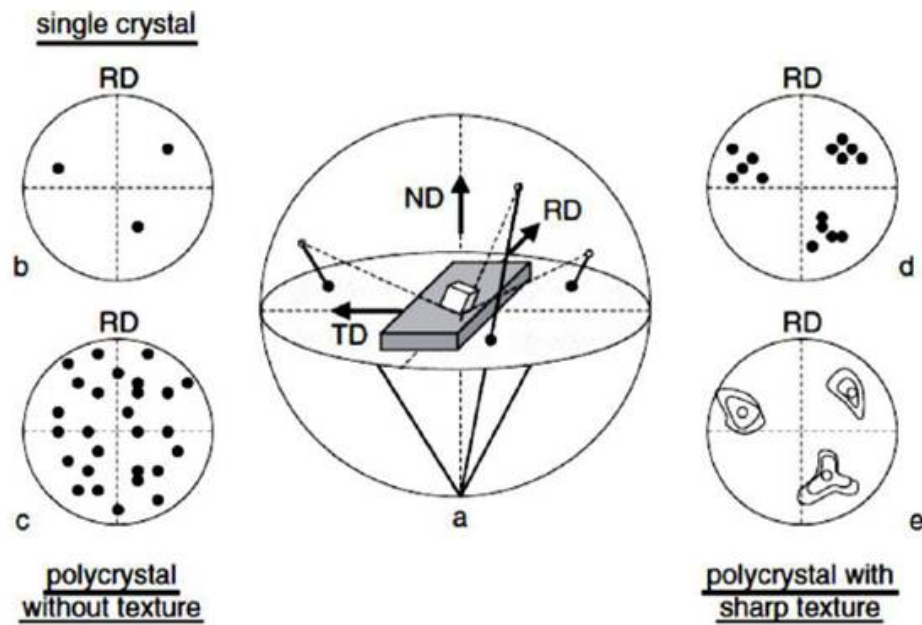


Figure 1.9 Schematic showing construction of a (100) pole figure [56]

Pole figure discussed till now, presents texture in terms of one or more components which scatters with small deviation around ideal orientations. These are referred as peak-type components. Usually some deformation processes which are axially symmetric like wire-drawing, texture is produced with rotational symmetry. Textures of this type are designated by specifying the crystallographic direction $\langle uvw \rangle$, which is parallel or almost parallel to the axis of deformation. These are known as fiber textures, and the axis is named as the fiber axis. Fiber textures are shown as continuous bands of orientations in the pole figure (Fig. 1.10). Fig. 1.10 shows $\langle 110 \rangle$ fiber textures through bands of orientations in a (001) pole figure. When the bands are uniformly populated then it is called a perfect fiber. In case of partial population, partial fiber texture forms.

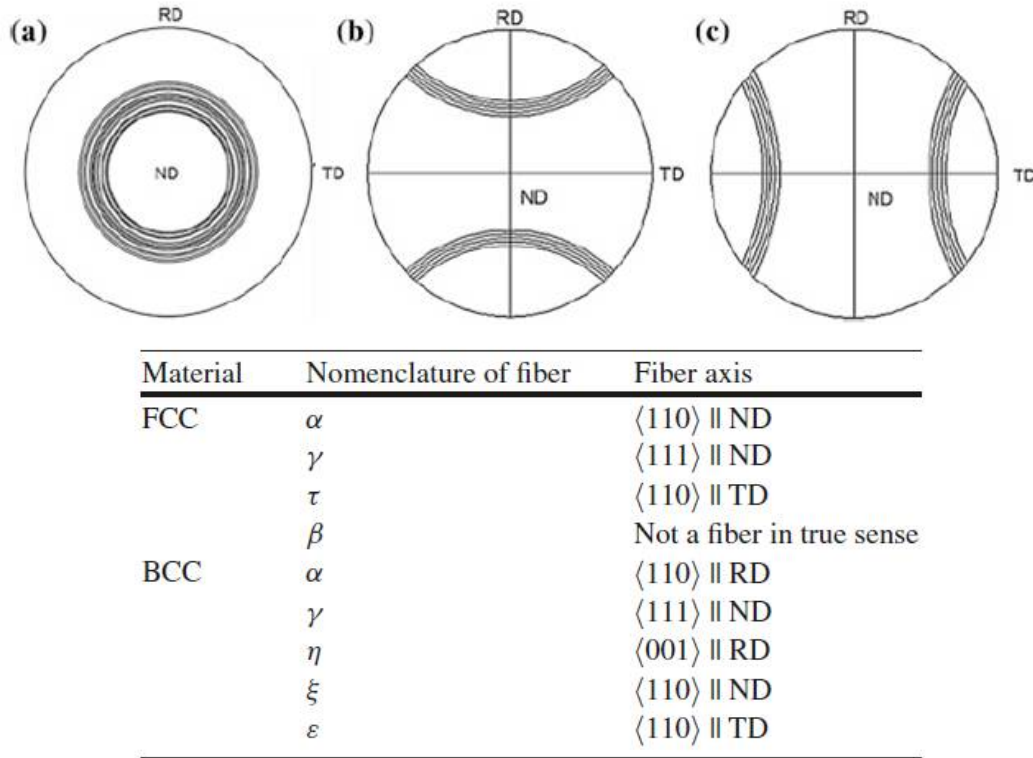


Figure 1.10 (001) Pole figure showing (110) fiber along (a) ND, (b) RD, (c) TD and (d) typical texture fibers in fcc and bcc materials[59]

1.7.1.2. Orientation Distribution Function (ODF)

A crystal is three dimensional object but the pole figure representation has only two angles. Thus, pole figure representation of texture has certain limitations – in pole figure representation, it is necessary to analyze all intensities separately, and while projecting there is always a chance to miss certain orientations [59–61]. However, these limitations are overcome through use of ODF. An ODF presents the frequency of occurrence of specific crystal orientations in 3-D Euler space using three Euler angles. The angles are the three consecutive rotations which are applied to every crystallite in order to transform crystallographic frame into specimen frame. ODF is mathematically expressed as:

$$\frac{dV}{V} = f(g)dg$$

Equation 1.2

Where, g represents orientation of a grain and f is the volume fraction of grains in intervals $g \pm \Delta g$. The ODF has a constant value for texture less sample. In presence of texture, the ODF will have maxima and minima [61,62].

- **Euler Angles**

Euler angles define the orientation g of a grain through which graphical representation of an ODF is possible. Two different co-ordinate systems are chosen: one for the sample (sample axes system X_i) and another for the crystal of a grain (crystal axes system X^c_i) (Fig. 1.11). Depending on the shape of the sample, sample system is defined. In case of a rolled sheet, the coordinate systems are chosen such that the axes X_1 , X_2 and X_3 presents rolling direction (RD), transverse direction (TD) and normal direction (ND) of the sheet respectively. The orientation of the crystal axes system can be expressed in the reference frame of the sample axes system through three rotations (Fig. 1.11). The three rotations in series as described in Bunge convention are as follows:

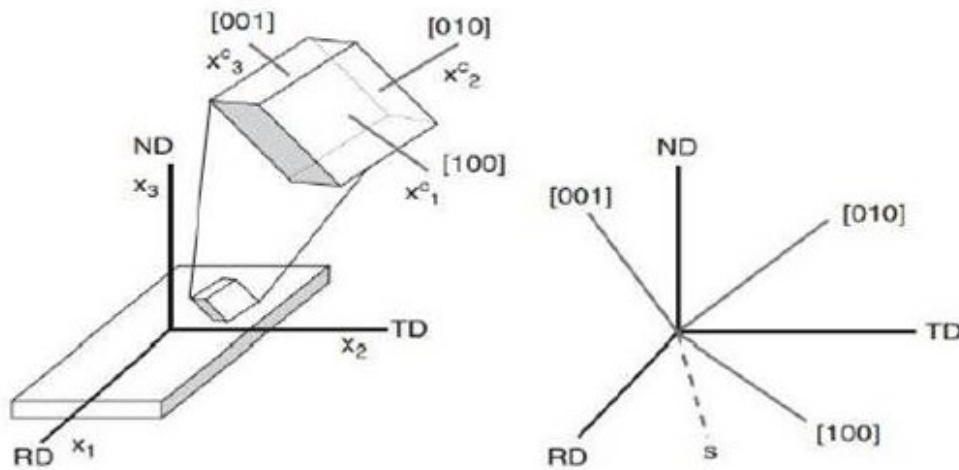


Figure 1.11 Orientation of the crystal axis system (X^c_i) and the sample axis system $\{RD, TD, ND\}$; s is the intersection of the planes $(RD-TD)$ and $([100]-[010])$ [63].

First ϕ_1 rotation is given around ND which take RD in the position s , where s is perpendicular to the plane defined by ND and $[0\ 0\ 1]$. After rotation, RD and TD goes to RD' and TD' respectively. A second rotation around RD' by Φ merges ND with $[0\ 0\ 1]$. Now, TD' changes to TD". A third rotation of ϕ_2 is applied around ND same as $[0\ 0\ 1]$ is given so that RD' coincides with $[1\ 0\ 0]$ and TD" with $[0\ 1\ 0]$. These three angle values (ϕ_1, Φ, ϕ_2) used to describe the crystal orientation are called Euler angles (Fig. 1.12).

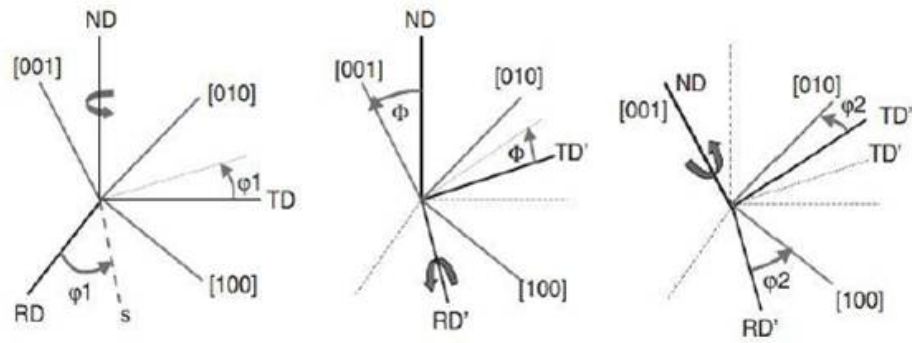


Figure 1.12 Definition of Euler angles, ϕ_1 , Φ and ϕ_2 , in Bunge convention [64].

- **Euler Space**

Euler space is obtained by plotting the three different Euler angles in Cartesian coordinates generating the graphical representation of ODF. Fig. 1.13 shows Euler space with different fibre textures typically formed in cubic materials. Many often $\phi_2 = \text{constant}$ sections represents the most frequently observed ideal orientations in cubic metals as shown in Fig. 1.14.

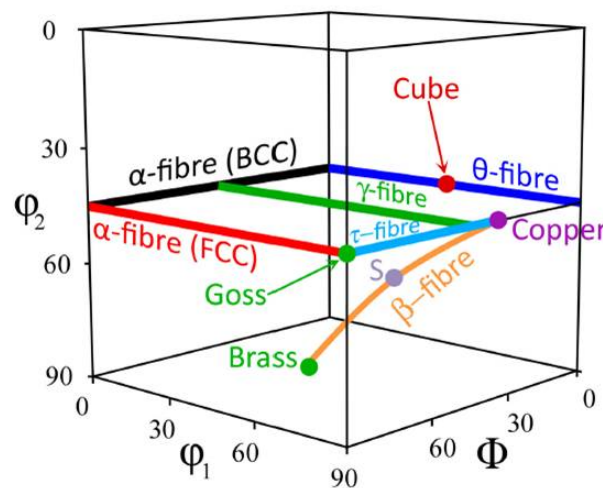


Figure 1.13 Representation of Euler space with Euler angles showing Various fibre textures that are of relevance for rolling and annealing textures in fcc and bcc alloys [65].

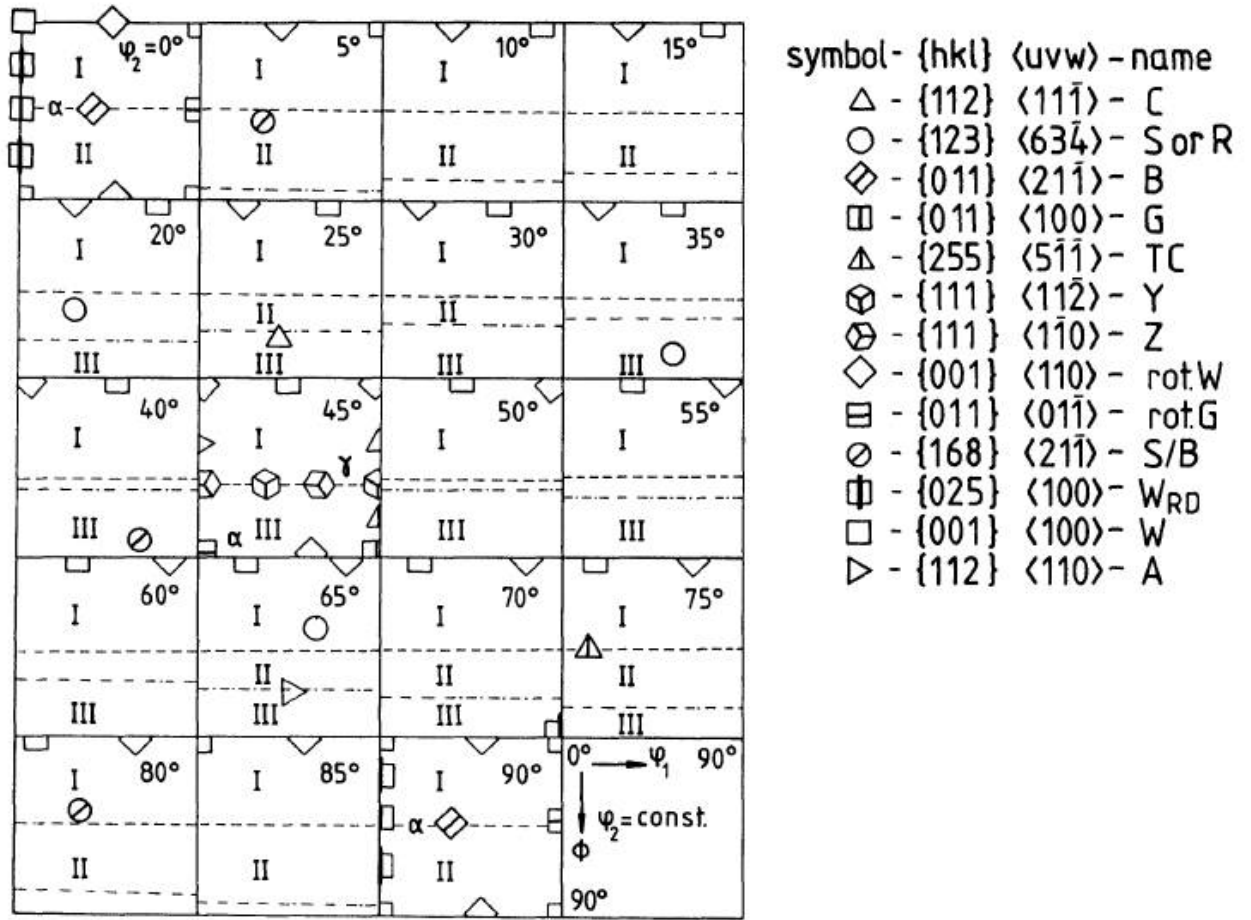


Figure 1.14 Some ideal orientations used for texture description in cubic materials plotted in $\phi_2 = \text{constant}$ sections of the Euler space [66].

The fabrication of clad tubes involves successive stages of cold work after extrusion and intermediate annealing during which the microstructure of alloys are severely affected and different types of texture are produced. An alloy with almost random grain orientation distribution presents weak texture which is desirable to hinder grain boundary sliding during deformation at high temperature [67]. Analysis of microstructure and texture during cold-rolling and after annealing are essential for optimizing the fabrication route in order to obtain the materials with high performances.

1.8. Motivation

As discussed above, ODS ferritic steels with excellent radiation resistance and superior creep strength has become promising candidates for cladding tubes in advanced fast reactors [68–70]. The manufacturing process of ODS cladding tubes, involves a series of cold-rolling and intermediate annealing [71,72] process during which the microstructure of alloy gets severely affected and different types of texture are formed. Microstructure and texture study during cold-rolling and the following annealing are essential for

optimizing the fabrication procedure in order to obtain the materials with high performances. Few works on recrystallization and texture of cold-rolled ODS ferritic steels have been reported [73–76].

Therefore, in the present thesis, evolution of microstructure and texture with various amounts of cold-rolling and annealing at different temperatures was studied in a commercial 18Cr–ODS steels.

Several reports are there on the effect of alloying element in nano particle size distribution and composition. Murali et al. [77] theoretically probed clustering behavior of Ti, Y and O in bcc Fe in presence of Cr by ab initio calculations. The report revealed that the Cr shows weak interaction with vacancies and repulsive interactions with Y and Ti [77]. In addition, structure of nanoclusters was found with a Cr rich shell formed around Y, O, Ti enriched core.

Even though a number of experiments have been carried out in order to understand the oxide particle evolution and their crystal structure, the effect of the alloying elements in the formation of the oxide particles and deciding their crystal structure is not yet clear. Experimental studies showed that Ti stabilizes the ultrafine clusters and makes the particle dispersion finer [78]. But only a very few reports exist that focuses on studying the role of Cr in size distribution and crystal structure of oxide nano particles.

Hence, in the present thesis, three simple alloys of composition Fe–0.3Y₂O₃, Fe–0.2Ti–0.3Y₂O₃ and Fe–14Cr–0.2Ti–0.3Y₂O₃ (in wt %) were chosen for understanding the role of Ti and Cr in alloy microstructure and oxide particles dispersion, crystal structure and composition.

Reactor structural materials are exposed to high neutron fluence. So, study of irradiation stability of the oxide nanoparticles in ODS (future clad tube) is of immense importance. Simulation of radiation damage in materials is possible using ion beam (from ion accelerator). Irradiation study has been performed in a 14Cr ODS alloy at 500 °C and 104 dpa produced via neutron bombardment and particles were reported as stable [79]. Real reactor damage of 200 dpa was also produced in 14Cr ODS alloy at 420 °C with the help of nuclear test reactor (FFTF: Fast Flux Test Facility) and no notable change was observed in nano particle density [80]. A neutron dose of 2.5 dpa, 7 dpa and 15 dpa with corresponding irradiation temperature of 400, 330 and 500 °C could neither dissolve nor made them grow [81]. On the other hand, Particles of diameter 1-2 nm are found to undergo complete dissolution at 100 dpa, -75 °C and at 40 dpa from -43 to 26 °C in a 14Cr

ODS alloy [82,83]. Allen et al. [84] conducted a study on 5 MeV Ni ion irradiated 9 Cr ODS steel at 150 dpa with irradiation temperature of 500-700 °C. The authors found that as dose increases, particle size decreases and number density increases for all temperatures [84]. Lescoat *et al.* [85] studied irradiation response of oxide particles in Fe-18Cr ODS and observed a linear relationship between size of the particles with $t_{irr}^{1/3}$ under ion irradiation at 500 °C up to 75 and 150 dpa where t_{irr} presents the time of irradiation.

Wharry et al. [86] summarized several studies on irradiation evolution of oxide nano particles in bcc Fe-Cr based ODS alloys and commented that with wide variation in experimental conditions, results have been very different and inconclusive. Hence, to study the irradiation response of the nano particles in presence of different alloying addition in the matrix, Ni²⁺ ion irradiation was carried out in the Fe-0.2Ti-0.3Y₂O₃ and Fe-14Cr-0.2Ti-0.3Y₂O₃ alloys and effect was studied at 40 dpa with irradiation temperature of 600 and 700 °C.

Organization of thesis:

This thesis deals with studying high Cr ODS alloys from three different aspects 1. Effect of alloy composition and cold work with annealing, in texture and microstructure, 2. Role of alloying elements (Ti and Cr) in alloy microstructure and oxide particle dispersion, oxide particle crystal structure and composition of ODS alloys 3. Stability of oxide nano-particles upon irradiation. The thesis is organized into six chapters. Apart from current chapter that gives a brief introduction to the thesis, contents of other five chapters are given below

Chapter 2: This chapter explains the basics of the materials chosen, fabrication process and the experimental techniques used to characterise and understand the effect of alloying element and ion irradiation in the alloys. The theory and experimental methods for the characterisation techniques used in the present thesis, electron back scattered diffraction (EBSD) equipped with scanning electron microscopy (SEM), Transmission electron microscopy (TEM), Vickers hardness test were explained.

Chapter 3: In this chapter, the effect of Ti & Cr in the evolution of alloy microstructure, texture and hardness was studied with the aid of Vickers hardness tester and EBSD in model ODS alloys of composition Fe-0.3Y₂O₃, Fe-0.2Ti-0.3Y₂O₃ and Fe-14Cr-0.2Ti-0.3Y₂O₃. The orientation image generated through EBSD showed equiaxed grain structure in both longitudinal and transverse sections of all the extruded alloy bars.

The Cr added alloy had finer microstructure. Cr added alloy was found with higher hardness value as compared to the other two alloys. Typical alpha texture with $\langle 110 \rangle \parallel \text{RD}$ was found in the Fe-0.3Y₂O₃ and Fe-0.2Ti-0.3Y₂O₃ alloy. But texture reduces near to random in case of the Fe-14Cr-0.2Ti-0.3Y₂O₃ alloy. This chapter also analyses the recrystallization and texture formation in a commercial 18Cr ODS steel as a function of cold work and annealing temperature. As extruded rod of 18Cr ODS was sliced and given cold work of 30, 40 and 50 % via rolling. Cold worked samples were heat treated at 1050, 1150 and 1250 °C in vacuum followed by furnace cooling. Dominant deformed structure with abnormally grown grains at 1050 °C retained strong alpha fibre but with different components excited with respect to different cold work %. At 30% cold work, the dominant alpha fibre component was $\{001\} \langle 110 \rangle$. After 40 % cold work, $\{111\} \langle 1\bar{1}0 \rangle$ became much stronger alpha component (15 times random) and gamma fibre component was also formed. 50 % cold work led to weaker alpha with wide spread from $\{111\} \langle 1\bar{1}0 \rangle$ to $\{001\} \langle 110 \rangle$ with $\{111\} \langle 1\bar{1}0 \rangle$ being strongest and gamma component also became weaker (6 times random). Substructure formation was prominent at 1150 °C. From 1150 °C, the texture transformation was observed towards Goss or Brass orientation.

Chapter 4: This chapter presents the studies carried out in three different model ODS alloys. In order to study the exclusive effect of alloying element in the microstructure and nano particle formation in the alloy, simple model ODS alloy systems were necessary. For this, three ODS alloys with the composition 1) Fe-0.3Y₂O₃, 2) Fe-0.2Ti-0.3Y₂O₃ and 3) Fe-14Cr-0.2Ti-0.3Y₂O₃ were chosen. The effect of Ti & Cr in the evolution of oxide nano particle formation was studied with the aid of TEM. Particle size distribution was checked from TEM images. Effect of Ti in reducing the particle size was observed consistent with literature. Present study showed that addition of Cr leads to even finer distribution of oxide nano particles. The crystal structure analysis of the particles was performed from HRTEM images and consistency was found with orthorhombic Y₂TiO₅ and fcc Y₂Ti₂O₇ with the first type as majority. The principal findings of the present work are that Ti refines the particle size and Cr addition leads to further refinement of particle size with formation of Cr-rich shells around oxide nano particles of all sizes but has no significant effect on the oxide crystallography.

Chapter 5: The ODS alloys of composition Fe-0.2Ti-0.3Y₂O₃ and Fe-14Cr-0.2Ti-0.3Y₂O₃ were irradiated at JANNUS (Saclay, France) irradiation facility for a peak dose of

150 dpa at 700 °C and 600 °C using 5 MeV Ni²⁺ ions. The damage level at the surface was 40 dpa. Evolution of the oxide particles examined under HRTEM.

Evolution of oxide particles under ion irradiation was investigated for a damage level of 40 dpa at irradiation temperature of 600 and 700 °C in the above two alloys. Irradiation at 700 °C substantially decreases the particle size. In presence of Cr, the size reduction becomes much more pronounced. Two possible reasons were figured out to explain the role of Cr in speeding up the oxide particle dissolution process: I. Cr added alloy had comparatively smaller particles in the as prepared state. Dissolution of these particles upon irradiation promptly increases the frequency of much finer particles. II. Cr forms shell around particles and gets displaced at lower energy. This can be responsible for a net vacancy bias towards particle favoring dissolution/mass loss. Estimation of irradiation induced hardness showed an appreciable increase. This may be advantageous in view of high temperature creep resistance of the clad/wrapper application.

Chapter 6: In this chapter, the summary and the salient features of the thesis are presented along with the scope for future work.

Chapter 2

Experimental

2.1. Materials

To study the effect of cold work and annealing temperature in texture, a high Cr commercial ODS alloy with 18 wt % Cr was selected. The detailed composition is given in Table no. 2.1. As the commercial alloy is composed of several alloying element, studying the effect of individual alloying element in oxide particle size and crystal structure becomes complicated. To study the exclusive effect of Ti and Cr, model ODS alloys like Fe-Y₂O₃, Fe-Ti-Y₂O₃ and Fe-Cr-Ti-Y₂O₃ were chosen as simple platforms. The detailed composition is given in Table no. 2.1. Multiple alloying elements which are present in commercial ODS alloys are avoided here purposefully in order to prepare a simple reference system and elucidate the specific effect of alloying element addition.

Table 2.1 Composition of the Alloys used in the present study (bulk oxygen, carbon and nitrogen content of the four alloys (in weight percent) measured using ICPMS).

Alloy	Ti	Cr	Y ₂ O ₃	Al	W	O (%)	C (%)	N (%)	Fe
Fe-0.3Y ₂ O ₃	-	-	0.3	-	-	0.46	0.03	0.019	Balance
Fe-0.2Ti-0.3Y ₂ O ₃	0.2	-	0.3	-	-	0.47	0.02	0.009	Balance
Fe-14Cr-0.2Ti-0.3Y ₂ O ₃	0.2	14	0.3	-	-	0.38	0.02	0.006	Balance
Fe-18Cr-0.3Ti-0.3Y ₂ O ₃	0.3	18	0.3	0.05	2.2	0.12	0.03	0.016	Balance

2.1.1. Fabrication Process

The 18 Cr ODS alloy bar (i.e. the commercial ODS alloy bar used in this study) was prepared at ARCI. The process involved milling of argon atomized 18Cr steel powders with an average size of 90 µm produced at ARCI (International Advanced Research Centre for Powder Metallurgy and New Materials) and nano yttria powder (30–50 nm size, 99.95% purity) supplied by M/S Inframat Advanced Materials, LLC, USA in a high energy horizontal attritor mill (Simoloyer CM-08, ZOZ GmbH, Germany) for 6 h at 700 rpm with a ball to powder ratio of 7.5:1(hardened steel balls were used). After

degassing at 450 °C, sealed cans were extruded at 1150 °C with an extrusion ratio of 9:1 in Nuclear Fuel Complex, Hyderabad. The extruded bar was annealed at 1100 °C for 1h.

The model ODS alloys were prepared using mechanical alloying and hot extrusion (schematically presented in Fig. 2.1). Highly pure Fe, Ti, Cr, and Y_2O_3 elemental powders were weighed and mixed for desired compositions of Fe–0.3 Y_2O_3 , Fe–0.2Ti–0.3 Y_2O_3 and Fe–14Cr–0.2Ti–0.3 Y_2O_3 . The Alfa Aesar- Y_2O_3 powder (22 nm average particle size) had bcc crystal structure. Mechanical alloying was carried out in Simolayer CM-08 ball milling machine under argon atmosphere at 1000 rpm for 4 h (using a ball to powder ratio of 10:1; hardened steel balls were used). The mechanically alloyed powders of composition Fe–0.3 Y_2O_3 and Fe–0.2Ti–0.3 Y_2O_3 were extruded at 1050 °C and then annealing at 950 °C for 2 h followed by air cooling [87]. Extrusion was performed at 1150 °C temperature for the Fe–14Cr–0.2Ti–0.3 Y_2O_3 alloyed powder and subsequently annealed at 1050 °C for 0.5 h and tempered at 750 °C for 2 h with air cooling [88]. Consolidated model ODS rods of 12 mm diameter were prepared from all three alloy compositions.

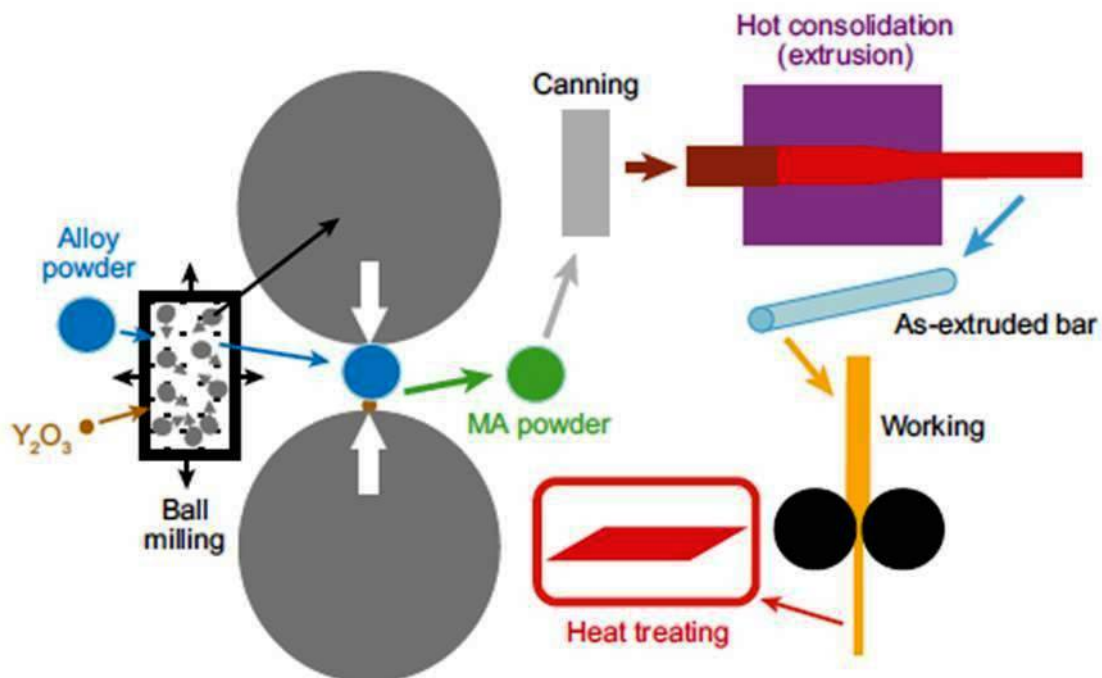


Figure 2.1 ODS Alloy tube manufacturing process [20]

2.2. Methods

2.2.1. Sample Preparation

2.2.1.1. 18 Cr ODS

The extruded and annealed rod was sliced along longitudinal direction using EDM wire cutting machine and the slices were cold rolled to generate different amount of cold work like 30, 40 and 50 %. The percentage reduction in thickness was evaluated as the cold work applied to the sliced sheet sample. Annealing was carried out at 1050, 1150 and 1250 °C for 0.5 h in vacuum followed by furnace cooling. The longitudinal sections of the samples were mounted and polished using SiC emery papers up to diamond finish and electropolished in a solution of methanol and HCl in 7:3 ratio at 23 V and -32 °C for EBSD (Electron Back Scattered Diffraction) study.

2.2.1.2. Model ODS alloys

In order to prepare the EBSD samples, longitudinal and transverse sections were cut from the three ODS alloy rods and were mounted using hot mount facility. The mounted sections were mechanically polished using SiC emery sheets of grit size 320, 540, 600, 800 & 1200 followed by diamond finish. The samples were electropolished using electrolyte solution of methanol and perchloric acid in a volume ratio of 95:5.

For TEM study of as received model ODS alloys, disks of thickness around 300 µm were cut from the rod. The disks were mechanically polished up to a thickness of near 50 µm to achieve required electron transparency and reduce electromagnetic interaction between the electron beam and the magnetic sample to minimum. 3 mm diameter disks were punched, deburred and electropolished in twin jet electropolishing machine model Tenupol-5. The schematic is given in Fig. 2.2. The disks were electropolished up to perforation using a solution of ethanol, 2-butoxy ethanol and perchloric acid (7:2:1 volume ratio) at ~ -35 °C. During electropolishing, the voltage was optimized and 22 V was applied.

For studying the effect of irradiation at 40 dpa on the surface of the ion irradiated samples, the samples were thinned from the back side. The irradiated surface was protected using lacomit varnish and then electropolishing was carried out up to perforation as mentioned before.

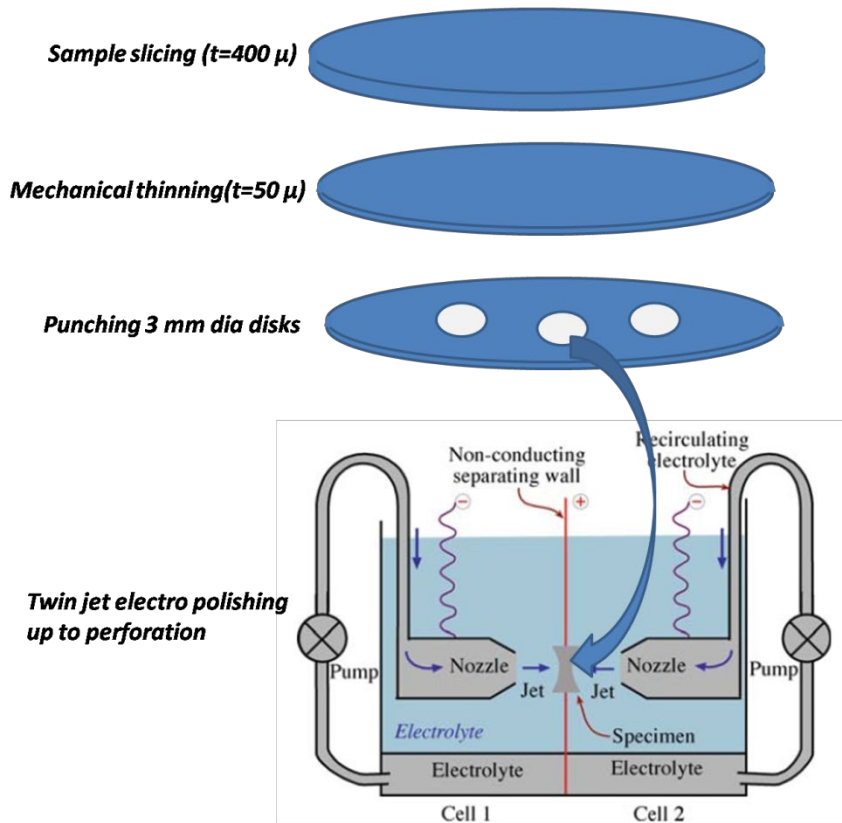


Figure 2.2 TEM sample preparation process [89].

2.2.2. Field Emission Gun Scanning Electron Microscopy (FEGSEM) and Electron Back Scattered Diffraction (EBSD)

Orientation imaging microscopy was generated in the present study using a Zeiss Sigma FEGSEM (Field Emission Gun –Scanning Electron Microscope) equipped with electron back scattered diffraction (EBSD)-Nordlys nano detector.

Scanning electron microscopy (SEM) uses a focussed electron beam to raster scan over the sample surface. As the electrons hits the sample surface, electron matter interaction generates different signals like secondary electrons, back scattered electrons, X –rays etc. The number of secondary electrons entering the detector varies as a function of sample surface features. For raised surfaces, more number of electrons enters the detector while depressed surfaces contribute lesser electrons to enter the detector. Hence, raised surfaces appear brighter and depressed surfaces appear darker producing different contrast in the image. Therefore, by detecting the secondary electrons specimen morphology and topography can be studied. Backscattered electrons show Z-contrast depending on the composition of the elements present in the specimen. SEM can be operated with an accelerating voltage up to 30 kV by accelerating the primary electrons towards the sample. The resolution of SEM is 1.3 nm with an operating voltage of 15 kV.

EBSD is a SEM based microstructural-crystallographic technique. This powerful technique is used for crystal orientation mapping, grain size and grain boundary character analysis, micro-texture, strain and identification and separation of phases (that belongs to different crystal structures).

In EBSD, a primary electron beam hits a tilted crystalline sample and generates a divergent source of electrons just beneath the striking location on the sample. These electrons get backscattered by crystal lattice planes and diffraction patterns are produced on a suitably placed phosphor screen. The diffraction pattern consists of a pair of parallel lines known as Kikuchi bands. Width of such band corresponds to distinct crystallographic plane of sample crystal structure. The center line of each Kikuchi band represents the intersection of the diffracting plane (generating the band) with phosphor screen. The patterns recorded in camera are transferred to computer for indexing and identifying crystal orientation.

The positions of the Kikuchi bands are extracted from the patterns using Hough transform. This transformation of line to point is used for calculating the crystal orientation of the sample region generating the pattern. Having knowledge about the experimental geometry, d spacings obtained from measured band widths (represents most probable diffracting lattice plane) and angle between the bands are compared with look-up tables of expected angles for the suspected phases present within the sample (Fig. 2.3). Capturing patterns and indexing are performed very fast in modern systems and when combined with precise scanning of the incoming electron beam, a detailed mapping of the sample crystallography (crystal type, crystal orientation, pattern quality etc.) is generated. These maps provide valuable information about the sample microstructure [90].

In present study, EBSD measurements were carried out at an accelerating voltage of 20 kV at a specimen inclination angle of 70° towards the camera. Fe-bcc was selected as the phase for indexing. The Orientation maps were taken with a working distance of 13 mm, sample to detector distance of 202 mm with a step size of $0.8\ \mu\text{m}$ with the aid of Aztec software interface.

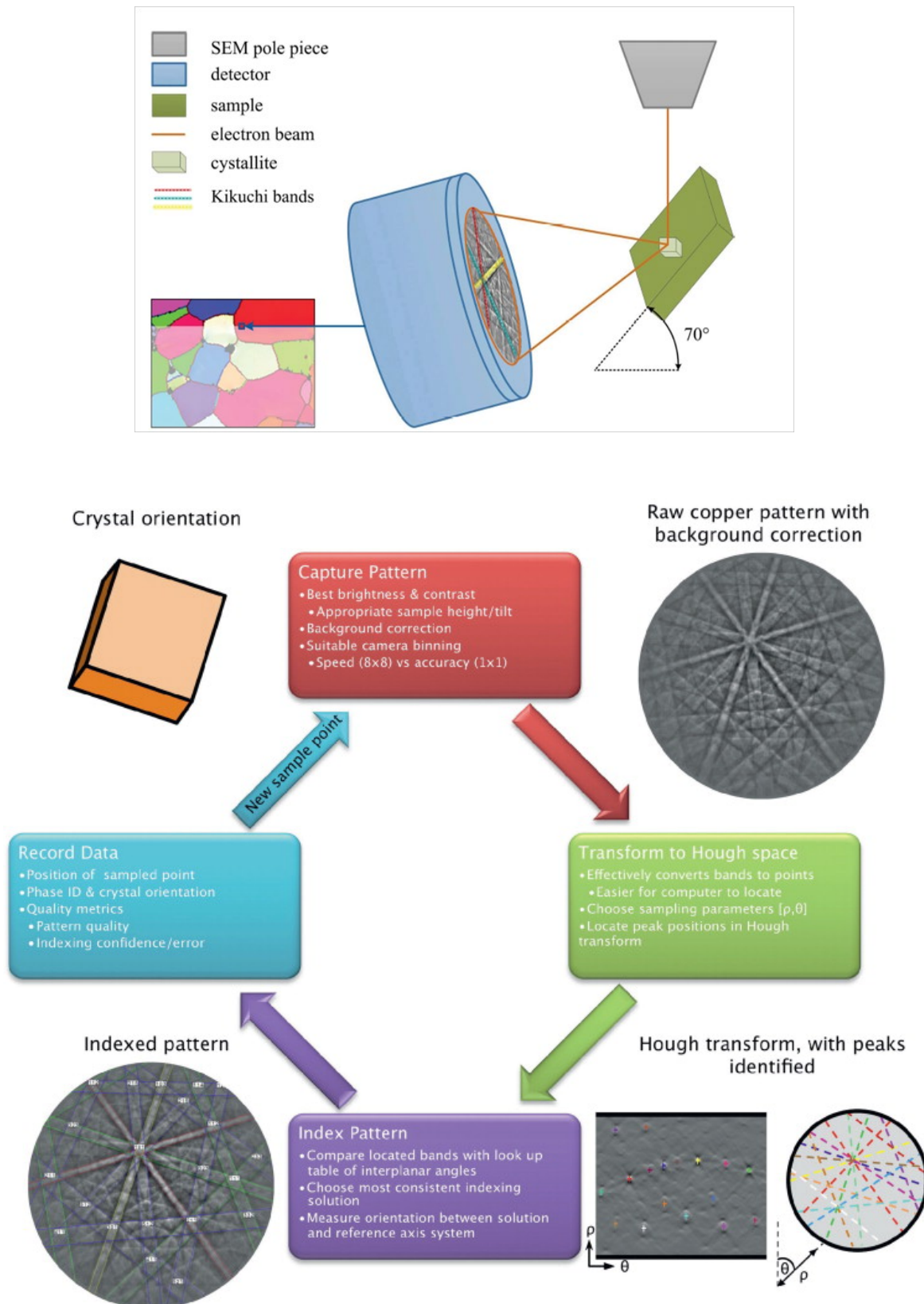


Figure 2.3 Set-up and principle of data acquisition for EBSD measurement in a polycrystalline material.; Overview of EBSD indexing procedure showing pattern capture through to determination of crystal orientation [90].

2.2.3. Transmission electron microscopy (TEM)

Historical development of Transmission Electron Microscope (TEM) was backed by the idea to overcome the limitations in image resolution in optical microscopes, which is limited by the visible light wavelength. The probe used in TEMs is high energy electrons with drastically reduced wavelength of the order of pm. For instance, value of electron wavelength is ~ 0.0025 nm for 200 keV electrons. In real situation, the resolution is limited to ~ 0.1 nm because of the aberrations in the objective lens contrast transfer function in electron microscopes. However, it is still much less (orders of magnitude smaller) than the typical wavelength of visible light. This small wavelength is the key to achieve atomic level resolution in materials. The image of the TEM instrument with schematic is shown in Fig. 2.4.

The contrast in TEM image is generated through the scattering of the incident electron beam by the specimen. The amplitude and phase of incoming electron wave changes as it travels through the specimen and both this phenomenon give rise to image contrast. In most of the cases, both types of contrast actually contribute to image formation but one tries to dominate the effect caused by the other. Amplitude contrast results from variations in mass or thickness or both in the sample. Phase contrast arises when multiple diffracted beams are allowed along with direct beam to form an image. HRTEM lattice imaging is a phase-contrast imaging technique.

In the present work, samples were characterized using a 200 kV high-resolution transmission electron microscope (HRTEM, of make: Carl Zeiss; and model: LIBRA 200FE). The information limit of the microscope is 0.13 nm. The diameters of the particles were measured using ImageJ software [91] from TEM images taken in bright-field mode.

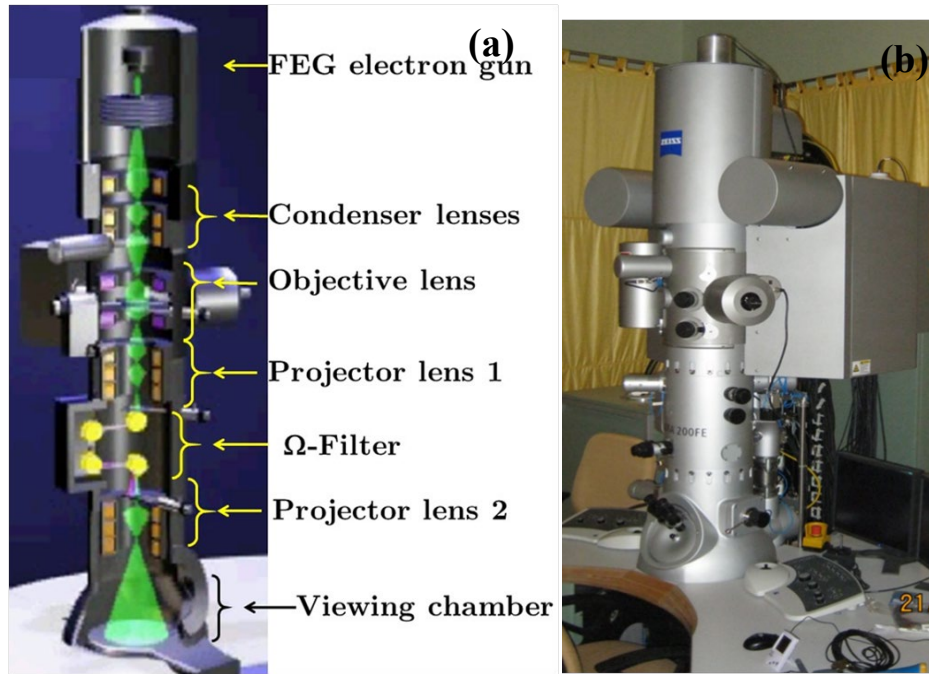


Figure 2.4 Shows (a) TEM schematic [33] and (b) TEM instrument used in the present study.

2.2.4. Vickers Hardness Test

Hardness is a measure of a materials resistance to plastic deformation or the measure of ability to counter penetration of another body. The indenter in Vickers hardness test is square based diamond pyramid with an included angle of 136° . The Vickers hardness number is computed from

$HV = F/A$ where F is the force applied and A is the indentation area

Which can be expressed as $HV = (2 * P \sin(\alpha/2)) / d^2 = 1.844 * P / d^2$

Where P = load, Kgf; d =mean diagonal of the impression and α = face angle of the diamond = 136° .

The Vickers hardness testing machine consists of a support for the specimen and provides for the indenter and the specimen to be brought into contact gradually and smoothly, under a predetermined load (Fig. 2.5) (In this study, 10 kg load was used). This load dwells for a fixed period of time (10 s dwell time was kept for the present work). In general, a measuring microscope is fixed on the machine such that the impression in its optical field is readily traced. The diagonal lengths of the indentation are measured.

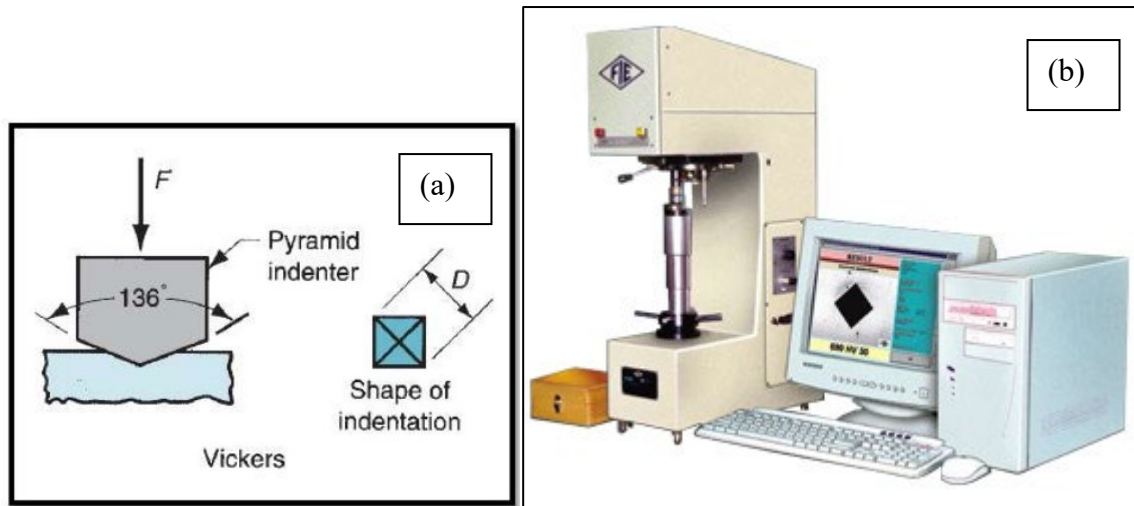


Figure 2.5 Vickers hardness tester (a) schematic of indentation process [92] and (b) the instrument

Hardness measurements were carried out in the ODS alloy for a comparison study and to correlate with the microstructure using a Vickers Hardness testing machine (make-FIE) using a load to 10 kg. The Vickers hardness values are normally presented with unit as HV followed by a number which presents the load applied in kg.

2.2.5. SRIM (Kinchin Pease to NRT consideration in TRIM) for irradiation damage study

Neutron –matter interaction can lead to several processes as follows: elastic scattering of the neutrons, transmutation through absorption of neutrons and inelastic scattering via energy transfer [91]. The energy transfer during irradiation can create knock-on damage. In 1955 Kinchin et al. [93] did a thorough review on irradiation damage and identified the effect of irradiation of various forms. As the high-energy sources emerged and fission reactors were developed, research activities improved the basic understanding of the mechanisms involved [94,95]. With the aid of the Transmission Electron Microscope (TEM), direct study of irradiation induced defects became possible [96] ([97] describes in more detail). Computer simulation with molecular dynamics, guided to probe the atomistic detail of irradiation damage. Simulating large volumes (needed to capture the complete nature of irradiation damage) through computation was very expensive. So, larger-scale models became reality only after the development of better efficient models and faster computers in the 1980s [98,99].

If an energetic particle collides with a nucleus, damage is produced. If sufficient energy is transferred during ballistic collision and atom gets displaced from its equilibrium lattice site, then a primary knock-on atom (PKA) is created and a vacant site is left behind.

Passage of the PKA through the lattice produces additional knock-on atoms. Finally the knock-on atom slows down and stop and a self-interstitial atom (SIA) defect is generated; Vacancy and interstitial formed together is called a Frenkel pair. A PKA with sufficiently high-energy can displace several atoms, forming a displacement cascade. In order to quantify the damage imparted, displacements per atom (dpa)-concept is introduced. Total number of the displacements is thus averaged as dpa and calculated using the modified Kinchin-Pease formulation [93], usually referred to as the Norgett, Robinson, and Torrens (NRT) model [100] as given in equation 2.1(for a single PKA):

$$N_d = \frac{\kappa E_{damage}}{2 E_d} = \frac{\kappa (T - \eta)}{2 E_d}$$

Equation 2.1

Where, T: total energy of the PKA; η : energy lost in the cascade through electron excitation process, and E_{damage} : energy available to generate atomic displacements by elastic collisions and E_d : threshold energy for displacement. The displacement efficiency, κ is 0.8. Once this estimate of number of subsequent displacements produced from a single energetic collision is available, the total dpa can be calculated by integrating the incident particle flux, possible PKA energies and the probability of collision in a time interval [101]. Equation 2.2 is used to estimate dpa from SRIM –damage events outputs in terms of no. of vacancies generated per ion per Å.

$$dpa = \frac{No. of vacancies}{Ion \cdot \text{\AA}} \times \varphi \times \frac{1}{\rho}$$

Equation 2.2

Where φ is ion fluence (ions/cm²) and ρ is atomic density (atoms/cm³)

The stopping and range of ions in matter (SRIM) program a revised version of TRIM (transport of ions in matter) is a Monte Carlo simulation code extensively used to compute parameters related to ion implantation like the range, straggling of the implanted ion, sputtering efficiency, ionization and damage energies deposited in the matrix, displacement damage profiles in elemental, compound matrices, thin films and multilayers etc. As dpa is a standard measure of primary radiation damage production, SRIM is mostly to determine the dpa associated with irradiation study. Damage calculation is performed through two options: i) quick damage or ii) full cascades. The former uses the Kinchin-Pease formalism. Besides, SRIM program provides detailed position coordinates and

instantaneous velocities of incident ion and recoils that can be used for computing beam sizes through foils and spatial correlation between vacancy and interstitial excesses.

In the present study, damage was calculated with the aid of SRIM using the above model with 40 eV displacement energy following the reference [102]; 99,999 ions were simulated in the SRIM 2013 version. The damage in dpa was calculated from the VACANCY.txt output; by summing the vacancies due to ions and recoils, multiplying by the ion dose (ions cm⁻²) and dividing by the number of atoms in a 1 cm² area by 1 Å thick layer, 8.48×10^{14} for Fe.

2.2.6. Ion irradiation facility: JANNuS

The JANNuS facility (Joint Accelerator for Nanosciences and Nuclear Simulation) is a triple beam facility which couples three ion accelerators. The facility is dedicated for simulating neutron damage in reactor structural materials as well as fuel [103]. It is a complementary irradiation tool with the OSIRIS research reactor in Saclay and the JHR European reactor, which is being constructed at CEA Cadarache. JANNuS couples a 3 MV Pelletron accelerator (ÉPIMÉTHÉE line) equipped with a multi-charged ECR ion source, a 2.5 MV Pelletron accelerator with an RF ion source (PANDORE line), and a 2 MV Pelletron Tandem accelerator (JAPET line) [103]. Associated with the complementary JANNuS Orsay facility, this platform is the only one of its kind in Europe (Fig. 2.6) and is used to:

- simulate neutron-induced ballistic damage and atom production (nuclear reactions) in nuclear materials using ion beams [103];
- tailor the properties of materials in a fully controlled way and to synthesize new phases using ion implantation or irradiation [103];
- quantify the evolution of chemical composition and microstructure of irradiated materials using available on-line ion beam analysis techniques [103];
- promote training and teaching activities in the field of ion/matter interaction [103];
- strengthen interactions between experimentalists and scientists that develop analytical models for the behavior of irradiated materials on scales ranging from nanometric (atom displacement) to macroscopic (evolution of physical, chemical, and mechanical properties) [103].

The alloy Fe-0.2Ti-0.3Y₂O₃ and Fe-14Cr-0.2Ti-0.3Y₂O₃ were irradiated using 5 MeV Ni²⁺ ion beam. The irradiation induced damage varied with depth of sample forming a profile like Fig. 5.1. The simulated damage profile has a peak damage of 150 dpa near 1.5 μ m producing a dose of 40 dpa at the surface (Refer Fig. 5.1). The above irradiation was carried out at 700 °C and 600 °C at JANNUS irradiation facility.

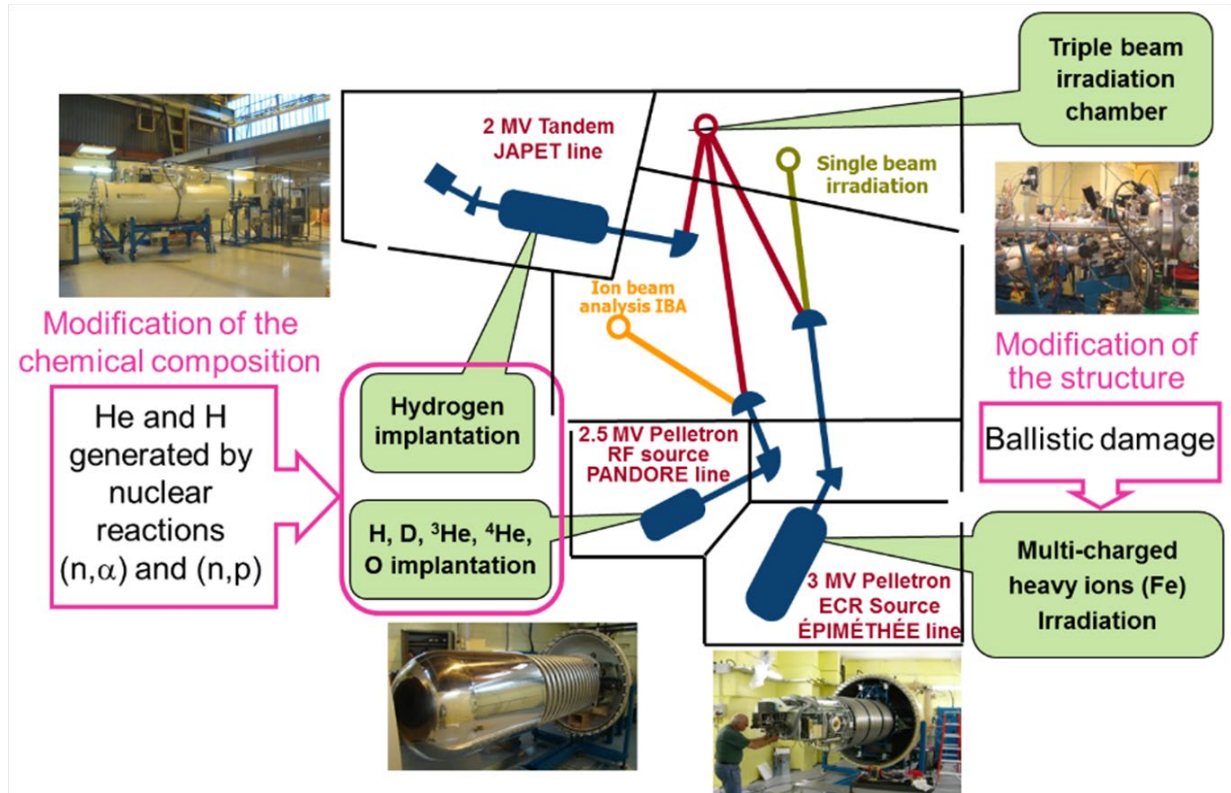


Figure 2.6 JANNUS ion irradiation facility [103]

2.2.7. Cold Rolling

In metalworking, rolling is a metal forming process in which metal stock is passed through one or more pairs of rolls to reduce the thickness. The amount of strain introduced determines the hardness and other material properties of the finished product. During rolling, If the temperature of the metal is above its recrystallization temperature, then the process is known as hot rolling and if the temperature of the metal is below its recrystallization temperature, the process is known as cold rolling. The cold rolling process Schematic is given in Fig. 2.7.

Manufacturing of ODS alloy tubes from extruded hollow to final size tube involves many stages of cold rolling with intermediate annealing. This imparts appreciable effect in alloy microstructure and texture evolution. In the present study, 18 Cr ODS alloy rod was

sliced and the sheets were subjected to different amount of cold rolling to study the texture as a function of amount of cold work.

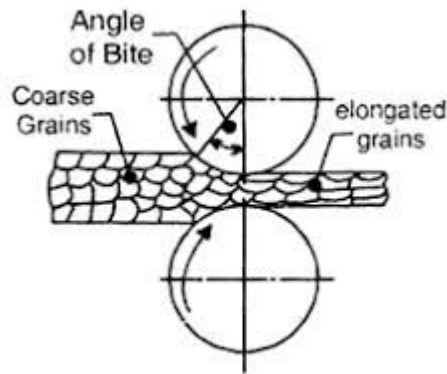


Figure 2.7 Cold rolling process schematic

2.2.8. Vacuum annealing

The 18 Cr ODS samples were annealed in a vacuum furnace, make-M/s Hind High Vac (P) Ltd. Bangalore. The operating temperature of the furnace is 1250 °C with uniformity of $\pm 5^\circ$ above 600 °C. The furnace is resistively heated via 12 numbers of graphite type heaters. The working vacuum of the furnace is 5×10^{-5} mbar. Figure 2.8 shows the image of the vacuum annealing furnace used for annealing in the present study.



Figure 2.8 Vacuum furnace used for annealing in present study.

Chapter 3

Study of microstructure and texture in high Cr ODS alloys

3.1. Introduction

Oxide dispersion strengthened (ODS) steels have been considered as candidate clad tube material in the future SFRs (sodium cooled fast reactor). The fabrication process of the final size clad tubes involves hot extrusion of the bar prepared from mechanically alloyed powder followed by cold forming steps. Intermediate heat treatment is also performed to soften the material and avoid damage during further fabrication steps. It also helps in reducing the crystallographic and morphological anisotropy that is one of the major issues observed during manufacturing of the ODS tubes [104]. During the fabrication stages, microstructures of alloys are severely affected and different types of texture are produced. Analysis of the changes of microstructure and texture during cold-forming and the subsequent annealing are essential for optimizing the fabrication procedure in order to obtain the materials with high performance. Because of the tremendous industrial importance, many studies have been conducted by several researchers and reports are available on recrystallization behaviors of ferritic steels, like interstitial free (IF) steel [105–107] and silicon steel [108–111]. However, fewer works on recrystallization texture of cold-rolled ODS ferritic steels have been published [73–76].

The aim of the present work was to study the microstructure and texture in the different model ODS alloys of composition Fe-0.3Y₂O₃, Fe-0.2Ti-0.3Y₂O₃, Fe-14Cr-0.2Ti-0.3Y₂O₃ and the synergistic effect of cold work and temperature in development of texture in a commercial 18Cr- ODS alloy.

3.2. Experimental

The model ODS alloys were prepared by using mechanical alloying and hot extrusion method. High pure elemental powders of Fe, Ti, Cr, and Y₂O₃ were taken for the compositions of Fe-0.3Y₂O₃, Fe-0.2Ti-0.3Y₂O₃ and Fe-14Cr-0.2Ti-0.3Y₂O₃. The Y₂O₃ powder (Alfa Aesar) with an average particle diameter of ~ 22 nm was taken for ball milling and the crystal structure of the Y₂O₃ was body centered cubic (bcc). The powders were mechanically alloyed in ball milling (Simolayer CM-08) in Argon atmosphere for four hours at 1000 rpm with a ball to powder ratio of 10:1. Two mechanically alloyed powders with the composition of Fe-0.3Y₂O₃ and Fe-0.2Ti-0.3Y₂O₃ were extruded at 1050 °C followed by annealing at 950 °C for two hours and then air cooled. Another

mechanically alloyed powder with the composition of Fe-14Cr-0.2Ti-0.3Y₂O₃ was extruded at 1150 °C and was quenched. Quenched sample was annealed at 1050 °C for 0.5 h and tempered at 750 °C for two hours. Air cooling was done in order to obtain a well defined microstructure. Finally consolidated model ODS rods of 12 mm diameter of three different alloy composition Fe-0.3Y₂O₃ (0.03 wt % C), Fe-0.2Ti-0.3Y₂O₃ (0.02 wt % C) and Fe-14Cr-0.2Ti-0.3Y₂O₃ (0.02 wt % C) were prepared. The O, C and N content of the alloys are measured using inductively coupled plasma mass spectrometry (ICPMS) and composition is tabulated in Table.3.1.

The 18 Cr ODS alloy bar were prepared by milling and extrusion. Milling was carried out by using argon atomized 18Cr steel powder (with an average size of 90 µm produced at ARCI, Hyderabad) and nano yttria powder (30–50 nm size, 99.95% purity supplied by M/S Inframat Advanced Materials, LLC, USA) in a high energy horizontal attritor mill (Simoloyer CM-08, ZOZ GmbH, Germany) for 6 hours at 700 rpm with a ball to powder ratio of 7.5:1. After degassing at 450 °C, sealed cans were extruded at 1150 °C. The extruded bar was annealed at 1100 °C for 1h.

The O, C and N content of the alloy was measured using ICPMS technique and is given in Table 3.1. The bar was sliced twice along the longitudinal direction to generate three sheets for three different cold work samples. The percentage cold work was measured as a reduction in sheet thickness. These sheets were subjected to cold rolling by 30, 40 and 50 % respectively. Each sheet was further sliced into three pieces and annealed at 1050, 1150 and 1250 °C respectively in vacuum for 30 minutes followed by furnace cooling. In this process, nine samples are produced with different amount of cold work and annealing treatment for the study to understand evolution of microstructure and texture with cold work and temperature.

Orientation imaging microscopy (OIM) was carried out *via* electron back scattered diffraction technique (EBSD – make: Oxford Instruments, Nordlys Nano) equipped with the SEM to generate the crystal orientation map from the longitudinal section of extruded and annealed rods. The OIM maps were studied in the as cold worked sample and after annealing. The results were compared. Channel 5 software [112] was used for texture and recrystallization study from misorientation profiles. Recrystallization analysis was carried out using misorientation analysis. Critical misorientation for subgrain and recrystallized grain identification was set as 1 and 7 ° respectively. The samples for OIM study were prepared by mechanical polishing (using SiC emery papers of different grit sizes up to

diamond finish followed by electropolishing in a solution of methanol, 2-butoxy ethanol and perchloric acid in 7:2:1 ratio at 25 V and -35 °C). Hardness measurements were carried out in the ODS alloy using a Vickers hardness testing machine (make-FIE) using a load to 10 kg to correlate the hardness with microstructure.

Table 3.1 Alloy composition with bulk oxygen, carbon and nitrogen content of the four alloys (in weight percent) measured using ICPMS.

Alloy	Ti	Cr	Y ₂ O ₃	Al	W	O (%)	C (%)	N (%)	Fe
Fe-0.3Y ₂ O ₃	-	-	0.3	-	-	0.46	0.03	0.019	Balance
Fe-0.2Ti-0.3Y ₂ O ₃	0.2	-	0.3	-	-	0.47	0.02	0.009	Balance
Fe-14Cr-0.2Ti-0.3Y ₂ O ₃	0.2	14	0.3	-	-	0.38	0.02	0.006	Balance
Fe-18Cr-0.3Ti-0.3Y ₂ O ₃	0.3	18	0.3	0.05	2.2	0.12	0.03	0.016	Balance

3.3. Results

3.3.1. Model ODS alloys

3.3.1.1. Hardness study

Hardness study was carried out using Vickers hardness tester and the average values obtained is tabulated in Table 3.2. The hardness value of alloy Fe-14Cr-0.2Ti-0.3Y₂O₃ was appreciably greater than the hardness of the other two alloys of composition Fe-0.3Y₂O₃ and Fe-0.2Ti-0.3Y₂O₃.

R. Vijay *et al.* [87] studied the hardness of ODS alloy of composition Fe-0.35Y₂O₃, Fe-0.2Ti-0.35Y₂O₃ and compared with pure Fe. Their results showed that pure Fe has a bulk hardness value of 110 HV₅ (HV₅: Hardness Vickers with applied load 5 kg) which increases to 140 and 199 HV₅ for Fe-0.35Y₂O₃ and Fe-0.2Ti-0.35Y₂O₃ respectively. The authors reported that the hardness of iron increases when fine Y₂O₃ dispersoids are present as in Fe-0.35Y₂O₃. Further increase of hardness in Fe-0.2Ti-0.35Y₂O₃ is obviously caused because of grain size refinement and reduced size and increased volume fraction of the Y₂Ti₂O₇ oxide particles as compared to the Y₂O₃ dispersoids in Fe-0.35Y₂O₃ alloy. In the present work, upon Ti addition, the hardness of the alloy has increased significantly and it is due to oxide particle refinement. Even finer microstructure with finer oxide particles upon Cr addition leads to further increase of hardness which will be discussed in chapter 4 (section 4.3.1).

Table 3.2 Hardness values of three different model ODS alloys

Alloy	Vickers Hardness (HV ₁₀)
Fe-0.3Y ₂ O ₃	163
Fe-0.2Ti-0.3Y ₂ O ₃	195
Fe-14Cr-0.2Ti-0.3Y ₂ O ₃	251

3.3.1.2. Microstructure and recrystallization

Figure 3.1(a) and 3.1(b) shows the OIM (orientation imaging microscopy) images of the longitudinal and transverse sections of the Fe-0.3Y₂O₃ ODS rod. Equiaxed grains are observed in transverse section. Grains along longitudinal direction do not show any elongation. OIM images of the longitudinal and transverse sections of the Fe-0.2Ti-0.3Y₂O₃ ODS rod is shown in Fig. 3.1(c) and 3.1(d). Both the sections were found with equiaxed grains.

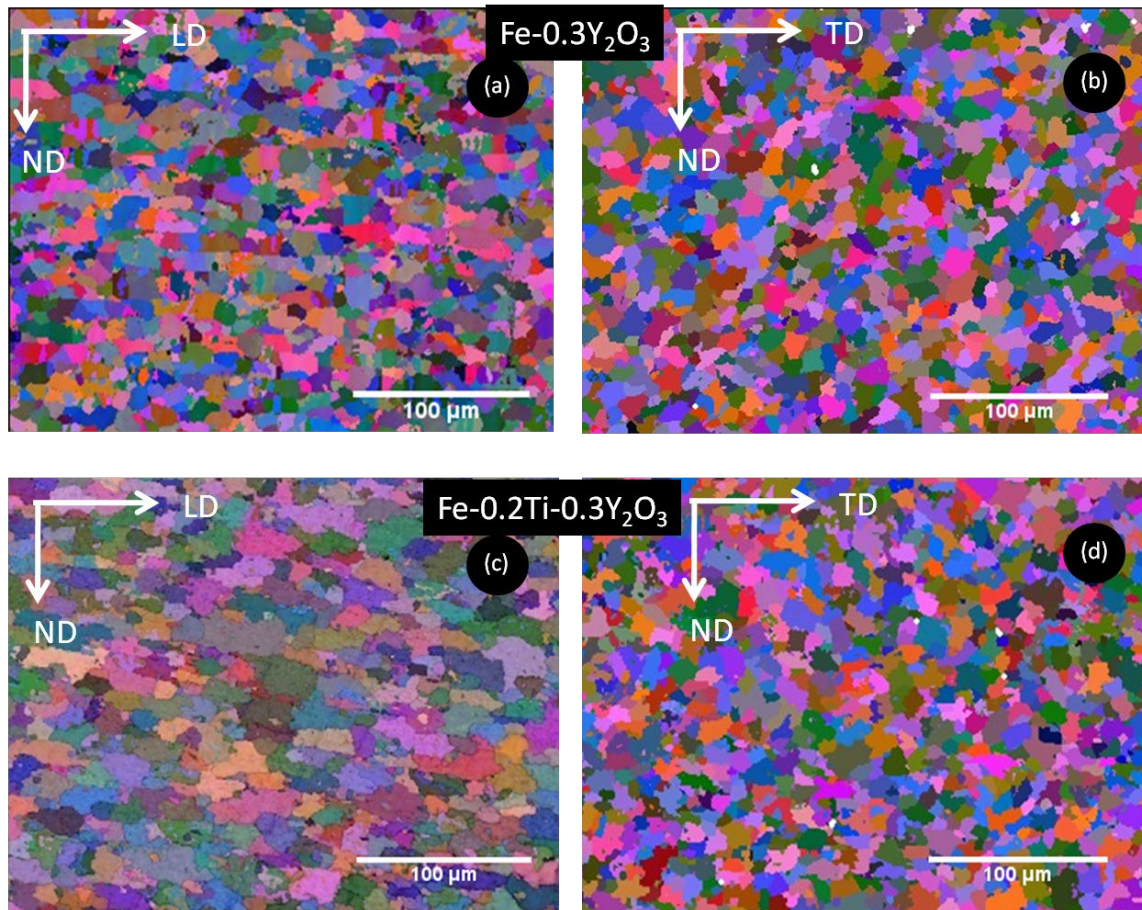


Figure 3.1 EBSD-OIM map from (a), (c) longitudinal and (b), (d) transverse section of the ODS alloy of composition $\text{Fe-0.3Y}_2\text{O}_3$ and $\text{Fe-0.2Ti-0.3Y}_2\text{O}_3$ respectively.

OIM images of the longitudinal and transverse sections of the $\text{Fe-14Cr-0.2Ti-0.3Y}_2\text{O}_3$ ODS rod is shown in Fig. 3.2(a) and 3.2(b). Both the sections were found with equiaxed grains. From high magnification images, grain size banding was observed. From the longitudinal section image at higher magnification (Fig. 3.2 (c)), band of finer grains along longitudinal direction are clearly observed.

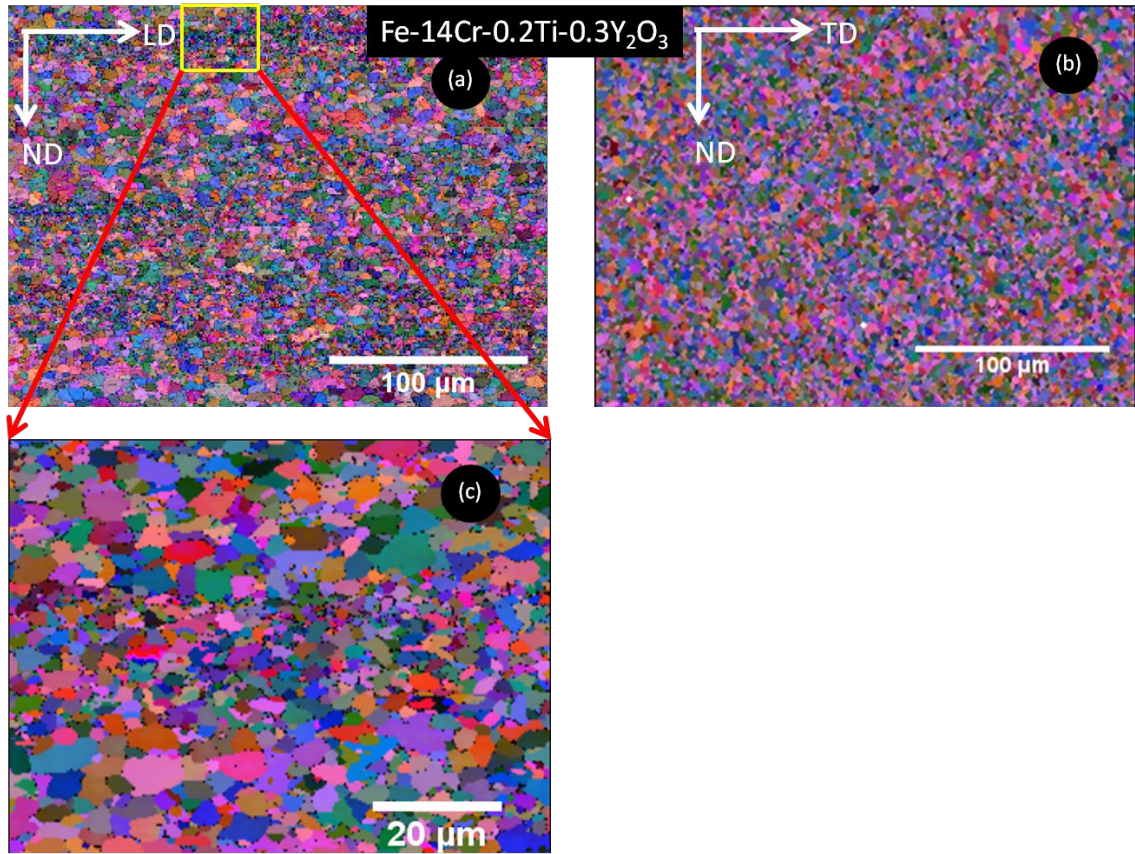


Figure 3.2 EBSD-OIM map from Fe-14Cr-0.2Ti-0.3Y₂O₃ alloy (a) longitudinal and (b) transverse section, and (c) at higher magnification which shows fine grain band.

The average grain size was found to be 9.0 μm for both the Fe-0.3Y₂O₃ and Fe-0.2Ti-0.3Y₂O₃ alloys with a standard deviation of 3.8 and 5.7 μm respectively whereas Fe-14Cr-0.2Ti-0.3Y₂O₃ alloy had a finer microstructure with average grain size of 4 μm with a standard deviation of 1 μm . Figure 3.3 (a) shows the grain size distribution for Fe-0.3Y₂O₃ alloy. The average grain size is 9 ± 4 μm with a range from 3-21 μm . Figure 3.3 (b) shows the grain size distribution histogram for Fe-0.2Ti-0.3Y₂O₃ alloy with dominated occurrence of finer grains of size around 5 μm although the average grain size remains 9 ± 5 μm with a range from 3-34 μm . Figure 3.3 (c) shows the grain size distribution for Fe-14Cr-0.2Ti-0.3Y₂O₃ alloy where the histogram is squeezed within a range of 3-12 μm grain size having average grain size as 4 ± 1 μm diameter. (From the OIM-EBSD mapped area, recrystallization fraction was studied and the values are tabulated in Table 3.4).

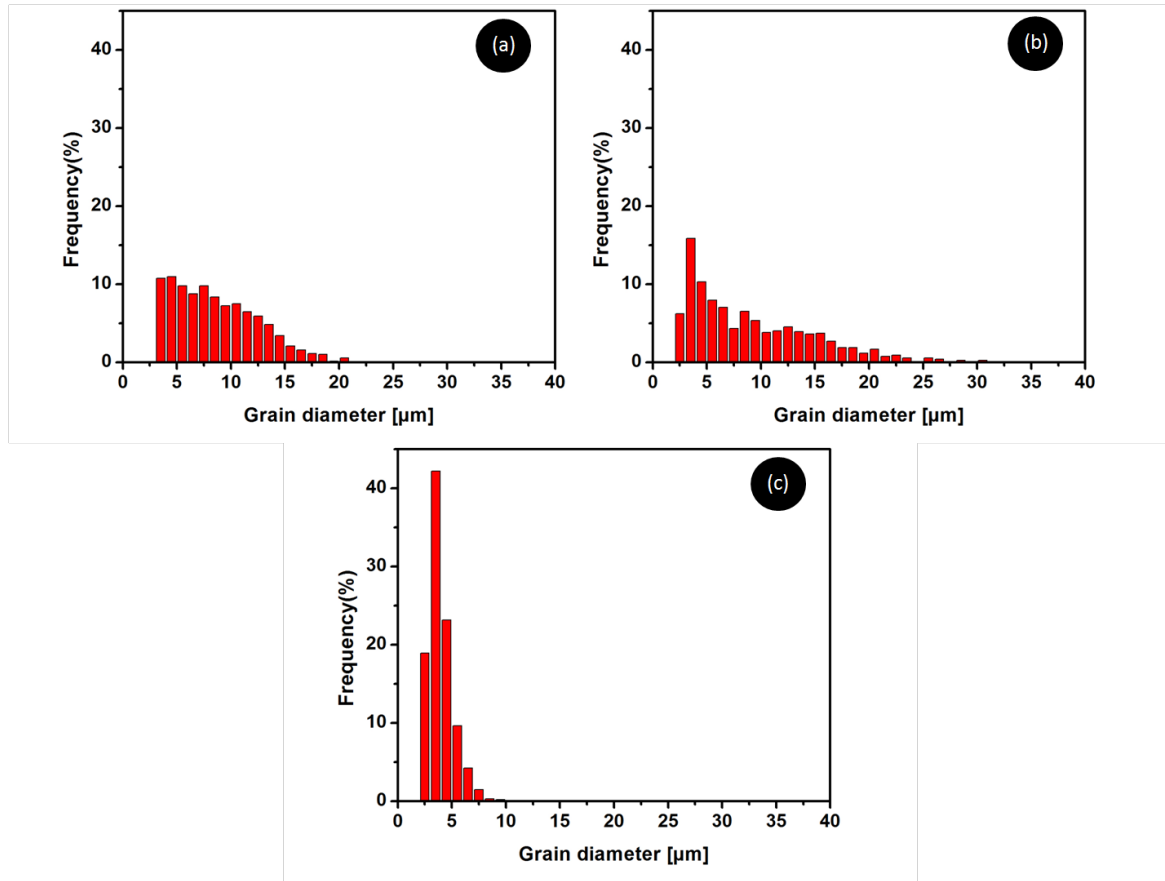


Figure 3.3 Grain size distribution histograms for alloy (a) Fe-0.3Y₂O₃, (b) Fe-0.2Ti-0.3Y₂O₃ and (c) Fe-14Cr-0.2Ti-0.3Y₂O₃ respectively

3.3.1.3. Texture study

Texture was studied in all the three model ODS alloys and presented using pole figures as shown in Fig. 3.4. Figure 3.4 (a) shows the pole figure for Fe-0.3Y₂O₃ alloy and typical alpha texture with $\langle 110 \rangle \parallel \text{RD}$ is observed. Figure 3.4 (b) shows the pole figure for Fe-0.2Ti-0.3Y₂O₃ alloy alpha texture with $\langle 110 \rangle \parallel \text{RD}$ is observed. The texture was nearly random in Fe-14Cr-0.2Ti-0.3Y₂O₃ alloy (as the maximum intensity was 1.39 only) showing absence of texture in the alloy as can be checked from pole figure shown in Fig. 3.4 (c).

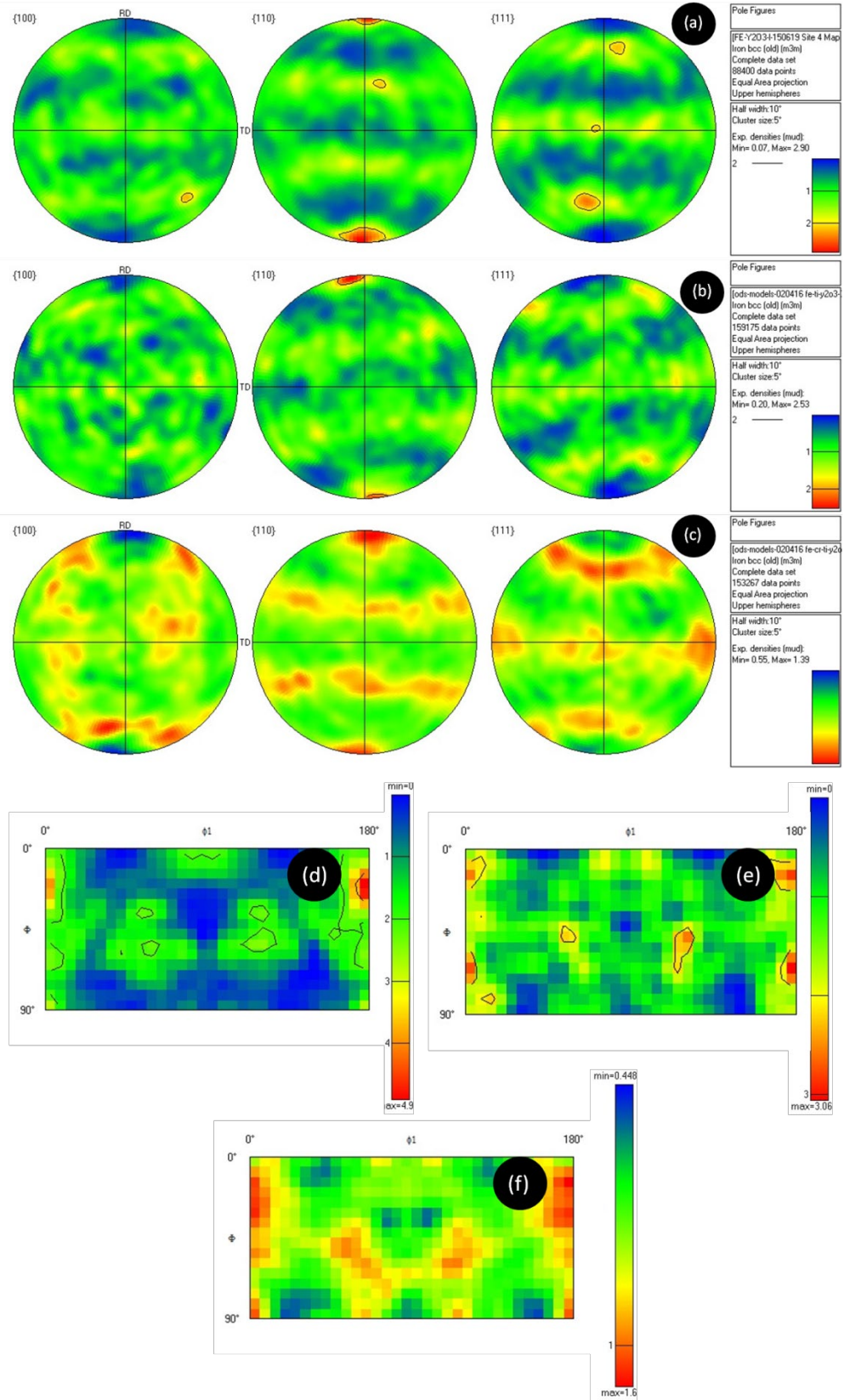


Figure 3.4 Pole figure obtained from (a) Fe-0.3Y₂O₃; (b) Fe-0.2Ti-0.3Y₂O₃ and (c) Fe-14Cr-0.2Ti-0.3Y₂O₃ ODS alloy for {100}, {110} and {111} planes and ODF $\phi_2 = 45^\circ$ section of (d) Fe-0.3Y₂O₃; (e) Fe-0.2Ti-0.3Y₂O₃ and (f) Fe-14Cr-0.2Ti-0.3Y₂O₃ ODS alloy.

The ODF sections of $\phi_2 = 45^\circ$ are also shown in Fig. 3.4 (d), 3.4(e) and 3.4(f) for the alloys Fe-0.3Y₂O₃, Fe-0.2Ti-0.3Y₂O₃ and Fe-14Cr-0.2Ti-0.3Y₂O₃ respectively. Similar to the pole figure, the ODF section of alloys Fe-0.3Y₂O₃ and Fe-0.2Ti-0.3Y₂O₃ are found with some excited components of the alpha fibre but the intensity decreases (from maximum value of 4.9) to 3. In case of the Fe-14Cr-0.2Ti-0.3Y₂O₃ alloy, the intensity becomes maximum (1.6 times random) which shows almost absence of texture in the alloy.

3.3.2. Commercial 18Cr ODS Alloy

3.3.2.1. Hardness Study

In order to study the mechanical strength/properties of the 18Cr ODS alloys, the hardness measurements were carried out for the extruded and annealed rod and cold worked alloys. Vickers hardness for the alloys with different conditions (% of cold work, and extruded and annealed) are tabulated and given in Table 3.3.

During cold work, a material deforms plastically at a temperature $< 0.4T_m$ where T_m is the melting point of the material which results in increase of hardness of a material. This is essentially due to introduction of a high density of crystal imperfections like dislocations. During the early stages of plastic deformation, slip occurs on primary glide planes and dislocations form coplanar arrays. As deformation proceeds, cross slip and multiplication takes place which soon develops into tangled networks restricting further movement of dislocations. This gets reflected in material hardness i.e. material hardness increases with amount of cold work imparted onto it.

The cold worked state exhibits higher internal energy than undeformed material. With increasing temperature, the cold worked state become more and more unstable and eventually leads to a strain-free softened condition. This is known as annealing which occurs through recovery, recrystallization and grain growth. Recovery is a process by which deformed grains can reduce their stored energy by the removal or rearrangement of defects in their crystal structure. Recrystallization replaces cold worked structure by a new set of strain-free grains. Treatment at more than recrystallization temperature leads to progressive increase in size of these strain-free grains which is called grain growth. Thus annealing process reduces dislocation density which decreases the hardness of the material. The ODS alloy final tube should not have strength anisotropy along axial and hoop direction. But tube manufacturing process involves cold working which produces elongated grains along working direction and hence anisotropy appears. In case of 9-Cr ODS, phase transformation is available at 1050 °C. Hence annealing at this temperature can nucleate fresh

equiaxed grains and anisotropy can be eliminated. But for 12 Cr-ODS, no such phase transformation is available. Hence the final tube is required to be recrystallized. But if recrystallization occurs at intermediate stage, further recrystallization at the final stage is prevented thus generating strength anisotropy in the final product. Hence, control of recrystallization for the 12Cr-ODS steel is much more difficult than that of alpha to gamma transformation for the 9Cr-ODS steel, because recrystallization is not reversible [113]. Although recrystallization is favorable to soften before cold rolling, recrystallization must be induced in the final heat treatment, because recrystallization in intermediate heat treatments prevent from further recrystallization in the final heat treatment. To prevent from premature recrystallization and subsequent strength anisotropy in final products, one-step annealing is not enough and two-step annealing in the intermediate heat treatments was introduced by Inoue *et al.*[113].

It has been reported by Inoue *et al.* in page no. 311-325 of ref [113] that hardness value should be less than 400 HV to avoid damage during manufacturing [114]. The typical hardness value of the final heat treated 9Cr-ODS fabricated in CEA, Saclay is ~ 360 HV₁[104].

In the present work, the extruded and annealed 18Cr ODS bar was having a hardness value of 360 HV₁₀. The hardness was similar in 30% and 40% CW sample with a value of 395 HV₁₀. Hardness further increased to 430 HV₁₀ in 50% CW sample. The increase in hardness with % CW showed the effect of work hardening in the alloy. With 30 % CW, annealing at 1050 °C did not show any change in hardness of the alloy suggesting retention of deformed microstructure only. Hardness decreased to 350 HV₁₀ and was similar in the 30% CW samples after annealing at 1150 °C and 1250 °C. This suggests that transformation of deformed microstructure towards recrystallization has initiated. With 40% CW, a slight reduction in hardness is noticed after annealing at 1050 °C as compared to the 40% CW sample. Hardness gets substantially reduced in 40% CW samples after annealing at 1150 °C and 1250 °C indicating similar behavior with the 30% CW and annealed samples. With 50% CW, annealing at lower temperature of 1050 °C showed a pronounced reduction in hardness from cold worked state as compared to the reduction found in 30 or 40 % CW samples after annealing. This is possible because of the higher amount of cold work that was stored in the 50 % CW sample as the driving force required for recrystallization. Higher annealing temperature of 1150 °C and 1250 °C further reduced the hardness value to 314 HV₁₀. The hardness values obtained from the present study suggests that manufacturing is not advisable with annealing temperature of

1050 °C as the values were on the higher side. Manufacturing trials can be taken with annealing temperature of 1150 °C.

Table 3.3 Hardness of the 18Cr ODS alloys with different conditions of cold work and heat treatment conditions

Sample condition	Hardness (HV ₁₀)
Extruded & annealed	360
30 % CW	395
40 % CW	397
50 % CW	430
30 % CW-1050 °C	394
30 % CW-1150 °C	349
30 % CW-1250°C	350
40 % CW-1050 °C	389
40 % CW-1150 °C	326
40 % CW-1250 °C	315
50 % CW-1050 °C	382
50 % CW-1150 °C	314
50 % CW-1250 °C	314

3.3.2.2. Effect of cold work and annealing temperature on microstructure

In order to study the microstructure of the 18Cr ODS alloys with different conditions, OIM imaging was employed. The OIM map of hot extruded and annealed bar of 18Cr ODS alloy is presented in Fig.3.5 (a) and it shows presence elongated grains along the longitudinal direction of the bar. Channel5 software [112] was employed to analyse the OIM images and get the recrystallization fraction. The map showed that the bar microstructure was partially recrystallized (~ 40% recrystallized grains).

Figure 3.5 (b) shows the OIM map of the longitudinal section of the 30 % CW sheet of 18Cr ODS alloy. Elongated grains are observed along the longitudinal direction and 30 % recrystallized grains are found to remain. Figure 3.5(c) shows the OIM map of the longitudinal section of the 40% CW sheet of 18Cr ODS alloy. In longitudinal direction, the grains are found to be elongated. Only 15 % recrystallized grains were found with predominant deformation. The OIM map of 50 % CW sheet is shown in Fig. 3.5(d). Elongated deformed grains are visible. The microstructure is found with only 15 % recrystallized grains with rest of the grains as deformed.

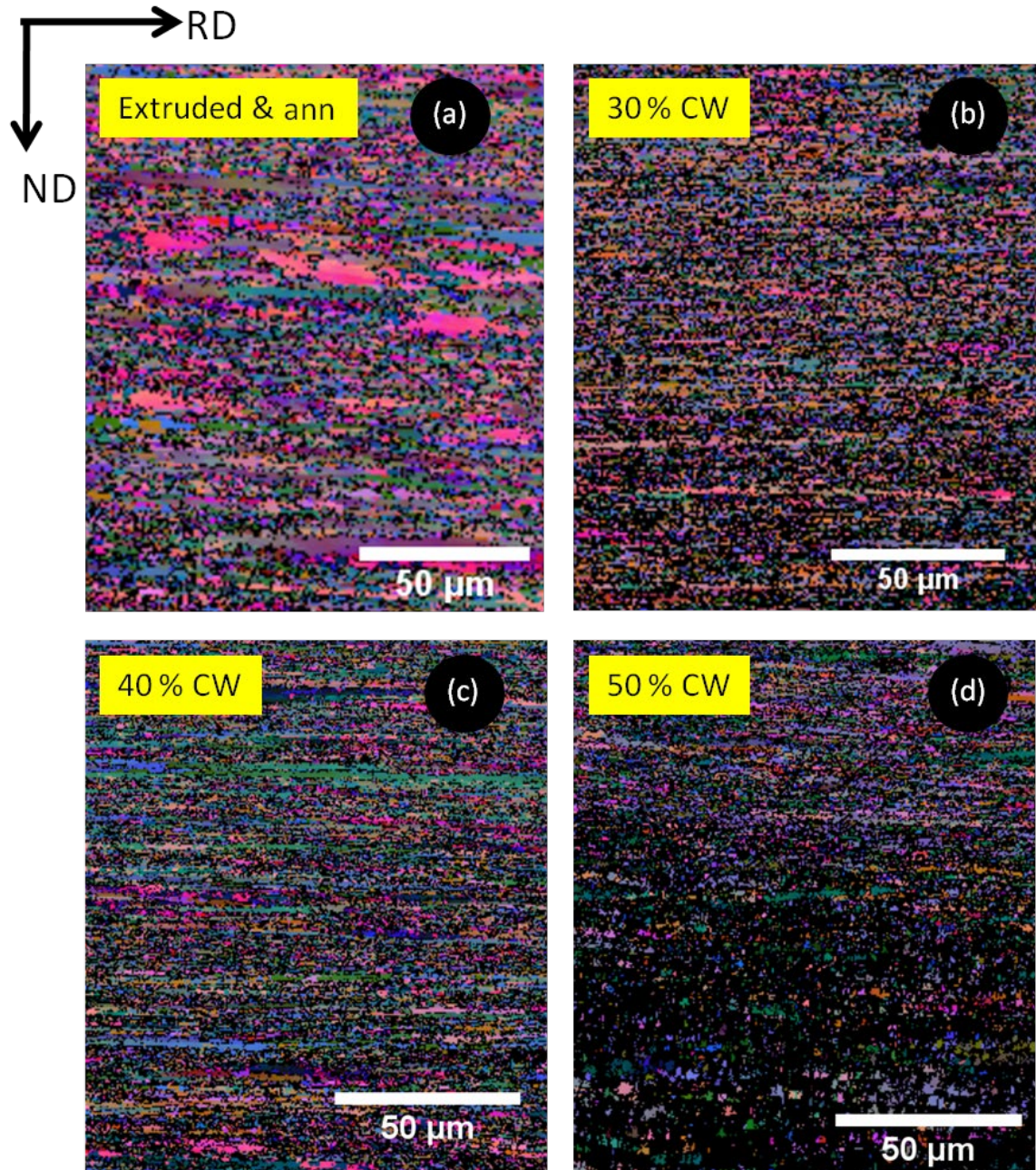


Figure 3.5 EBSD-OIM map from longitudinal section of (a) extruded and annealed rod, after (b) 30 %, (c) 40 % and (d) 50 % CW respectively

Figure 3.6(a) shows the OIM map of the 30% CW sheet after annealing at 1050 °C. The image shows fine deformed grains in different colors with some abnormally grown grain (in violet color). The black spots present the un-indexed regions. Figure 3.6(b) shows the corresponding recrystallization fraction map where the recrystallized fraction is shown in blue, substructured portion in yellow and deformed grains in red color. Figure

3.6(b) shows that the abnormally grown grain is fully recrystallized and the rest of the fine grains were partially recrystallized. Around 35% grains were recrystallized.

After annealing at 1150 °C, the OIM map shows drastically different microstructure with comparatively coarse grains (Fig. 3.6(c)). Majority of grains coarsened and some islands of finer grains survived. Figure 3.6(d) shows the recrystallization fraction map. The yellow color indicates presence of substructured grains. 61% grains were recrystallized with 15% in substructured form and rest 23% as deformed.

Effect of annealing at 1250 °C can be observed from Fig. 3.6(e). The grains were recrystallized and underwent substantial growth. Figure 3.6(f) shows the recrystallization fraction map. A considerable fraction of substructured grains transformed into recrystallized ones. Only ~ 10% grains were in deformed form.

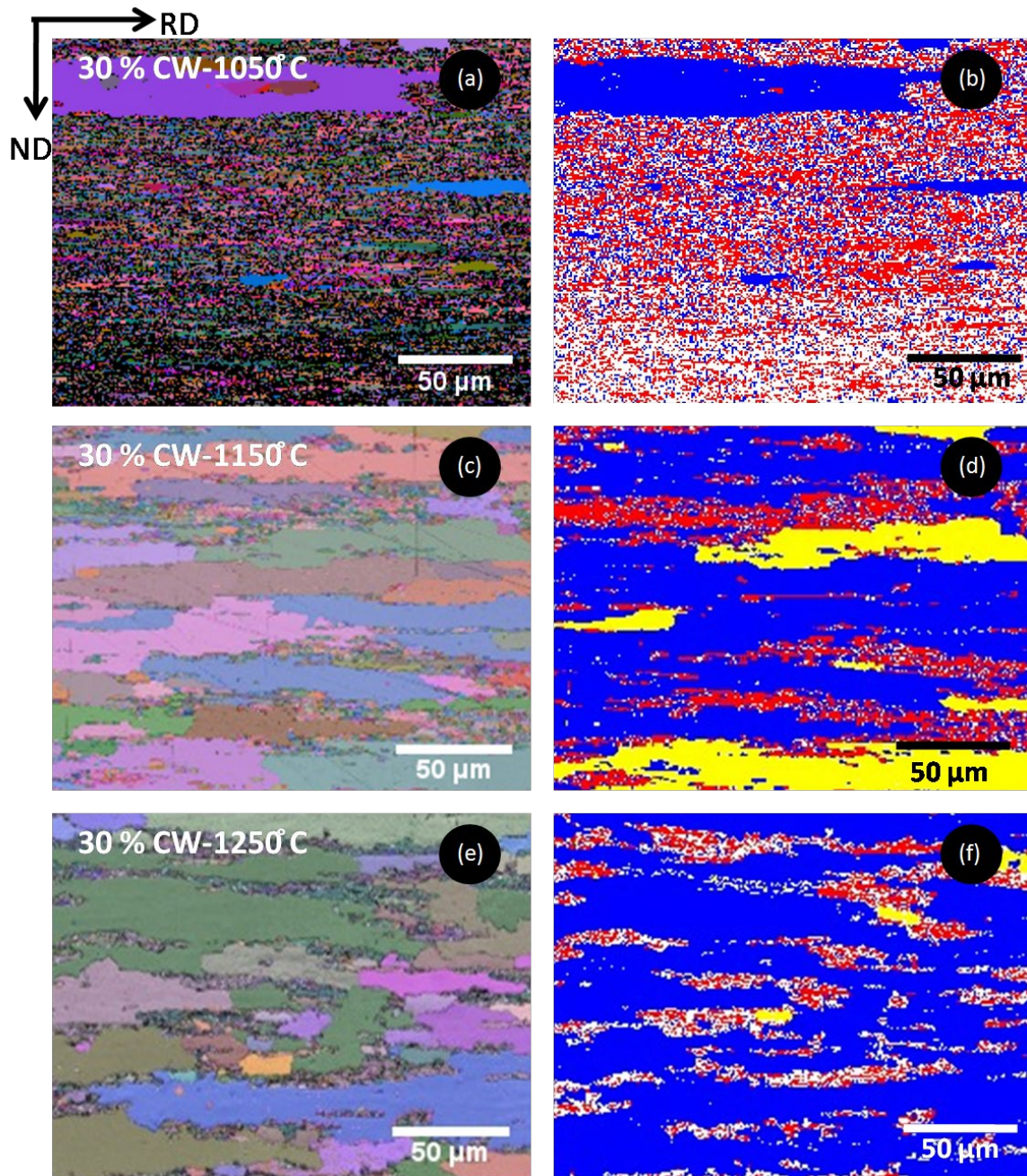


Figure 3.6 (a), (c), (e) Electron back scattered diffraction generated Orientation Imaging maps (EBSD-OIM) maps and corresponding (b), (d), (f) recrystallization mapping showing recrystallized portion in blue, subgrain in yellow and deformed portion in red of 30 % cold worked 18Cr-commercial ODS alloy after annealed at 1050, 1150 and 1250 °C respectively.

Figure 3.7(a) shows the OIM map of the 40% CW sheet after annealing at 1050 °C. Elongated grains in different colors are observed with abnormally coarse grain as found along the mid region of the image. Figure 3.7(b) shows the recrystallization map. Majority of the grains (68%) were found in deformed condition. At 1150 °C, coarse recrystallized grains can be observed with island of fine grains from Fig. 3.7(c) and (d).

Deformed fraction of grains (in red color) drastically reduced and around 62% recrystallized grains and 25% substructured grains were found. At 1250 °C, further coarse grains with 75% recrystallized and 15% substructured form were present as shown in Fig. 3.7(e) and 3.7(f).

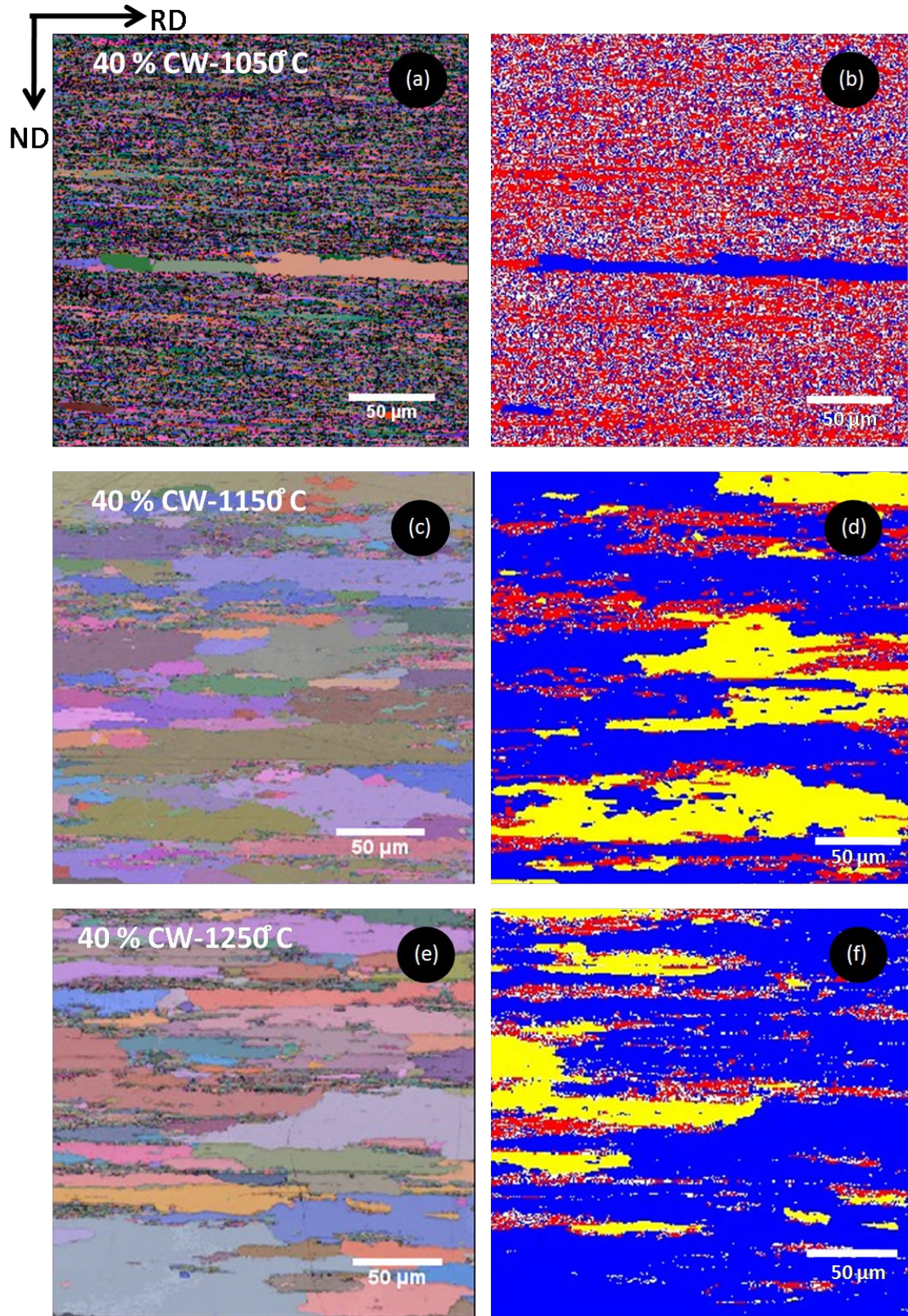


Figure 3.7 (a), (c) and (e) Electron back scattered diffraction generated Orientation Imaging maps (EBSD-OIM) maps and corresponding (b), (d) and (f) recrystallization mapping showing recrystallized portion in blue, subgrain in yellow and deformed portion in red of 40 % cold worked 18Cr-commercial ODS alloy after annealed at 1050, 1150 and 1250 °C respectively.

Figure 3.8(a) shows the OIM map of the 50% CW sheet after annealing at 1050 °C. A much higher fraction of the abnormally grown grains is found. The more number of adjacent coarse grains with comparatively less width shows that simultaneous initiation of recrystallization at many sites. Figure 3.8(b) shows the recrystallization map of the alloy 50% CW and annealed at 1050 °C. Few adjacent or trailing regions of such grains were found with substructured condition (with a small fraction of 0.5%). Around 46% grains were found recrystallized. After annealing at 1150 °C, deformed fraction drastically reduced and recrystallized and substructured fraction was 85 and 9% respectively (Fig. 3.8 (c) and 3.8(d)). Figure 3.8(e) shows OIM map of the 50% CW alloy after annealing at 1250 °C and the effects were clearly seen. Fully recrystallized elongated grains are observed (82%) and 17% were in substructured form. The fine grain islands almost disappeared. Deformed grains fraction was negligible (1%) as presented in Fig. 3.8(f).

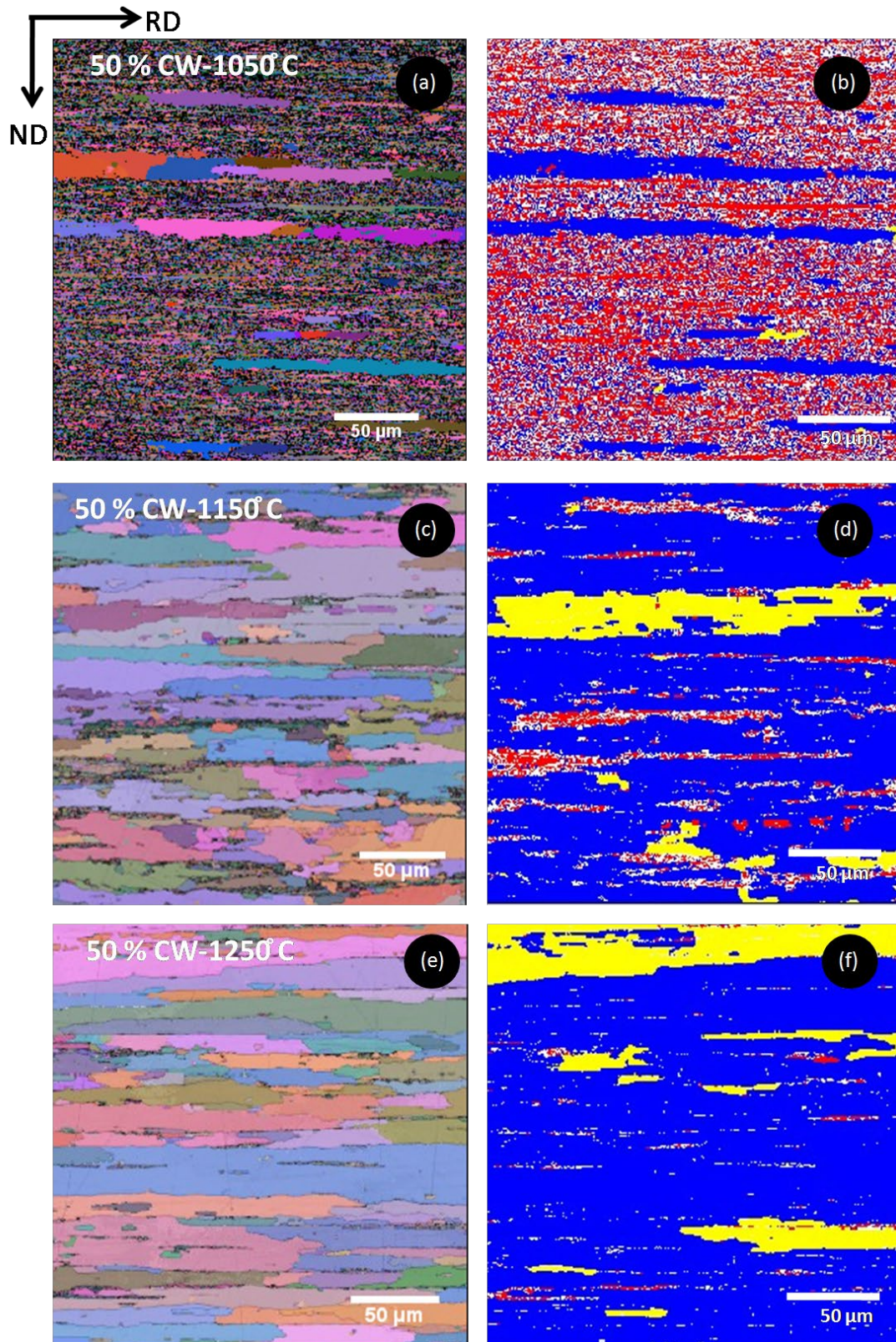


Figure 3.8 (a), (c) and (e) Electron back scattered diffraction generated Orientation Imaging maps (EBSD-OIM) maps and corresponding (b), (d) and (f) recrystallization mapping showing recrystallized portion in blue, subgrain in yellow and deformed portion in red of 50 % cold worked 18Cr-commercial ODS alloy after annealed at 1050, 1150 and 1250 °C respectively.

Table 3.4 Misorientation and recrystallization fraction for different conditions

Alloy	Condition	Fraction of grains with misorientation (0-15°)	Fraction (%)		
			deformed	subgrain	recrystallized
Fe-0.3Y ₂ O ₃	Extruded & annealed	-	92	4	4
Fe-0.2Ti-0.3Y ₂ O ₃			86	8	6
Fe-14Cr-0.2Ti-0.3Y ₂ O ₃			83	2	15
18-Cr ODS	As Extruded	42	60	-	40
	30 % CW	72	70	-	30
	40 % CW	68	85	-	15
	50 % CW	74	85	-	15
	30-1050	45	65	-	35
	30-1150	45	23	16	61
	30-1250	52	11	3	86
	40-1050	50	68	-	32
	40-1150	41	12	25	63
	40-1250	35	9	16	75
	50-1050	49	65	-	35
	50-1150	32	6	9	85
	50-1250	18	1	17	82

3.3.2.3. Effect of cold work and annealing temperature on texture

Fig. 3.9 shows some ideal orientation used for texture description in cubic materials plotted in $\Phi_2=45^\circ$ and 0° sections which were mainly used for the present study of texture in ODS

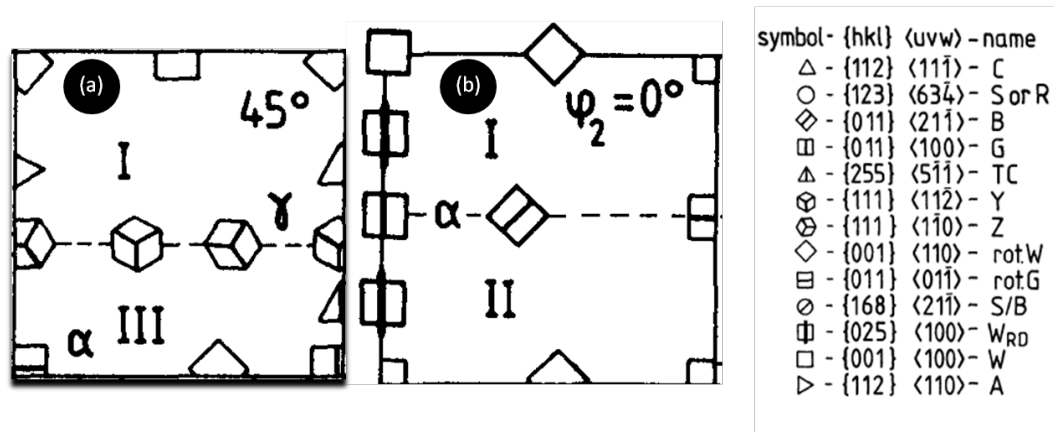


Figure 3.9 Orientation used for texture description in cubic materials plotted in (a) $\Phi_2=45^\circ$ and (b) $\Phi_2=0^\circ$ sections of the Euler space[66].

Fig. 3.10a shows the IPF-X (RD: Rolling Direction) map and Fig. 3.10(b) shows the $\Phi_2=45^\circ$ section of the ODF plot obtained from the extruded and annealed (1100 °C for

1h) 18Cr ODS bar sample. Complete alpha fibre texture was present with orientation from $\{001\} \langle 110 \rangle$ to $\{011\} \langle 01\bar{1} \rangle$. The Euler X (RD) map with the IPF color code shows the dominant orientation of $\langle 110 \rangle \parallel \text{RD}$ representing alpha fibre texture. Almost uniform strength (~ 6.5 times random) of all the components in the alpha fibre was found. But, only $\{111\} \langle 1\bar{1}0 \rangle$ component of gamma fibre was also present which was of similar strength (6.9 times random).

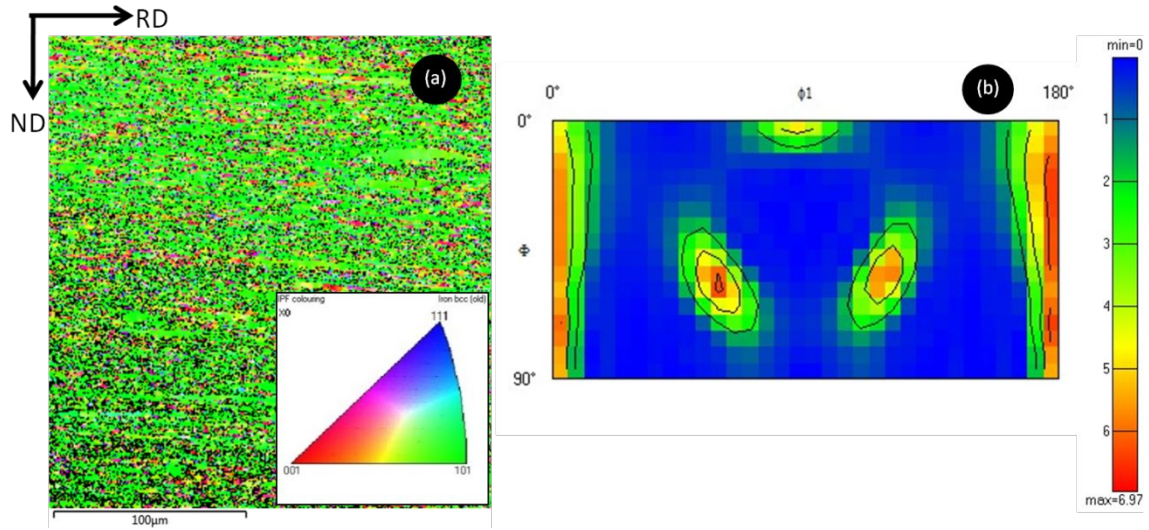


Figure 3.10 (a) Euler-X map with IPF legend in inset and (b) $\Phi_2=45^\circ$ section of the ODF in the extruded and annealed (1100 °C for 1h) 18Cr ODS bar sample.

After rolling by 30%, the complete alpha fibre was obtained but became weaker (maximum 4 times random) as can be seen from Fig. 3.11(a). Complete gamma fibre was also developed but of less strength (max 4 times random). After 40% cold work, complete alpha fibre was found but the components with orientation $\{001\} \langle 110 \rangle$ to $\{112\} \langle 110 \rangle$ became preferentially stronger 13 times random as compared to the rest of the components (6 times random) as it is clear from the ODF profile (Fig. 3.11(b)). Gamma fibre component $\{111\} \langle 1\bar{1}0 \rangle$ only was observed which was 5 times random. Figure 3.11(c) shows the $\Phi_2=45^\circ$ section of 50% CW 18Cr ODS sample. Partial alpha fibre from $\{001\} \langle 110 \rangle$ to $\{111\} \langle 1\bar{1}0 \rangle$ was 5 times random. Full gamma fibre was formed with strong component $\{111\} \langle 11\bar{2} \rangle$ (9 times random).

The 30% CW sample was annealed at 1050 °C and the partial alpha fibre $\{001\} \langle 110 \rangle$ to $\{111\} \langle 1\bar{1}0 \rangle$ with max 6 times randomness was found (Fig. 3.12(a)). The $\{111\} \langle 1\bar{1}0 \rangle$ component of gamma fibre was also present (4 times random). The texture of the 18Cr ODS sample (30% CW and annealed at 1150 °C) shows Goss type texture which was 3 times random as evident from Fig. 3.12(b) (presenting $\Phi_2=0^\circ$ of ODF). Typical

alpha and gamma fibre can no longer be observed. In 30% CW sample annealed at 1250 °C, Brass component of texture was found with 7.6 times randomness (Fig. 3.12(c)). It can be noted that alpha and gamma textures are described through $\Phi_2=45^\circ$ section and Goss/Brass textures are presented through $\Phi_2=0^\circ$ section images of ODF for all the samples.

The texture of 40% CW sample with annealing at 1050 °C can be seen from Fig. 3.13(a). Partial alpha fibre from $\{001\} \langle 110 \rangle$ to $\{111\} \langle 1\bar{1}0 \rangle$ with strong $\{111\} \langle 1\bar{1}0 \rangle$ component (12 times random) was present along with only $\{111\} \langle 1\bar{1}0 \rangle$ component of gamma fibre (12.6 times random). In 40% CW sample after annealed at 1150 °C, no trace of alpha fibre exists but Goss and brass components are found as shown in Fig. 3.13(b). Figure 3.13(c) ODF shows that in 40% CW sample annealed at 1250 °C, textured orientation is in between Goss and Brass type. The maximum intensity of this component is obtained as 6.38 times random.

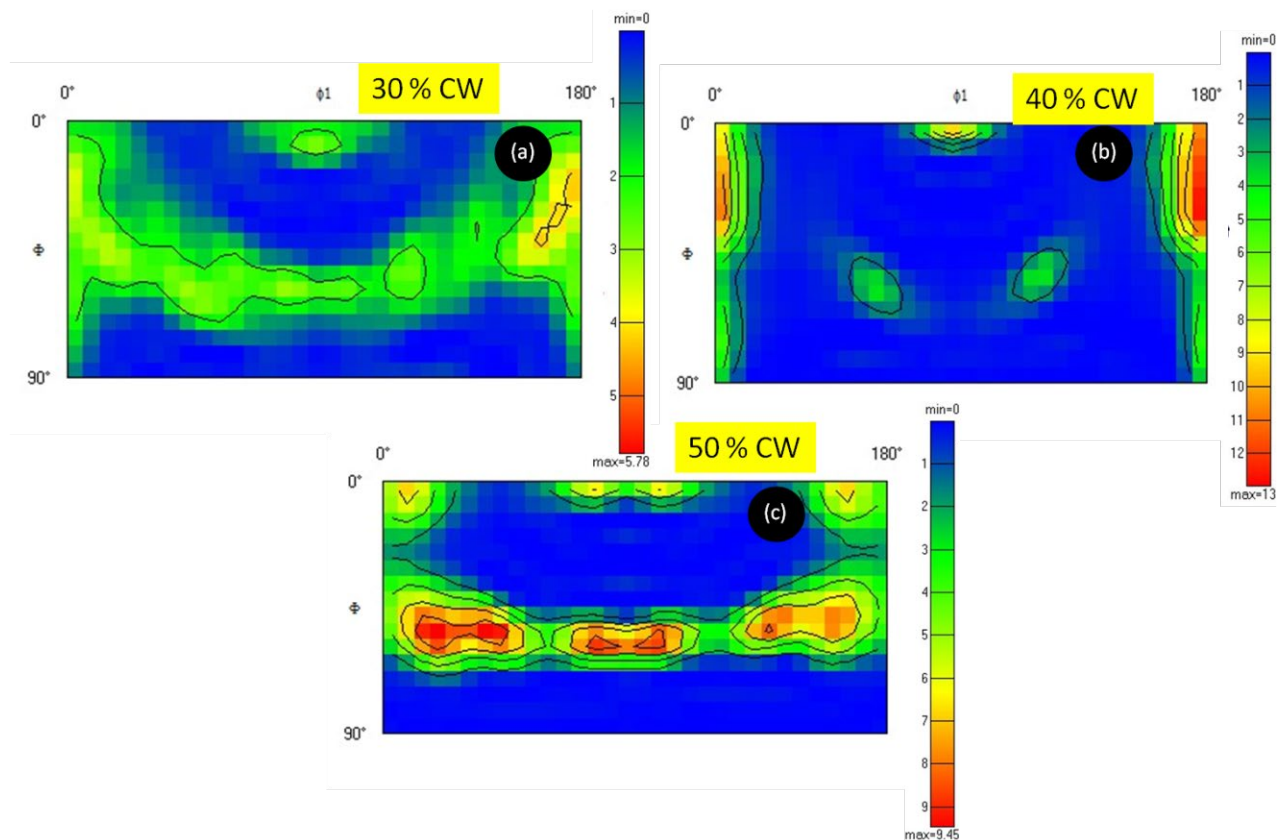


Figure 3.11 $\Phi_2=45^\circ$ section of the ODF after (a)30%, (b)40 % and (c) 50 % CW.

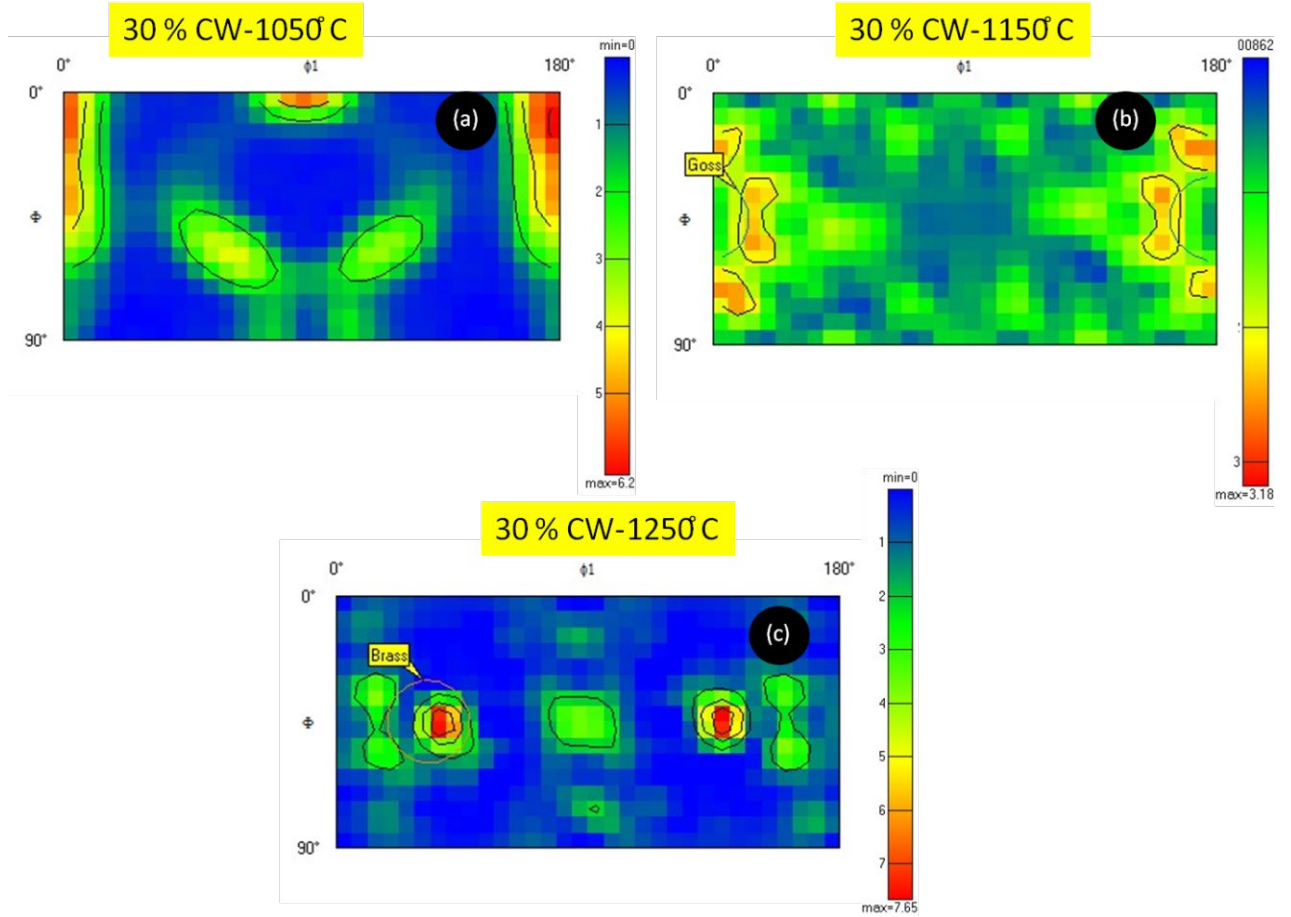


Figure 3.12 ODF in the 30% CW ODS alloy after annealing at (a) 1050 °C - $\Phi_2=45^\circ$ section, (b) 1150 °C - $\Phi_2=0^\circ$ section and (c) 1250 °C - $\Phi_2=0^\circ$ section respectively.

Figure 3.14(a) shows the $\Phi_2=45^\circ$ section of ODF in the 50% CW sample annealed at 1050 °C. Partial alpha fibre from $\{001\} \langle 110 \rangle$ to $\{111\} \langle 1\bar{1}0 \rangle$ was formed. The strong orientation was formed in b/w $\{112\} \langle 110 \rangle$ and $\{111\} \langle 1\bar{1}0 \rangle$ orientation with 10 times randomness. Complete gamma fibre was formed but with strong component $\{111\} \langle 1\bar{1}0 \rangle$ with 7 times randomness. Figure 3.14(b) shows that Goss type texture only forms in the 50% CW sample when annealed at 1150 °C (max. 9.6 times random). 50% CW sample annealed at 1250 °C develops Goss texture with higher intensity (11.4 times random) as can be seen from Fig. 3.14(c).

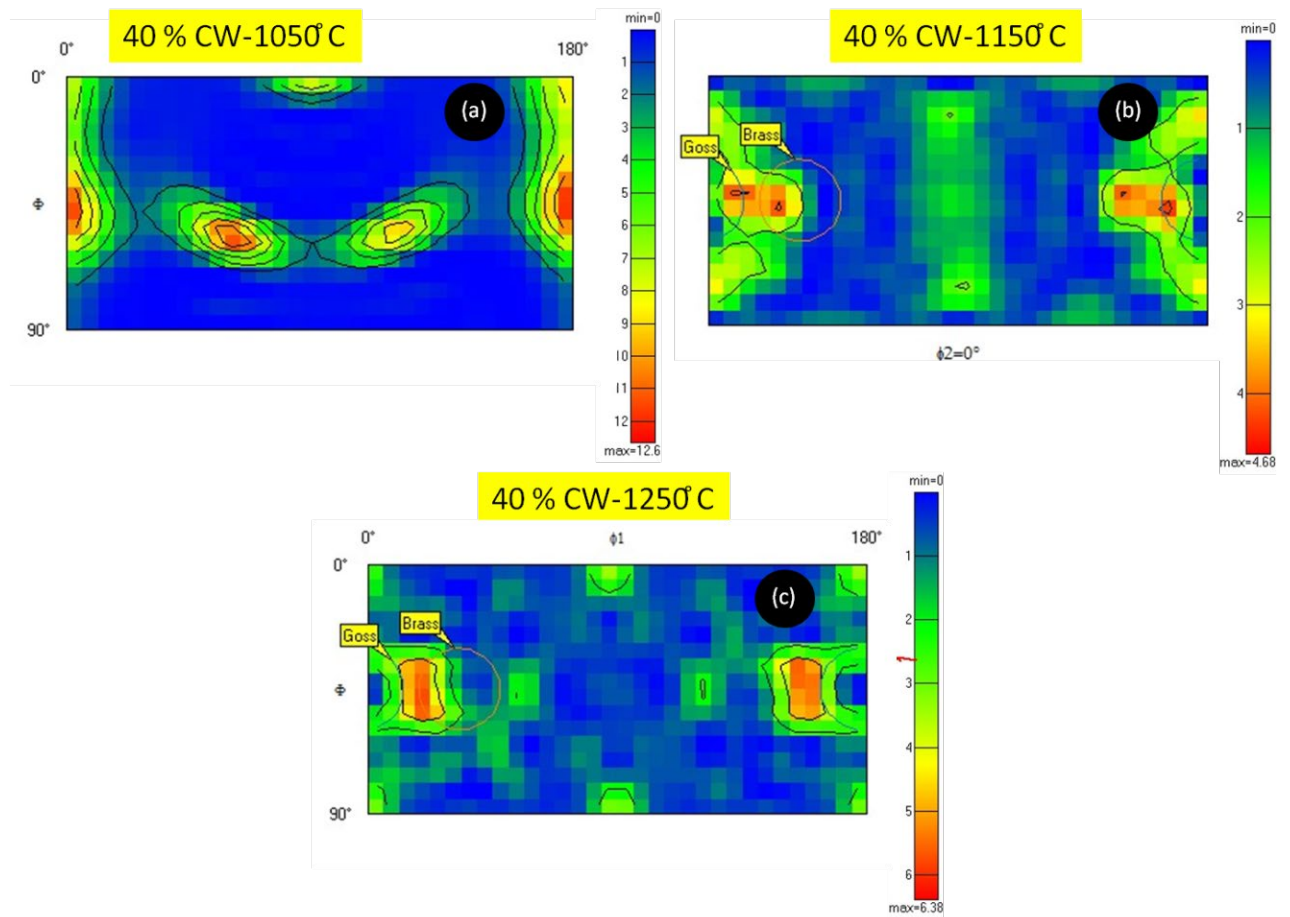


Figure 3.13 ODF in the 40% CW ODS alloy after annealing at (a) 1050 °C - $\Phi_2=45^\circ$ section, (b) 1150 °C - $\Phi_2=0^\circ$ section and (c) 1250 °C - $\Phi_2=0^\circ$ section respectively.

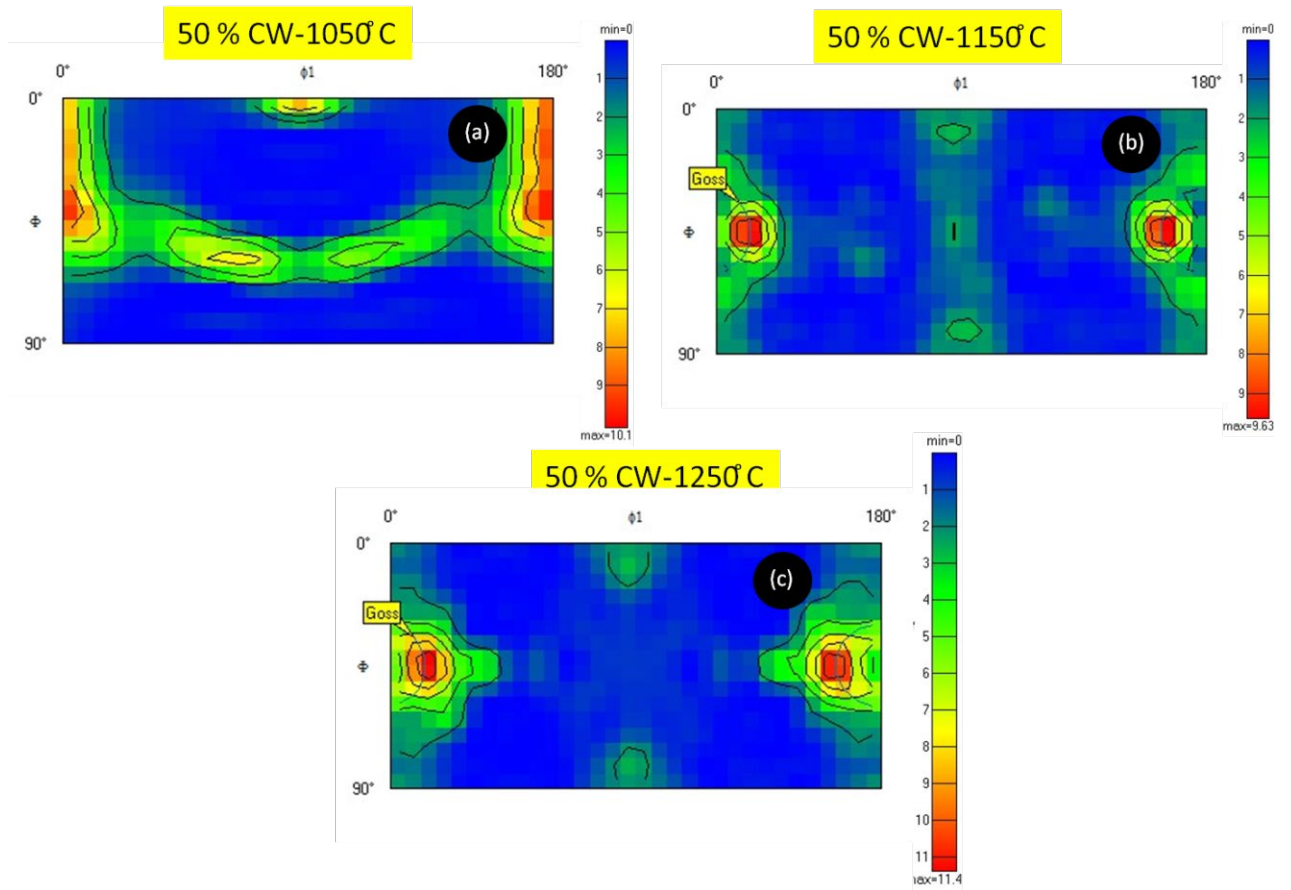


Figure 3.14 ODF in the 50% CW ODS alloy after annealing at (a) 1050 °C - $\Phi_2=45^\circ$ section, (b) 1150 °C - $\Phi_2=0^\circ$ section and (c) 1250 °C - $\Phi_2=0^\circ$ section respectively.

Evolution of texture with cold work and annealing temperature at different stages are presented in Table 3.5.

Table 3.5 Evolution of texture in the 18 Cr ODS samples with 30, 40 and 50 % cold work when annealing is carried out at different temperatures of 1050, 1150 and 1250 °C

Condition	Texture		
	Alpha	Gamma	Others
Extruded & annealed	Full homogenous; (6.9 times random)	Component $\{111\}$ $\langle 1\bar{1}0 \rangle$;(6.9 times random)	
30 % CW	Full; weak (max 4 times random)	Full; weak (max 4 times random)	
40 % CW	Full; but $\{001\}$ $\langle 110 \rangle$ to $\{112\}$ $\langle 110 \rangle$ 13 times random else 6 times random	component $\{111\}$ $\langle 1\bar{1}0 \rangle$;(5 times random)	
50 % CW	$\{001\}$ $\langle 110 \rangle$ & $\{111\}$ $\langle 1\bar{1}0 \rangle$ component 5 times random	Full with strong diverged component $\{111\}$ $\langle 11\bar{2} \rangle$ 9 times random	
30-1050	partial $\{001\}$ $\langle 110 \rangle$ to $\{111\}$ $\langle 1\bar{1}0 \rangle$ maximum 5 times random	$\{111\}$ $\langle 1\bar{1}0 \rangle$;(4 times random)	
30-1150	-	-	Near Goss : $\{011\}$ $\langle 100 \rangle$ ($\varphi_2=0^\circ$ section)
30-1250			Brass: $\{011\}$ $\langle 21\bar{1} \rangle$ ($\varphi_2=0^\circ$ section)
40-1050	partial $\{001\}$ $\langle 110 \rangle$ to $\{111\}$ $\langle 1\bar{1}0 \rangle$ with strong $\{111\}$ $\langle 1\bar{1}0 \rangle$ component 12 times random	$\{111\}$ $\langle 1\bar{1}0 \rangle$;(12 times random)	-
40-1150	-		In b/w Goss : $\{011\}$ $\langle 100 \rangle$ & Brass: $\{011\}$ $\langle 21\bar{1} \rangle$ ($\varphi_2=0^\circ$ section)
40-1250		-	In b/w Goss : $\{011\}$ $\langle 100 \rangle$ & Brass: $\{011\}$ $\langle 21\bar{1} \rangle$ ($\varphi_2=0^\circ$ section)
50-1050	partial $\{001\}$ $\langle 110 \rangle$ to $\{111\}$ $\langle 1\bar{1}0 \rangle$ with strong in b/w $\{112\}$ $\langle 110 \rangle$ and $\{111\}$ $\langle 1\bar{1}0 \rangle$ 10 component times random	Full; strong component $\{111\}$ $\langle 1\bar{1}0 \rangle$ at 7 times random	
50-1150			Near Goss : $\{011\}$ $\langle 100 \rangle$ ($\varphi_2=0^\circ$ section)
50-1250			Near Goss : $\{011\}$ $\langle 100 \rangle$ ($\varphi_2=0^\circ$ section)

3.4. Discussion

3.4.1. Model ODS Alloys

Hardness study on three model ODS alloys (Fe-0.3Y₂O₃, Fe-0.2Ti-0.3Y₂O₃ and Fe-14Cr-0.2Ti-0.3Y₂O₃) revealed that the Cr addition led to much higher hardness as compared to the other two alloys (Table 3.2). OIM imaging (Fig. 3.1 and 3.2) showed that all three alloys were having almost equiaxed grains in both longitudinal and transverse section without any directional anisotropy. Some grains in Fe-Ti ODS appeared bigger than Fe-ODS as can be found in the grain size distribution histograms too (Fig. 3.3). But more number of fine grains in Fe-Ti ODS as compared to Fe-ODS finally yields similar average grain size. For uniform dissolution of Ti, ball milling parameters were optimized [87]. However non uniform distribution could result in change ingrain size distribution[115].

Average grain size was found to be similar in both the Fe-0.3Y₂O₃ and Fe-0.2Ti-0.3Y₂O₃ alloys, but very fine microstructure was observed in the Fe-14Cr-0.2Ti-0.3Y₂O₃ alloy along with finer grain band structure. The higher hardness is due to drastic refinement of grain size. EBSD study of the model ODS alloys showed that the Cr added Fe-14Cr-0.2Ti-0.3Y₂O₃ has finer microstructure (with fine grain bands) as compared to the Fe-0.3Y₂O₃ and Fe-0.2Ti-0.3Y₂O₃ alloy. It could be possible due to higher extrusion temperature or annealing temperature used during Cr-added ODS alloy fabrication which may help in recrystallization as the alloy remains fully ferritic. Though recrystallization fraction increased in this alloy dominant structure was found deformed except the fine grain bands. This drives to suspect that recrystallization alone did not create the fine grain structure, but some other factors in presence of Cr was responsible for fine grain structure which will be discussed in chapter 4 (section 4.3.1).

Typical alpha texture with $\langle 110 \rangle \parallel \text{RD}$ is present in the Fe-0.3Y₂O₃ and Fe-0.2Ti-0.3Y₂O₃ alloy. But texture reduces near to random in case of the Fe-14Cr-0.2Ti-0.3Y₂O₃ alloy. The finer grain bands were found to be recrystallized which could be the cause for removal of texture from the alloy.

3.4.2. 18 Cr-ODS Alloy

Study of recrystallization showed that though the 18Cr ODS extruded rod was annealed at 1100 °C/1 h, dominant deformed structure was still present. Unlike the 14 Cr ODS alloy, this alloy was found with typical elongated bamboo grain structure along the rod longitudinal direction showing directional anisotropy. Homogenous alpha fibre with

strength around 6.9 tr (times random) was present and $\{111\} \langle 1\bar{1}0 \rangle$ component of gamma fibre was present of similar strength.

After 30% cold work on 18Cr ODS steel, microstructure remained elongated and deformed fraction of grains increased (Table 3.4). The texture became weaker but nearly homogenous alpha and gamma fibre was observed. After annealing at 1050 °C, partial alpha fibre from $\{001\} \langle 110 \rangle$ to $\{111\} \langle 1\bar{1}0 \rangle$ similar to cold rolled state was retained with slight increase in strength. Very weak Goss $\{101\} \langle 100 \rangle$ texture is formed after annealing at 1150 °C. Brass texture $\{011\} \langle 21\bar{1} \rangle$ of intensity 7.6 times random is generated when annealed at 1250 °C. Table 3.4 shows that microstructure remained mainly deformed up to annealing at 1050 °C whereas formation of substructure and increase in recrystallized fraction is triggered after annealing at 1150 °C with further increase in annealing temperature at 1250 °C. This indicates that deformed grains have a signature of alpha and gamma texture whereas onset of substructure and recrystallization leads to formation of near Goss or Brass texture. The deformed grains shows typical preference towards alpha and gamma texture component and hence the CW state and deformation dominant, annealed state at 1050 °C consists of alpha and gamma fibre components. At 1150 °C, alpha or gamma oriented grain fraction drastically reduce and Goss grains are found but of weak intensity. At 1250 °C, stronger Brass texture was developed. In order to understand the formation or growth of the Goss grains, misorientation angle between these growing grain and the major texture components of the consumed matrix was calculated as shown in Table 3.6. Misorientation between Goss grains and $\{112\} \langle 110 \rangle$ and $\{111\} \langle 1\bar{1}0 \rangle$ deformed grain components is 45.99 ° around random axis. This marginally satisfies the criteria for high energy boundaries with high mobility with misorientation in the range of 15 ° to 45 ° [116,117]. The Brass orientation has a perfect high energy misorientation of 30 and 35.6 ° with $\{112\} \langle 110 \rangle$ and $\{111\} \langle 1\bar{1}0 \rangle$ deformed grains. Misorientation of 46 ° between matrix- $\{001\} \langle 110 \rangle$ to Brass grains may be considered as high mobility considering the deviation from ideal orientation in the practical ODS steel [118]. The transformation from matrix- $\{001\} \langle 110 \rangle$ to Goss is not backed by any high energy assistance as misorientation is quite high 62.8 °. But it is quite possible that matrix- $\{001\} \langle 110 \rangle$ transformed to Brass grains at 1150 °C which were of much lesser intensity may be due to small quantity or size.

Table 3.6 Misorientation between nucleus at higher temperature and deformed grain of 30 % CW 18Cr ODS sample

Deformed matrix Nucleus/ growing grain	{001} <110>	{112} <110>	{111} < $\bar{1}\bar{1}0$ >
{011} <21 $\bar{1}$ > (Brass)	46 ° @ [2 $\bar{2}$ 4 $\bar{5}$]	30 ° @ [11 $\bar{1}$]	35.6 ° @ [16 1 $\bar{1}\bar{2}$]
{011} <100> (Goss)	62.8 ° @ [5 12 12]	45.99 ° @ [117 $\bar{1}0$ 24]	45.99 ° @ [117 $\bar{1}0$ 24]

The {001} <110> and {112} <110> alpha fibre components of 40% cold worked sample transformed into strong {111} < $\bar{1}\bar{1}0$ > component with {001} <110> retained after annealing at 1050 °C. The strength of the {001} <110> component before and after annealing remained same. This suggests that this component did not transform into {111} < $\bar{1}\bar{1}0$ >. This is supported by the fact that this boundary has 54.74 ° misorientation which is not a high mobility thus inhibiting the transformation. On the other hand misorientation of 19.47 ° transformed the matrix-{112} <110> into energetically favored {111} < $\bar{1}\bar{1}0$ >. The misorientation values at 1050°C are tabulated in Table 3.7. The Annealing at 1150 °C and 1250 °C led to formation of near Goss/Brass texture. Table 3.8 shows the misorientation values found for texture transformation at 1150 and 1250 °C. As discussed earlier, this might have been possible with matrix-{001} <110> transformation into Brass grains via favorable misorientation of 46 ° or into Goss grains overcoming 62.8° misorientation assisted by more stored energy from increased amount cold work and higher temperature.

Table 3.7 Misorientation between nucleus at 1050°C and deformed grain of 40 % CW sample

Deformed matrix Nucleus/ growing grain	{001} <110>	{112} <110>
{111} < $\bar{1}\bar{1}0$ >	54.74 ° @ [$\bar{1}$ $\bar{1}0$]	19.47 ° @ [0 $\bar{1}$ 1]

Table 3.8 Misorientation between nucleus at higher temperature and deformed grain of 40 % CW sample

Deformed matrix Nucleus/ growing grain	{001} <110>	{112} <110>
{011} <21 $\bar{1}$ > (Brass)	46 ° @ [2 $\bar{2}$ 4 $\bar{5}$]	30 ° @ [1 1 $\bar{1}$]
{011} <100> (Goss)	62.8 @ [5 12 12]	45.99 ° @ [117 $\bar{1}0$ 24]

50% cold work led to formation of $\{001\} \langle 110 \rangle$ and $\{111\} \langle \bar{1}\bar{1}0 \rangle$ component of alpha fibre and gamma fibre with strong $\{111\} \langle 11\bar{2} \rangle$ component. At 1050 °C, partial alpha from $\{001\} \langle 110 \rangle$ to $\{111\} \langle \bar{1}\bar{1}0 \rangle$ was developed with maximum in between $\{112\} \langle 110 \rangle$ and $\{111\} \langle \bar{1}\bar{1}0 \rangle$ via high mobility boundaries with misorientation values as tabulated in Table 3.9. Annealing at 1150 °C and 1250 °C transformed the texture to strong near-Goss orientation with much higher intensity (Table 3.10).

Table 3.9 Misorientation between nucleus at 1050°C and deformed grain of 50 % CW sample

Deformed matrix Nucleus/ growing grain	$\{111\} \langle 11\bar{2} \rangle$
$\{111\} \langle \bar{1}\bar{1}0 \rangle$	30 ° @ $[1\ 1\bar{1}]$
$\{112\} \langle 110 \rangle$	35.64 ° @ $[66\ 88\ \bar{5}]$

Table 3.10 Misorientation between nucleus at higher temperature and deformed grain of 50 % CW sample

Deformed matrix Nucleus/ growing grain	$\{001\} \langle 110 \rangle$	$\{111\} \langle \bar{1}\bar{1}0 \rangle$	$\{111\} \langle 11\bar{2} \rangle$
$\{011\} \langle 100 \rangle$ (Goss)	62.8 ° @ $[5\ 12\ 12]$	45.99 ° @ $[117\ \bar{1}0\ 24]$	35.26 ° @ $[\bar{1}\ 1\ 0]$

Leng *et al.* [118] studied recrystallization texture of 88% cold worked 15Cr ODS ferritic steel. The authors found that annealing at 1000 °C produces strong $\{110\} \langle 112 \rangle$ texture i.e. Brass type texture whereas the present study showed formation of $\{110\} \langle 112 \rangle$ texture in the 30% CW sample only after annealing at higher temperature 1250 °C. This difference in annealing temperature required to produce similar texture may be because of the comparatively very high amount of cold work imparted in Leng *et al.*'s study [118]. The authors observed that annealing at 1150 °C and 1300 °C produces strong $\{111\} \langle 112 \rangle$ type gamma component texture but present study showed formation of the Brass/Goss type texture from annealing temperature 1150 °C. The difference in texture formation in the 18Cr ODS (in the present work) as compared to that in the 15Cr ODS of reference [118] can be because of the following reason:

Different amount of cold work imparted on the 18Cr ODS and 15Cr ODS alloys. Based on published data, it is widely accepted that the stored energy (E_d) of the deformed matrix

depends on the dominant plane of the deformed matrix and $Ed_{(111)} > Ed_{(112)} > Ed_{(001)}$ [119,120]. 88% cold work in the 15Cr ODS alloy produced deformed grain with $\{001\} \langle 110 \rangle$ as the highest texture intensity with minimum stored energy (Ed). But in all the 18Cr ODS alloys in CW condition, deformed matrix had either similar or dominating contribution from other planes as well like (111) and (112) with greater amount of stored energy.

3.5. Conclusions

EBS D study of the model ODS alloys showed that the Cr added Fe-14Cr-0.2Ti-0.3Y₂O₃ has finer microstructure (with fine grain bands) as compared to the Fe-0.3Y₂O₃ and Fe-0.2Ti-0.3Y₂O₃ alloy. Though recrystallization fraction increased in this alloy dominant structure was found deformed except the fine grain bands. This indicated that not only recrystallization but some other factor in presence of Cr was responsible for fine grain structure in the alloy. Typical alpha texture with $\langle 110 \rangle \parallel \text{RD}$ is present in the Fe-0.3Y₂O₃ and Fe-0.2Ti-0.3Y₂O₃ alloy. But texture reduces near to random in case of the Fe-14Cr-0.2Ti-0.3Y₂O₃ alloy. The finer grain bands were found to be recrystallized which could be the cause for removal of texture from the alloy.

Temperature plays a crucial role in deciding the texture of the 18 Cr ODS alloy. Deformed structure was found to develop alpha and gamma fibre texture with excitation of different components depending on amount of cold work. A shift in microstructure from deformed towards substructure or recrystallized form was noticed from annealing at 1150 °C onwards. With increase in recrystallization, the texture also transformed from alpha/gamma fibre to near Goss/Brass orientation. Minimum texture was obtained in 30 % CW sample when annealed at 1150 °C. The mechanism of the texture transformation is aided by high energy boundaries with high mobility associated with a misorientation range of 15-45 °.

Chapter 4

Role of Cr and Ti in oxide particle dispersion, crystal structure and composition of ODS Alloys

4.1. Introduction

In order to make Generation IV and fusion reactors a reality, a superior core design is absolutely necessary with a high performance advanced cladding technology. Oxide dispersion strengthened (ODS) steels are the most intended primary candidate material for such application because of its remarkable irradiation resistance at high temperature. The exceptionally higher creep strength and excellent radiation response of ODS steel as compared to the conventional ferritic/martensitic steels can be attributed to the large number of nanoscale oxide particles dispersed in to the steel matrix [121–123]. These stable oxide dispersoids effectively impede dislocation motion, arrest grain growth and trap radiation-induced point defects [20,124–127].

Synthesis of these alloys involves mechanical alloying (MA) with the aid of a high energy ball mill. MA blends powders of required composition and mills it through repeated flattening and fracturing process [128,129]. Subsequently the mechanically alloyed powders are subjected to hot-extrusion [130] or hot-isostatic pressing [131] for consolidation. During this consolidation process, Y–Ti oxide nanoclusters form [20,132,133]. In order to probe the effect of alloying element on nano particle size distribution, and composition, ODS alloys of varying composition has been synthesized and studied [20,131–136].

Further, many theoretical studies are also carried out to examine the effect of different alloying elements on oxide particle formation. Murali et al. [77] probed clustering behavior of Ti, Y and O in bcc Fe in presence of Cr by ab initio calculations. The report revealed that the Cr shows weak interaction with vacancies and repulsive interactions with Y and Ti [77]. In addition, structure of nanoclusters was found with a Cr rich shell formed around Y, O, Ti enriched core.

Even though a number of experiments have been carried out in order to understand the oxide particle evolution and their crystal structure, the effect of the alloying elements in the formation of the oxide particles and deciding their crystal structure is not yet well established. Through experimental evidence, it is commonly accepted that Ti stabilizes the ultrafine clusters and makes the particle dispersion finer [78]. But only a very few reports

exist that focuses on studying the role of Cr in size distribution and crystal structure of oxide nano particles.

The objective of the present work was to examine the exclusive role of the individual alloying elements like Cr and Ti in the oxide particle formation, dispersion, and crystal structure. Alloys with three different compositions were selected in the present study Fe–0.3 Y₂O₃, Fe–0.2Ti– 0.3 Y₂O₃ and Fe–14Cr–0.2Ti–0.3 Y₂O₃ (all in wt %). From earlier work [137], excellent creep strength was obtained when 0.35 wt% Y₂O₃ was added in the alloys. Based on this, Fe–0.3Y₂O₃ alloy was chosen in the present study. This alloy also serves as a simple platform to study the structure and chemistry of Y₂O₃ particles in the Fe (bcc) matrix. It is well known that in presence of Ti, particle dispersion becomes finer with small Y–Ti–O clusters [78]. Increase in Ti concentration further reduces particle size and inter-particle distance which explains measured increase in creep strength [78]. The second alloy system was selected as Fe–0.2Ti–0.3 Y₂O₃ to examine the effect of Ti. Cr has a significant role in improving corrosion resistance and it acts as bcc ferrite (matrix) stabilizer. But limited study has been executed to understand the effect of Cr on oxide particle crystal structure and size distribution. Therefore, in the third system, Cr was added generating Fe–14Cr–0.2Ti–0.3Y₂O₃ alloy to study its influence on crystal structure, dispersion and microstructure.

4.2. Experimental

The model ODS alloys were synthesized through mechanical alloying and hot extrusion method. High purity elemental powders of Fe, Cr, Ti and Y₂O₃ were weighed and mixed to obtain the alloy precursors of selected compositions of Fe-0.3Y₂O₃, Fe-0.2Ti-0.3Y₂O₃ and Fe-14Cr-0.2Ti-0.3Y₂O₃. The Y₂O₃ powder (Alfa Aesar) with an average particle diameter of ~ 22 nm was taken for ball milling and the crystal structure of the Y₂O₃ was body centered cubic (bcc). Mechanical alloying was carried out in argon atmosphere for four hour at 1000 rpm using Simolayer CM-08 for ball milling (ball: powder = 10:1). Two mechanically alloyed powders with the composition of Fe-0.3Y₂O₃ and Fe-0.2Ti-0.3Y₂O₃ were extruded at 1050 °C followed by annealing at 950 °C for two hours and then air cooled. The mechanically alloyed powder of composition of Fe-14Cr-0.2Ti- 0.3Y₂O₃ was extruded at 1150 °C and was subjected to annealing at 1050 °C for 0.5h followed by tempering at 750 °C for two hours and air cooling in order to obtain a well defined microstructure. Finally 12 mm diameter consolidated rods of three different model ODS alloys of composition Fe-0.3Y₂O₃, Fe-0.2Ti-0.3Y₂O₃ and Fe-14Cr-0.2Ti-

0.3Y₂O₃ were obtained. The compositions of the alloys are Fe-0.3Y₂O₃, Fe- 0.2Ti-0.3Y₂O₃ and Fe-14Cr- 0.2Ti-0.3Y₂O₃ respectively as detailed in Table 4.1. In order to study the microstructure and dispersion of the oxide particles, TEM investigation was carried out. The TEM specimens were prepared from three different alloys by slicing disks of thickness ~ 300 µm from the extruded rods, mechanical polishing was carried out up to a thickness of ~ 50 µm. Disks of diameter 3mm were obtained using a disc punch machine from the 50 µm foils. The disks were electropolished up to perforation using a solution of ethanol, 2-butoxy ethanol and perchloric acid (7:2:1 volume ratio) at ~ -35 °C temperature applying a voltage of 22 V. The samples were characterized using LIBRA 200FE (Carl Zeiss) high resolution TEM operated at 200 kV. Energy dispersive X-ray spectroscopy (EDS) analysis, scanning transmission electron microscopy (STEM) and in-column energy filters were attached with the instrument (TEM). The information limit of the microscope is 0.13 nm.

Table 4.1 Alloy compositions with measurements of the bulk oxygen, carbon and nitrogen content of the three alloys in weight percent using ICPMS.

Alloy	Ti	Cr	Y ₂ O ₃	O (%)	C (%)	N (%)	Fe
Fe-0.3Y ₂ O ₃	-	-	0.3	0.46	0.03	0.019	Balance
Fe-0.2Ti-0.3Y ₂ O ₃	0.2	-	0.3	0.47	0.02	0.009	Balance
Fe-14Cr-0.2Ti-0.3Y ₂ O ₃	0.2	14	0.3	0.38	0.02	0.006	Balance

4.3. Results

4.3.1. Effect of alloying element in particle size distribution

Figure 4.1(a) shows a low magnification TEM bright field image of the alloy Fe-0.3Y₂O₃. Oxide nano particles of size 5 to 34 nm are observed in dark contrast. Several low magnification images were acquired in TEM and particle size distribution was examined and the histogram of particle size distribution was plotted (Fig. 4.1 (b)). The average particle size was found to be 11 nm. Figure 4.1 (c) shows a low magnification TEM bright field image of the alloy Fe-0.2Ti-0.3Y₂O₃. Oxide nano particles of various sizes (3 to 33 nm) are observed in dark contrast. The oxide nano particle size distribution was measured from several low magnification images and the histogram of particle size distribution was plotted (Fig. 4.1(d)). The average particle size was found to be 8 nm. Figure 4.1 (e) shows a low magnification TEM bright field image of the alloy Fe-14Cr-0.2Ti-0.3Y₂O₃. Oxide

nano particles of various sizes (1 to 37 nm) are observed in dark contrast. The oxide nano particle size distribution was measured and the histogram of particle size distribution is shown in Fig. 4.1 (f). The average particle size was found to be 4 nm.

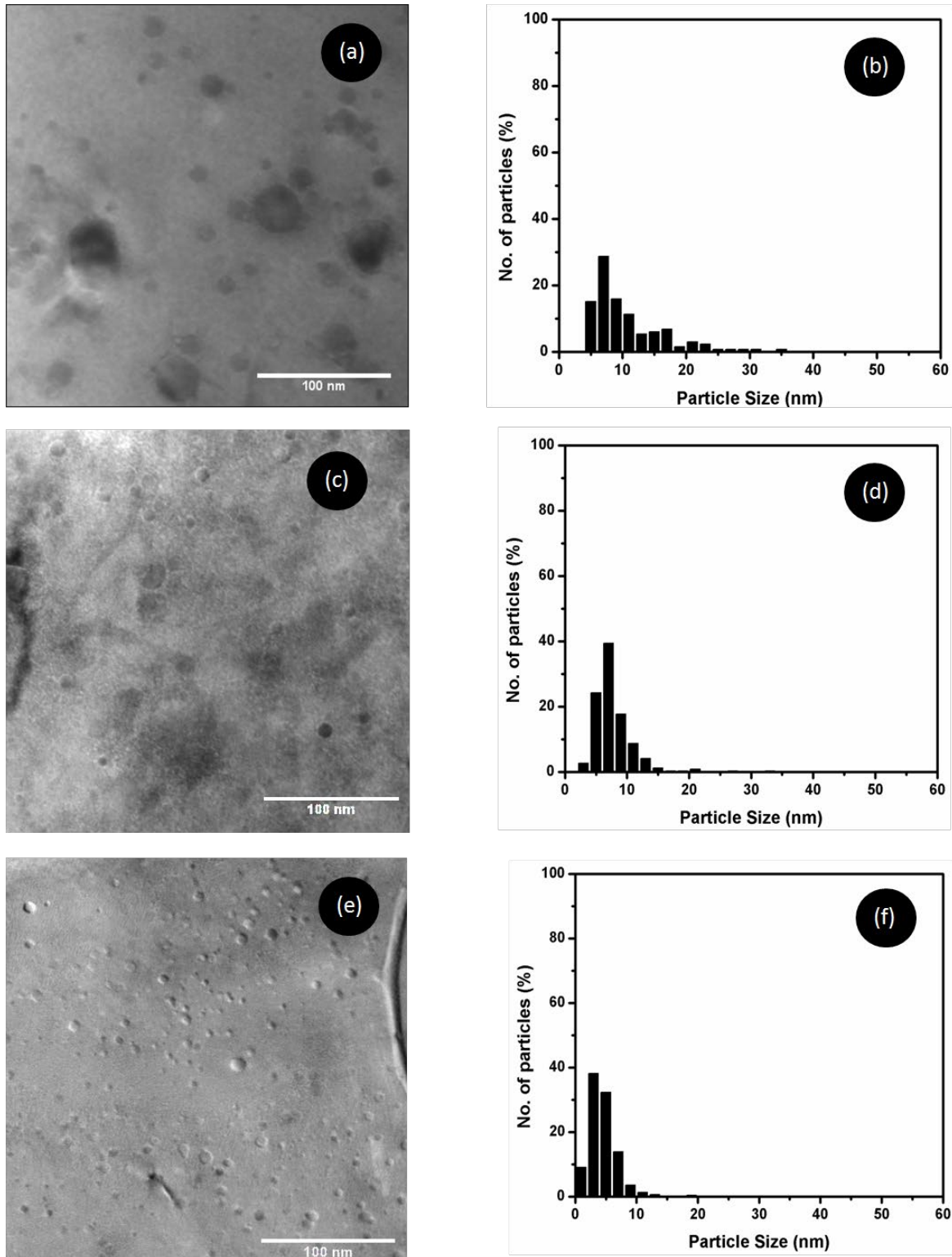


Figure 4.1 BF- TEM images and particle size distribution histogram of alloy (a), (b) Fe-0.3Y₂O₃; (c), (d) Fe-0.2Ti-0.3Y₂O₃ and (e), (f) Fe-14Cr-0.2Ti-0.3Y₂O₃ respectively. The average particle size was 11 nm, 8 nm and 4 nm respectively for Fe-0.3Y₂O₃, Fe-0.2Ti-0.3Y₂O₃ and Fe-14Cr-0.2Ti-0.3Y₂O₃ respectively.

The Number density of the oxide nano particles was calculated from the bright field TEM images considering sample thickness as 60 nm. The obtained particle number

density is tabulated in Table 4.2. A slight increase in particle number density is observed in the Fe-0.2Ti-0.3Y₂O₃ alloy as compared to that in Fe-0.3Y₂O₃ alloy. This further increased by an order of magnitude in case of the Fe-14Cr-0.2Ti-0.3Y₂O₃ alloy.

Table 4.2 Number density and average size of the particle in three ODS alloys

Particle density	Fe-0.3Y ₂ O ₃	Fe-0.2Ti-0.3Y ₂ O ₃	Fe-14Cr-0.2Ti-0.3Y ₂ O ₃
N (m ⁻³)	3.4×10 ²¹	4.3×10 ²¹	4.3×10 ²²

4.3.2. Effect of alloying element in crystal structure of oxide nano particles

High-resolution transmission electron microscopy was carried out on selected oxide particles for studying the particle crystal structure. At least two different *d* spacing values (corresponding to two different *hkl* planes) and the intermediate angle hold between these planes is necessary to identify the crystal structural consistency as some of the in inter-planar *d* spacing values are similar for the possible Y-Ti-O crystal structures. Fast Fourier transforms (FFT) of the lattice images of oxide particles were indexed for obtaining the crystallographic information. Zone axis orientation was identified after matching with structural data from several possible compounds. These included monoclinic and bcc Y₂O₃ or Fe₂O₃ in the Fe-Y₂O₃ alloy, adding TiO₂, Y₂TiO₅, Y₂Ti₂O₇ and YTiO₃ for the alloy with Ti, and for the Fe-14Cr-Ti-Y₂O₃ alloy Cr₂O₃, Cr₂TiO₃ and Cr₂TiO₅. The effect of alloying element like Ti & Cr in the particle composition and crystal structure was studied.

Figure 4.2(a) shows a typical HRTEM image of one spherical oxide nano particle of diameter ~ 15 nm in Fe-0.3Y₂O₃ alloy. The FFT obtained from the highlighted region of Figure 4.2(a) and its corresponding IFFT is presented in Fig. 4.2(b) and (c) respectively. The *d* spacing values were obtained from the enhanced IFFT image and the corresponding spots from the respective (*hkl*) planes were indexed after matching with the interplanar angles as can be seen from Fig. 4.2(b). Three different sets of planes were identified and the interplanar angles were measured using ImageJ software. Two of these *d* spacings were found to be 2.9 Å which is consistent with the {222} type planes of bcc Y₂O₃. The third plane had a *d* spacing of 2.7 Å consistent with {400} planes of bcc Y₂O₃ as given in JCPDS file (41-1105). The zone axis was found to be <011> of the same structure. The particle crystal structure was consistent with bcc Y₂O₃. Two more particles were found structurally consistent with bcc Y₂O₃ and one was found consistent with monoclinic Y₂O₃ structure.

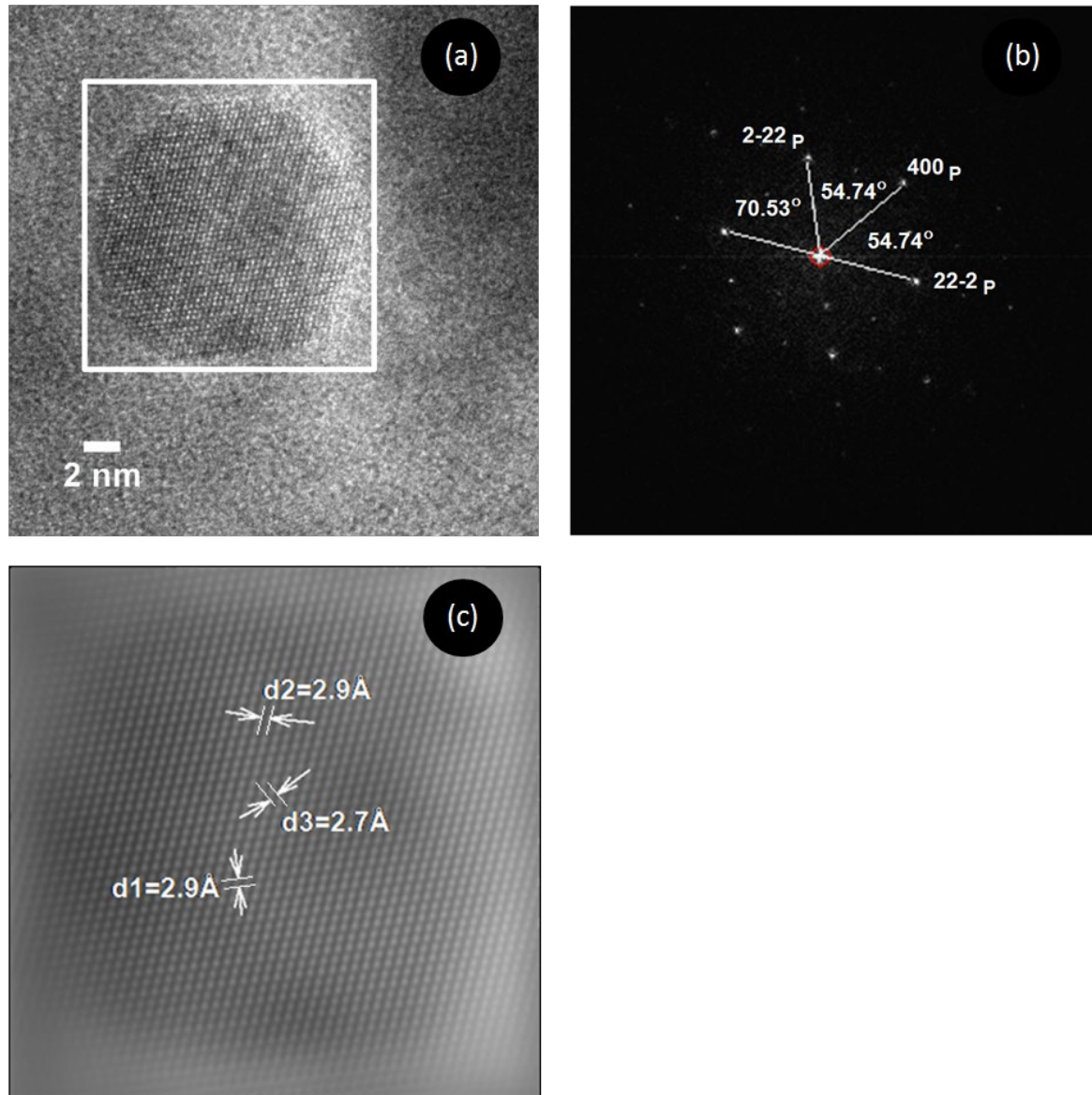


Figure 4.2 (a) HRTEM image from $\text{Fe-0.3Y}_2\text{O}_3$ with an embedded oxide particle; (b) the FFT taken from the highlighted region and with various planes and angles indexed as bcc Y_2O_3 , (c) IFFT.

Figure 4.3(a) shows HRTEM image of one fine oxide nano particle in $\text{Fe-0.2Ti-0.3Y}_2\text{O}_3$ alloy. The FFT obtained from the highlighted region of Fig. 4.3(a) and its corresponding IFFT is presented in Fig. 4.3(b) and (c) respectively. The d spacing values were obtained from the enhanced IFFT image and the corresponding spots from the respective (hkl) planes were indexed after matching with the interplanar angle as can be seen from Fig. 4.3(b). Two sets of planes were identified with d spacing value of 3.0 \AA with an intermediate angle of 70° . These matched well with $\{222\}$ planes of fcc $\text{Y}_2\text{Ti}_2\text{O}_7$. The 3rd plane was found with a d spacing of 2.6 \AA which matched well with $\{400\}$ planes of the same structure. The particle crystal structure was consistent with fcc $\text{Y}_2\text{Ti}_2\text{O}_7$.

The 3rd plane was at an angle of 55.1 ° and 54.1 ° with 1st and 2nd set of planes respectively. The measured values matched with JCPDS file (42-0413) confirming the particle crystal structure consistency with fcc $Y_2Ti_2O_7$.

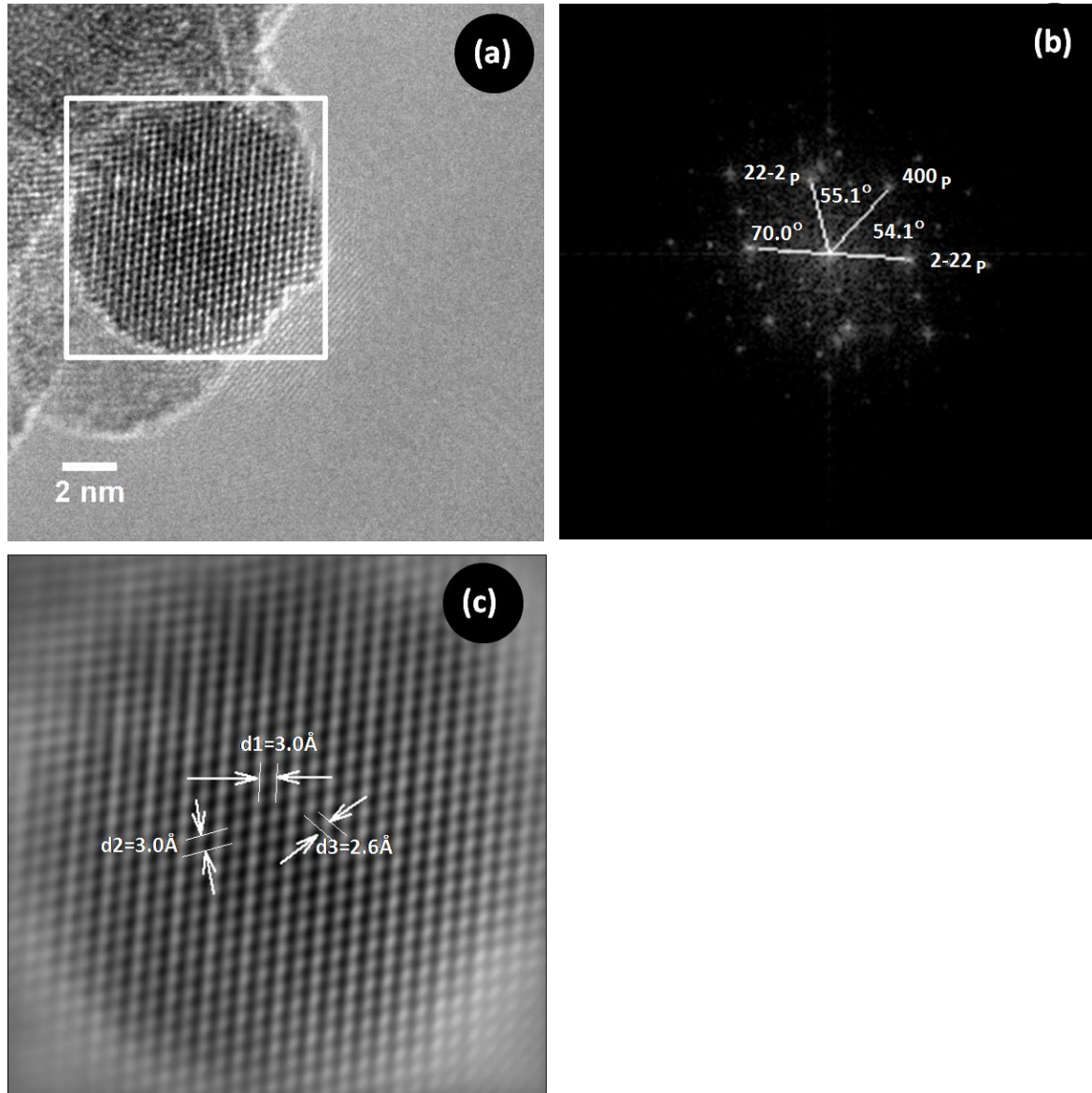


Figure 4.3 (a) HRTEM image from $Fe-0.2Ti-0.3Y_2O_3$ with an embedded particle, (b) the FFT taken from the highlighted region indexed as fcc $Y_2Ti_2O_7$; (c) IFFT.

Figure 4.4(a) shows HRTEM image of another fine oxide nano particle of diameter ~ 7 nm in $Fe-14Cr-0.2Ti-0.3Y_2O_3$ alloy. The FFT obtained from the highlighted region of Fig. 4.4(a) and its corresponding IFFT is presented in Fig. 4.4(b) and (c) respectively. The d spacing values were obtained from the enhanced IFFT image as 2.5 Å and 2.8 Å and the corresponding spots from the respective (hkl) planes were indexed as {140} and {201} after matching with the interplanar angle of 81.25 ° as can be seen from Fig. 4.4(b).

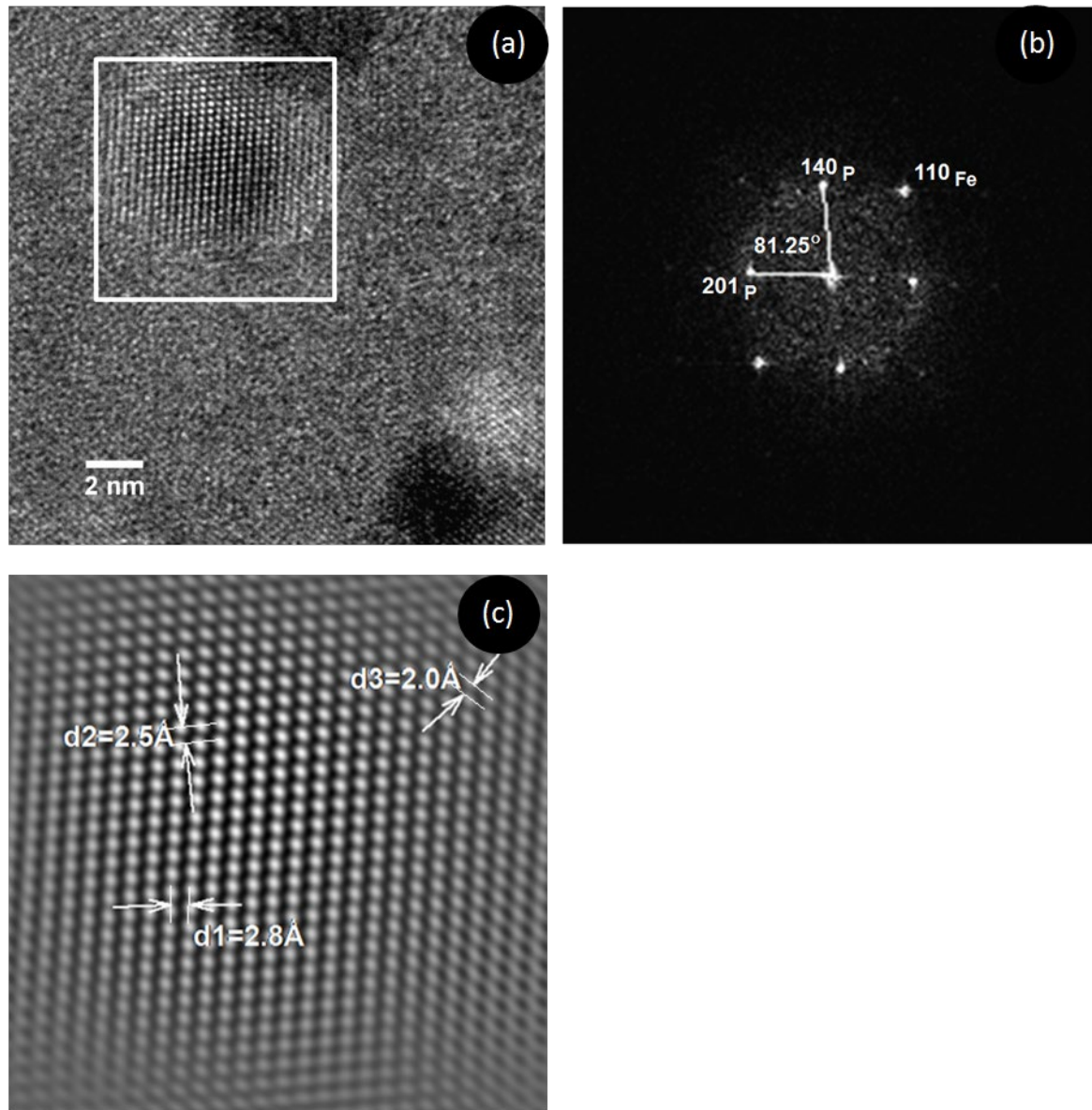


Figure 4.4 (a) HRTEM image from Fe–14Cr–0.2Ti–0.3Y₂O₃ with an embedded particle of size 8 nm; (b) the FFT taken from the highlighted region indexed as orthorhombic Y₂TiO₅ and (c) IFFT.

The particle crystal structure was consistent with orthorhombic Y₂TiO₅ (JCPDS file 40-0795). The consistency obtained between measured d spacing and the interplanar angles with actual d spacing and the interplanar angles from relevant JCPDS card for all the images are tabulated in Table 4.3.

HRTEM of several particles were studied for all three alloys. As expected, the oxide particles in the Fe-0.3Y₂O₃ alloy were mostly bcc Y₂O₃ type only. But the crystal structure of one particle was identified as monoclinic Y₂O₃. In the Fe-0.2Ti-0.3Y₂O₃ alloy, complex oxides were found. The crystal structures of these particles were consistent with either

orthorhombic Y_2TiO_5 or fcc $\text{Y}_2\text{Ti}_2\text{O}_7$. In the Fe-14Cr-0.2Ti-0.3Y₂O₃ alloy too, complex oxides of crystal structure orthorhombic Y_2TiO_5 or fcc $\text{Y}_2\text{Ti}_2\text{O}_7$ was identified. The results are detailed in Table 4.4.

Table 4.3 Crystal structural consistency through comparison between measured and standard structure d spacing and interplanar angles

Figure No.	$d(\text{\AA}), \alpha$	d_1	d_2	d_3	α_{12}	α_{23}	α_{31}
4.2	Measured	2.9	2.9	2.7	69.5	54.2	55.6
	bcc Y_2O_3 (41-1105)	3.06 {2-22}	3.06 {22-2}	2.65 {400}	70.53	54.74	54.74
4.3	Measured	3.0	3.0	2.6	70.0	55.1	54.1
	fcc $\text{Y}_2\text{Ti}_2\text{O}_7$ (42-0413)	3.02 {2-22}	3.32 {2-22}	2.52 {400}	70.53	54.74	54.74
4.4	Measured	2.8	2.5		81		
	Orthorhombic Y_2TiO_5 (40-0795)	3.00 {201}	2.69 {140}		81.25		

Table 4.4 Summary of HRTEM results from individual particles studied in the three ODS alloys including the size range of particles identified.

Alloy	Total number of particles analyzed	Phase			
		Y_2TiO_5 (orthorhombic)	$\text{Y}_2\text{Ti}_2\text{O}_7$ (fcc)	Y_2O_3 (bcc)	Y_2O_3 (monoclinic)
Fe-0.3Y ₂ O ₃	10	N.A.	N.A.	3 (10–20 nm)	1 (12 nm)
Fe-0.2Ti-0.3Y ₂ O ₃	14	5 (5–13 nm)	3 (6–10 nm)	0	0
Fe-14Cr-0.2Ti-0.3Y ₂ O ₃	28	11 (4–16 nm)	2 (5–15 nm)	0	0

4.4. Discussion

The effect of Ti in refinement of oxide particles is already reported by many authors [51,78,123]. In the present study, upon Ti addition, a reduction in particle size is observed and the average particle size came down to 8 nm from 11 nm in the Fe-0.3Y₂O₃ alloy upon addition of Ti. This shows consistency with the earlier suggestion [133] that during mechanical alloying in presence of Ti, Y₂O₃ gets decomposed and any subsequent

heat treatment triggers the nucleation of fine Y–Ti–O complex oxide particles. The Y–Ti complex oxides with superior thermal stability (as compared to the Y-only oxides) prevents their growth, lowering the ultimate particle size after hot consolidation [138]. There are not many reports on effect of Cr in particle size distribution. In the present study, it is observed that addition of Cr leads to formation of even finer distribution of oxide particles reducing the particle size further to 4 nm.

Murali et al. [77] performed ab initio calculations to understand the possible role of Cr on the Ti, Y and O clustering behavior in bcc Fe. Their calculations shows weak interaction between Cr and vacancies and repulsive interaction between Cr and Y/Ti [77]. This suggests that Cr does not play active role in the Y–Ti–O nanoclusters formation. Cr does not go into the core of the particles but strongly attaches to the oxygen-rich surface of the oxide particles [139]. Table 4.4 shows the frequency of particles found consistent with different crystal structures as was obtained from HRTEM analysis. In the Fe–Y₂O₃ alloy, ten numbers of oxide particles were analyzed using HRTEM image and only one particle of 12 nm diameter was found to match with monoclinic yttria and the rest of them were identified as bcc Y₂O₃. The starting powder in the present study was bcc Y₂O₃ and bulk yttria remains stable in the bcc phase up to 2598 K at atmospheric pressure [140–142]. On the contrary, nano-scale Y₂O₃ particles are stabilized in the monoclinic phase owing to the increasing importance of surface effects [137,140,143]. Chang et al. [144] employed electron microscopy to study phase transformations in nano-scale Y₂O₃ and reported that the critical size required for the monoclinic to cubic transformation is in the range of 8–12 nm. It is thus not surprising that presence of both phases of Y₂O₃ is detected from TEM data. The results obtained from a careful study of detecting the frequency orthorhombic Y₂TiO₅ or fcc Y₂Ti₂O₇ in the Fe–Ti–Y₂O₃ and Fe–14 Cr–Ti–Y₂O₃ alloys are less consistent. The ground state formation energies of these phases have been evaluated to be -36.9 eV per formula unit of Y₂Ti₂O₇ (-3560 kJ mol⁻¹) and -27.7 eV per formula unit of Y₂TiO₅ (-2670 kJ mol⁻¹), respectively [51]. This implies that the formation of Y₂Ti₂O₇ should be thermodynamically favoured over Y₂TiO₅. However in the present study of the Fe–Ti–Y₂O₃ alloy, ~63% of the particles indexed by TEM were orthorhombic Y₂TiO₅ and this number increases to ~85% in the Fe–14Cr–Ti–Y₂O₃ alloy. This suggests that although Cr does not interfere with particle core chemistry, presence of Cr favors the formation of the orthorhombic Y₂TiO₅ crystal structure as compared to fcc Y₂Ti₂O₇. However, in the Cr containing alloy crystallographic identification was more difficult because of the smaller average particle diameter which is reflected in the number of particles that could be

indexed from the TEM data as either Y_2TiO_5 or $\text{Y}_2\text{Ti}_2\text{O}_7$ —around 50% of all the particles imaged.

In presence of Ti in the alloy, the particles are detected to be complex oxide type in nature. The analysed particles were structurally consistent with either orthorhombic Y_2TiO_5 or fcc $\text{Y}_2\text{Ti}_2\text{O}_7$. In the Cr added alloy, majority of the particles got detected with Y_2TiO_5 type along with a few consistent with fcc $\text{Y}_2\text{Ti}_2\text{O}_7$. Particles of orthorhombic Y_2TiO_5 type structure were in the size range of 4-16 nm and similar sized particles were also detected with fcc $\text{Y}_2\text{Ti}_2\text{O}_7$ type structure. This shows that there is no specific correlation between composition of a particle with its size.

The drastic reduction in oxide particle size in presence of Cr can be explained from observation by A.J. London et al. [145]. This report shows that the Cr added ODS alloy had oxide particles each one surrounded by a Cr rich shell using APT study. APT data shows that despite the higher consolidation temperature the Cr-containing alloy, smaller oxide particles were detected suggesting that Cr acts to reduce the surface energy of the particles and so reduces the rate of coarsening or promotes nucleation of the clusters. Further, in the alloy without Cr, and in 9Cr ODS alloys, phase transformation to austenite will take place during the hot extrusion (some residual ferrite may be retained) [146]. Kim et al. found an increase in growth rate of the oxide particles upon phase transformation from alpha to gamma iron [147]. Loss of interface (particle-matrix) coherency and enhanced solute diffusion along gamma grain boundaries can explain this observation [148]. Hence, as the alpha–gamma phase transformation of the matrix will be suppressed by 14 wt % of Cr, the particle growth rate may be affected in an indirect way [145].

4.5. Conclusion

TEM study of oxide particle size distribution in model ODS alloys of composition Fe–0.3 Y_2O_3 , Fe–0.2Ti–0.3 Y_2O_3 and Fe–14Cr–0.3Ti–0.3 Y_2O_3 showed that refinement of particle size takes place upon addition of Ti and a further refinement is observed in presence of Cr. In presence of Ti in the alloy, the particles are detected to be complex oxide type in nature. The analysed particles were structurally consistent with either orthorhombic Y_2TiO_5 or fcc $\text{Y}_2\text{Ti}_2\text{O}_7$. In the Cr added alloy, majority of the particles got detected with orthorhombic Y_2TiO_5 type along with a few consistent with fcc $\text{Y}_2\text{Ti}_2\text{O}_7$. Particles of orthorhombic Y_2TiO_5 type structure were in the size range of 4-16 nm and similar sized particles were also detected with fcc $\text{Y}_2\text{Ti}_2\text{O}_7$ type structure. This shows that there is no specific correlation between composition and size of a particle.

Chapter 5

Irradiation response of the nano-particles in Fe-0.2Ti-0.3Y₂O₃ and Fe-14Cr-0.2Ti-0.3Y₂O₃ ODS Alloys

5.1. Introduction

Radiation damage to the structural materials due to intense neutron bombardment is one of the major issues in the development of fast reactors. In order to achieve a high burn up target of about 250 GWd/t in Fast Breeder Reactor (FBR) the core material (clad and wrapper) residence time has to increase substantially. This demands the material to have very good void swelling resistance (due to neutron damage) at higher dose as well as enormous high temperature strength in the range 650-700 °C. In this context, ferritic steel is an indispensable choice since bcc structure is known to be more resistant against irradiation swelling as compared to fcc structure [50]. But, these steels have poor thermal creep strengths at temperatures above 550-600 °C. This restricts the applicability of these steels for clad-tubes operating at temperatures up to 600-700 °C in FBRs.

In order to extend the creep resistance of such ferritic/martensitic steels beyond 650 °C, stable dispersoids can be introduced in the matrix [14,15]. This concept developed the oxide dispersion strengthened ferritic/martensitic steels (ODS steels). Hence, ODS steels have become potential candidate structural material for Generation IV and fusion reactors because of their thriving high-temperature mechanical properties and extraordinary radiation resistance compared to conventional ferritic/martensitic steels [78,149–151]. These properties are derived from stable oxide nano particles which forms during high temperature extrusion after decomposition of yttria in Fe during mechanical alloying [20,77]. This oxide particles act as pinning sites for dislocations, sinks for radiation-induced point defects and also limit the grain growth [70,82,149,152–158]. Variants of ODS alloys are developed by ball milling of differing chemical compositions followed by consolidation techniques forming oxide nano clusters [20,128,129,131–133] which affect the microstructural properties leading to the beneficially resilient properties of these alloys. However, stability of these nano oxide particles under irradiation is an important factor for their long term use.

MA957 is a ferritic commercial ODS alloy with a nominal composition of Fe-14Cr-0.9Ti-0.25Y₂O₃ (in wt %). Irradiation study has been performed in the alloy at 500 °C and 104 dpa produced via neutron bombardment and particles were reported as stable

[79]. Real reactor damage of 200 dpa was also produced in this alloy at 420 °C with the help of nuclear test reactor (FFTF: Fast Flux Test Facility) and no notable change was observed in nano particle density [80]. A neutron dose of 2.5 dpa, 7 dpa and 15 dpa with corresponding irradiation temperature of 400, 330 and 500 °C could neither dissolve nor made them grow [81]. The range of particle sizes changed a little (before irradiation: 1-5 nm; after 75 dpa at 430 °C: 0.5-5 nm) and particle number density changed only slightly in MA957 alloy as per the report given by Ribis et al. [159]. Rogozhkin et al. [160] found through APT (Atom Probe Tomography) study that after a dose of 32 dpa in BOR-60 at 330 °C, particle size remains same but composition changes.

The radiation damage in the materials can also be simulated using ion beam (produced from ion accelerator). Pareige et al. [161] produced Fe ion induced damage from 0.7 dpa in an ODS alloy of composition Fe-12.3Cr-3W-0.39Ti-0.25Y₂O₃ at 300 °C and found particles to remain stable. Nano particles in a high Cr (19%) ODS alloy were also found stable at 10 dpa and 500 °C [162]. Similar stability of particles is also observed at 20 dpa in a Fe-19Cr-1.82W-4Al-0.28Ti-0.29Y-0.368Y₂O₃ alloy through a broad temperature zone of 200-700 °C [163]. ODS steel of composition Fe-16Cr-0.1Ti-0.35Y₂O₃ showed stable particles at 650 °C up to 60 dpa dose [164]. In a Fe-19Cr-2W-4Al-0.3Ti-0.35Y₂O₃ alloy, particles of 7-9 nm diameter were reported as stable after irradiated at 670 °C up to a dose of 150 dpa [165].

Opposite to the earlier cases discussed, instability of particles are also reported by several authors. Particles of diameter 1-2 nm are found to undergo complete dissolution at 100 dpa, -75 °C and at 40 dpa from -43 to 26 °C in a 14Cr ODS alloy [82,83]. Allen et al. [84] conducted a study on 5 MeV Ni ion irradiated 9 Cr ODS steel at 150 dpa with irradiation temperature of 500-700 °C. The authors found that as dose increases, particle size decreases and number density increases for all temperatures [84]. The authors stated that this behavior can have a beneficial impact on matrix strengthening [84]. Lescoat *et al.* [85] studied irradiation response of oxide particles in Fe-18Cr ODS and observed a linear relationship between size of the particles with $t_{irr}^{1/3}$ under ion irradiation at 500 °C up to 75 and 150 dpa where t_{irr} presents the time of irradiation. The authors reported that before irradiation the particle size distribution ranged from 0.5-10 nm with centre ~ 3 nm which shifted to 3.5 and 4.5 nm after irradiated to a dose of 75 and 150 dpa respectively.

Ribis *et al.* [166] irradiated Fe-14Cr-1W-0.3Ti-0.3Y₂O₃ alloy at 500 °C up to 150 dpa using ion beam and irradiated MA957 alloy at 430 °C up to 75 dpa using neutron

beam for comparison study. The authors observed that under ion (6.4×10^{-3} dpa/s) irradiation, particle grows 30 times faster as compared to neutron (1.3×10^{-6} dpa/s) irradiation. The authors found that the average particle size increased to 5.6 nm and 2.5 nm after ion irradiation (1.1 nm prior irradiation) and neutron irradiation (2 nm prior irradiation) respectively.

Wharry et al. [86] summarized several studies on irradiation evolution of oxide nano particles in bcc Fe-Cr based ODS alloys and commented that given the inconsistent experimental conditions, results have been widely variable and inconclusive. Hence, to study the irradiation response of the nano particles in presence of different alloying addition in the matrix, ion irradiation was carried out in the Fe-0.2Ti-0.3Y₂O₃ and Fe-14Cr-0.2Ti-0.3Y₂O₃ alloys up to a surface dose of 40 dpa at 600 and 700 °C and the stability of the oxide particles was studied using high resolution TEM.

5.2. Experimental

Model ODS alloys of two different composition were obtained using mechanical alloying followed by consolidation through hot extrusion process. The raw elemental powders (Cr, Ti and Fe) of high purity were blended with Alfa Aesar make bcc Y₂O₃ powder (22 nm was average particle diameter) in Simolayer CM 08 –high energy ball mill. Ball milling was carried out with a ball to powder ratio of 10:1 at a speed of 1000 rpm for 4 h using argon atmosphere. Optimization of the mechanical alloying parameters were done to demonstrate that optimum dispersion can be achieved with 4 hour milling time [87] and same was followed in the present study.

After mechanical alloying, Fe–0.2Ti–0.3Y₂O₃ alloy powder was subjected to extrusion at 1050 °C. Annealing was carried out at 950 °C for 2 h followed by air cooling [88]. Mechanically alloyed powder of Fe–14Cr–0.2Ti–0.3Y₂O₃ alloy was extruded at 1150 °C. was done at 1050 °C for half an hour with tempering at 750 °C for 2 h and air cooled [87]. The concentration of O, C and N are measured by ICPMS and full composition is given in table 5.1.

Table 5.1 Alloy composition with measurements of the bulk oxygen, carbon and nitrogen content of the three alloys in weight percent using inductively coupled plasma mass spectrometry.

Alloy	Ti	Cr	Y ₂ O ₃	O (%)	C (%)	N (%)	Fe
Fe-0.2Ti-0.3Y ₂ O ₃	0.2	-	0.3	0.47	0.02	0.009	Balance
Fe-14Cr-0.2Ti-0.3Y ₂ O ₃	0.2	14	0.3	0.38	0.02	0.006	Balance

5 MeV Ni ion beam was used to irradiate the alloy samples for a peak dose of 150 dpa at 600 °C and 700 °C in JANNUS irradiation facility [103]. This irradiation produced a damage of 40 dpa at the surface. The dose rate was 1.8×10^{-3} dpa/s [151]. SRIM software [167] was used to simulate the implanted Ni and vacancy profile as shown in Fig. 5.1. The left Y-axis shows the damage in terms of displacements per atom (dpa) and the right Y-axis presents the number of implanted ions per incident ion per angstrom (the μ unit presents count after multiplied with 10^{-6}).

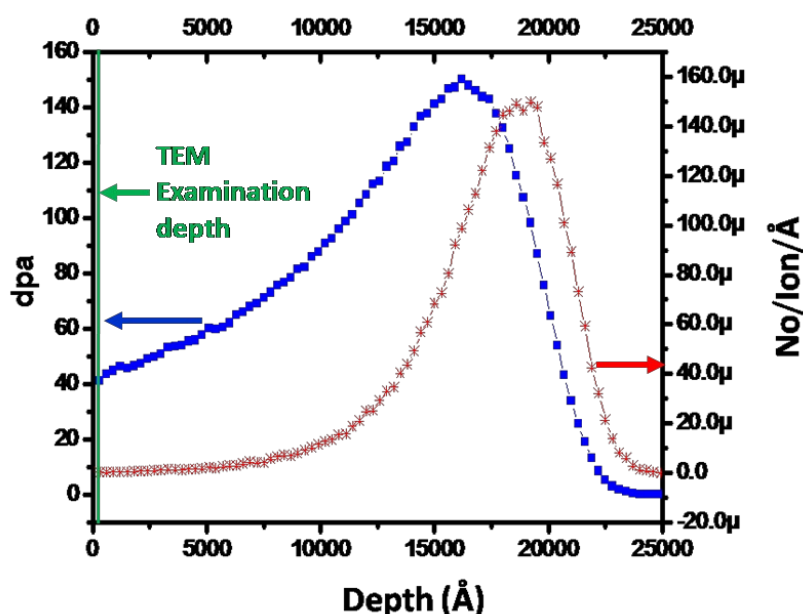


Figure 5.1 The implanted ion (in red) profile and damage (in blue) profile of 5 MeV Ni²⁺ ions in Fe matrix calculated through SRIM. The TEM observation was carried out at the surface -highlighted in green showing the sample surface facing irradiation[151]

Alloy microstructure and dispersed particles were studied using 200 KV HRTEM (make: Carl Zeiss; model: LIBRA 200 FE with in column omega filter). The information limit of the TEM was 0.13 nm. After irradiation of the samples, mechanical polishing was performed from the surface opposite to the side facing irradiation and around 50 μ thick foils were punched to get around 3 mm diameter disks. To study the effect of irradiation at the surface, lacomit varnish was used to protect the irradiated side and electropolishing was performed from the other side. Electropolishing was performed using a solution of ethanol, 2-butoxy ethanol and perchloric acid (7:2:1 volume ratio) at low temperature (-35 °C) to prepare TEM specimens. TEM samples were prepared from unirradiated part of the

irradiated samples to probe the effect of annealing. Electron energy loss spectroscopy technique was utilized to obtain TEM specimen thickness and the thickness of the samples was found in a range of 40 to 80 nm. ImageJ software [91] was used for measuring particle size from the TEM images.

5.3. Results

TEM study was carried out in the as prepared (i.e. before irradiation) Fe-0.2Ti-0.3Y₂O₃ and Fe-14Cr-0.2Ti-0.3Y₂O₃ alloys. TEM images were acquired from different locations of the specimens at low magnification for obtaining particle size distribution.

Figure 5.2(a) shows TEM image in bright field mode of the as prepared Fe-14-Cr-0.2Ti-0.3Y₂O₃ alloy. Nanoscale oxide particles of diameter 1-37 nm were observed. After irradiation at 600 °C and 40 dpa, the diameter range of the nano oxide particles became 1-15 nm in the Fe-14Cr-0.2Ti-0.3Y₂O₃ alloy (Fig. 5.2(b)). The effective pinning of dislocations at such nano particles is also visible from Fig. 5.2(b). The same alloy when irradiated up to 40 dpa at 700 °C, the discernible oxide particles seem to vanish and only the fine black dots can be found representing the possibility of presence of extremely fine particles (Fig. 5.2(c)). To understand the effect of temperature and irradiation on particle size, unirradiated annealed part of the Cr alloy at 700 °C was examined under TEM. The bright field image of the annealed sample is presented in Fig. 5.2(d) which shows that the oxide particles have coarsened as compared to the as prepared state.

To understand whether the fine black dots appeared from small clusters, or small dislocation loops or were irradiation-induced black dots, diffraction patterns were taken from the selected regions of the irradiated Fe-14Cr-0.2Ti-0.3Y₂O₃ alloy (Fig. 5.2(c)) containing only such black dots. Figure 5.2(e) and (f) shows the SAED patterns generated from the regions containing only black dots. The d spacing values corresponding to the diffraction spots were calculated to check consistency with different Miller indices (hkl) of possible crystal structure. ‘M’ and ‘P’ designates the spots arising from matrix and oxide particles respectively. Close matching was observed between the d spacing obtained and the theoretical d spacing of different crystal planes of Fe matrix-bcc and orthorhombic Y₂TiO₅ as tabulated in table 5.2.

APT study of self ion (5 MeV Fe³⁺) irradiated Fe-14Cr-0.2Ti-0.3Y₂O₃ alloy revealed that at 60 dpa, 700 °C cluster radius distribution has a mode at 1.4 nm [101].

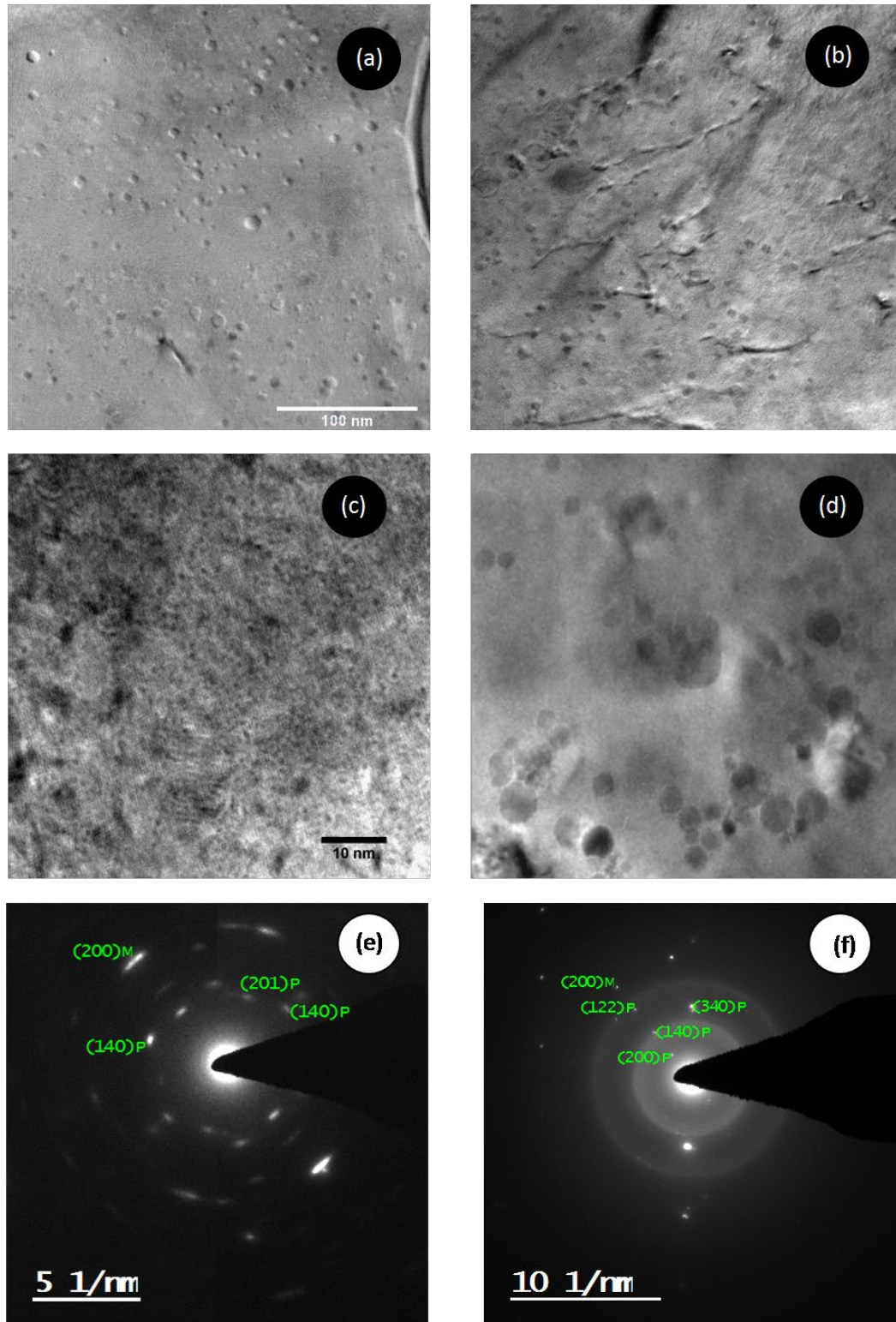


Figure 5.2 Low magnification bright field TEM images of the Fe-14Cr-0.2Ti-0.3Y₂O₃ alloy (a) as-prepared; 5 MeV Ni²⁺ ion irradiated alloy samples for the dose of (b) 40 dpa at 600 °C; (c) 40 dpa at 700 °C; and (d) annealed at 700 °C for 6 h. (scale bar shown in (a) applies for (b) and (d) also); (e),(f) SAED patterns obtained from (c) type regions showing indexed spots from different possible planes of matrix-M (bcc Fe) and particle-P (orthorhombic Y₂TiO₃) oxide crystal structures.

*Table 5.2 Analysis of SAED patterns obtained from Fe-14Cr-0.2Ti-0.3Y₂O₃ alloy irradiated up to 40 dpa at 700 °C with fine dots showing measured *d* spacing values consistent with different possible planes of matrix (Fe-bcc) and orthorhombic Y₂TiO₅ oxide crystal structures.*

Figures	<i>d</i> -measured (Å)	<i>d</i> (hkl) –theoretical (Å)	
		Y ₂ TiO ₅ Orthorhombic	Fe bcc
Fig. 5(b)	1.55		1.43 (200)
	3.11	3.01 (201)	
	2.68	2.69 (140)	
Fig. 5(c)	5.16	5.16 (200)	
	2.71	2.69 (140)	
	2.15	2.17 (340)	
	1.73	1.73 (122)	
	1.31		1.43 (200)

The TEM image (in the bright field mode) of the as prep Fe-0.2Ti-0.3Y₂O₃ alloy is shown in Fig. 5.3(a). Nanoscale oxide particles are found with diameter range of 3-33 nm. At 40 dpa, 600 °C, diameter range for the particles of the alloy became 1-23 nm as can be seen from Fig. 5.3(b). The same alloy at 40 dpa, 700 °C, was found with oxide particles with diameter ranging from 1-13 nm (Fig. 5.3(c)). Effect of annealing at 700 °C was also studied using TEM after preparing sample from the unirradiated part of the irradiated alloy disk. The particles in the annealed sample appeared to grow bigger in size showing coarsening in Fe-0.2Ti-0.3Y₂O₃ alloy (Fig. 5.3(d)).

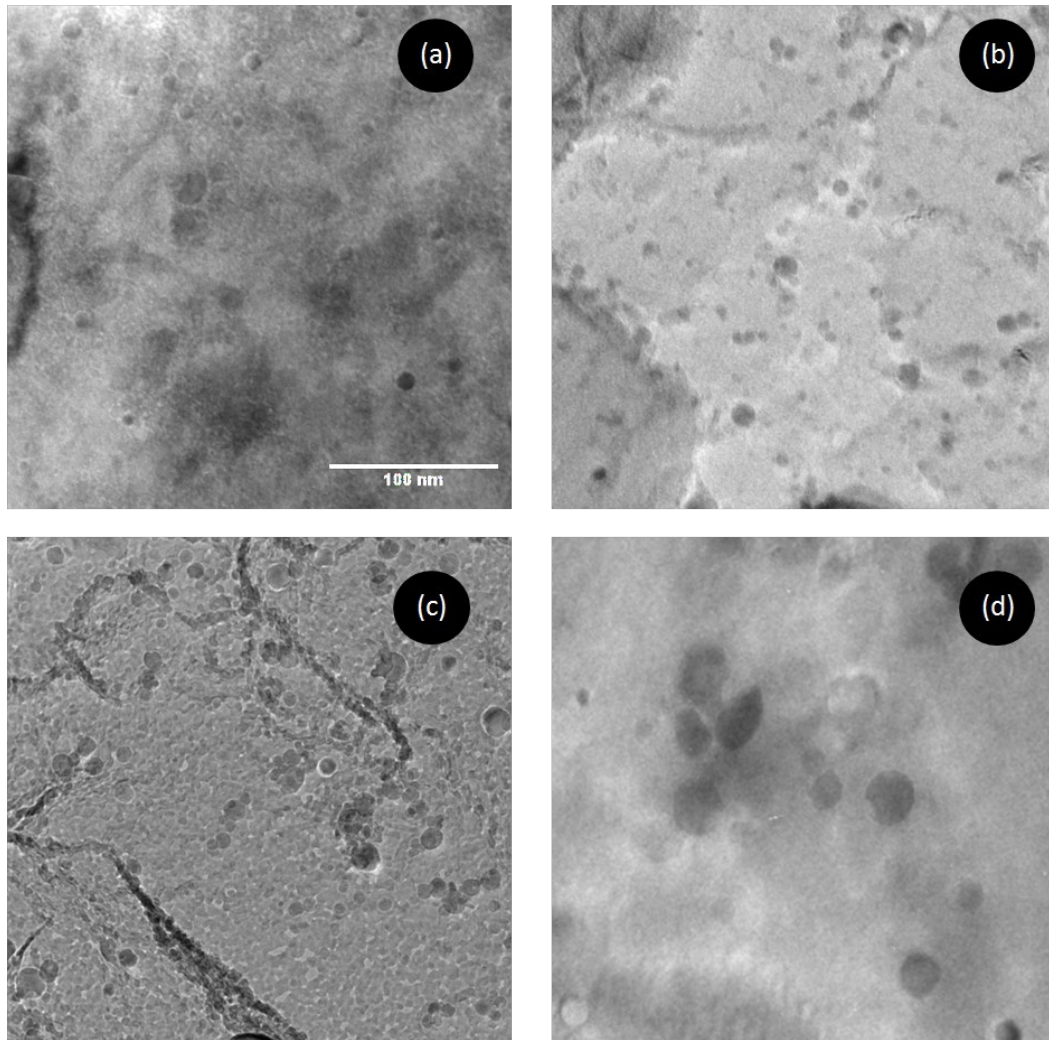


Figure 5.3 Low magnification bright field TEM images of the Fe-0.2Ti-0.3Y₂O₃ alloy (a) as-prepared; 5 MeV Ni²⁺ ion irradiated alloy samples for the dose of (b) 40 dpa at 600 °C; (c) 40 dpa at 700 °C; and (d) annealed at 700 °C for 6 h. (scale bar shown in (a) applies for all the images)

The particle size distribution, obtained from analysis of several TEM images of the as-prepared alloys of Fe-0.2Ti-0.3Y₂O₃ and Fe-14Cr-0.2Ti-0.3Y₂O₃ are shown in Fig. 5.4(a) and 5.4(b) respectively. The average particle size was found to be 8 nm and 4 nm in Fe-0.2Ti-0.3Y₂O₃ and Fe-14Cr-0.2Ti-0.3Y₂O₃ alloy respectively. As the Fe-14Cr-0.2Ti-0.3Y₂O₃ alloy was consolidated at 1150 °C and the Fe-0.2Ti-0.3Y₂O₃ alloy was consolidated at comparatively lower temperature 1050 °C, one may expect larger average particle size in the Cr-containing alloy based on the consolidation temperature [132]. It is worth noting that ODS alloys containing 9 and 18 wt% Cr consolidated at the same temperature has been studied [87] and finer particle size was observed in the higher Cr content alloy (with modal particle size 2.5 nm compared to 4.5 nm).

In the alloy without Cr, and in 9Cr ODS alloys, phase transformation to austenite will take place during the hot extrusion (some residual ferrite may be retained) [146]. Kim et al. found an increase in growth rate of the oxide particles upon phase transformation from alpha to gamma iron [147]. Loss of interface (particle-matrix) coherency and enhanced solute diffusion along gamma grain boundaries can explain this observation [148]. Hence, as the alpha–gamma phase transformation of the matrix will be suppressed by 14 wt % of Cr, the particle growth rate may be affected in an indirect way [145]. This fact implies that average oxide particle size may be reduced in presence of Cr in the alloy. However, annealing of the Fe-0.2Ti-0.3Y₂O₃ alloy was performed at 950 °C for 2 h whereas annealing of the Fe-14Cr-0.2Ti-0.3Y₂O₃ alloy was carried out at 1050 °C for 0.5 h and then 750 °C for 2 h. The lower annealing/tempering temperature can also contribute to influence/reduce the growth of oxide particles [151].

Upon Ni²⁺ ion irradiation in Fe-0.2Ti-0.3Y₂O₃ alloy at 40 dpa, 600 °C particle size distributions has an average value of ~ 5 nm ((Fig. 5.4(c)). At 40 dpa, 700 °C average particle size reduced only slightly to 4 nm (Fig. 5.4(e)). But standard deviation from the average value became much less at 40 dpa, 700 °C as compared to that at 40 dpa, 600 °C in Fe-0.2Ti-0.3Y₂O₃ alloy.

In the Fe-14Cr-0.2Ti-0.3Y₂O₃ alloy, at 40 dpa, 600 °C, particle size distribution shows an average value of 4 nm (Fig. 5.4 (d)) which reduces drastically to 1 nm after irradiation at 40 dpa, 700 °C (Fig. 5.4(f)). Upon annealing at 700 °C, as observed in the unirradiated portion of the alloys irradiated at 700 °C that has undergone same thermal treatment as the irradiated portion, average particle size increased to 12 nm and 13 nm in Fe-14 Cr-0.2Ti-0.3Y₂O₃ and Fe-0.2Ti-0.3Y₂O₃ alloy respectively.

Table 5.3 summarizes the average values obtained from particle size distribution for different conditions. These findings shows that ion irradiation at high temperature has a role to refine the particle size.

The volume density of particles was also calculated. Areal density was obtained from the TEM –bright field images and thickness measurement was carried out using EELS (Electron Energy Loss Spectroscopy). The electron transparent regions had a thickness value ranging from 40-80 nm with an average around 60 nm. This value was considered for calculating particle number density (refer table 5.3).

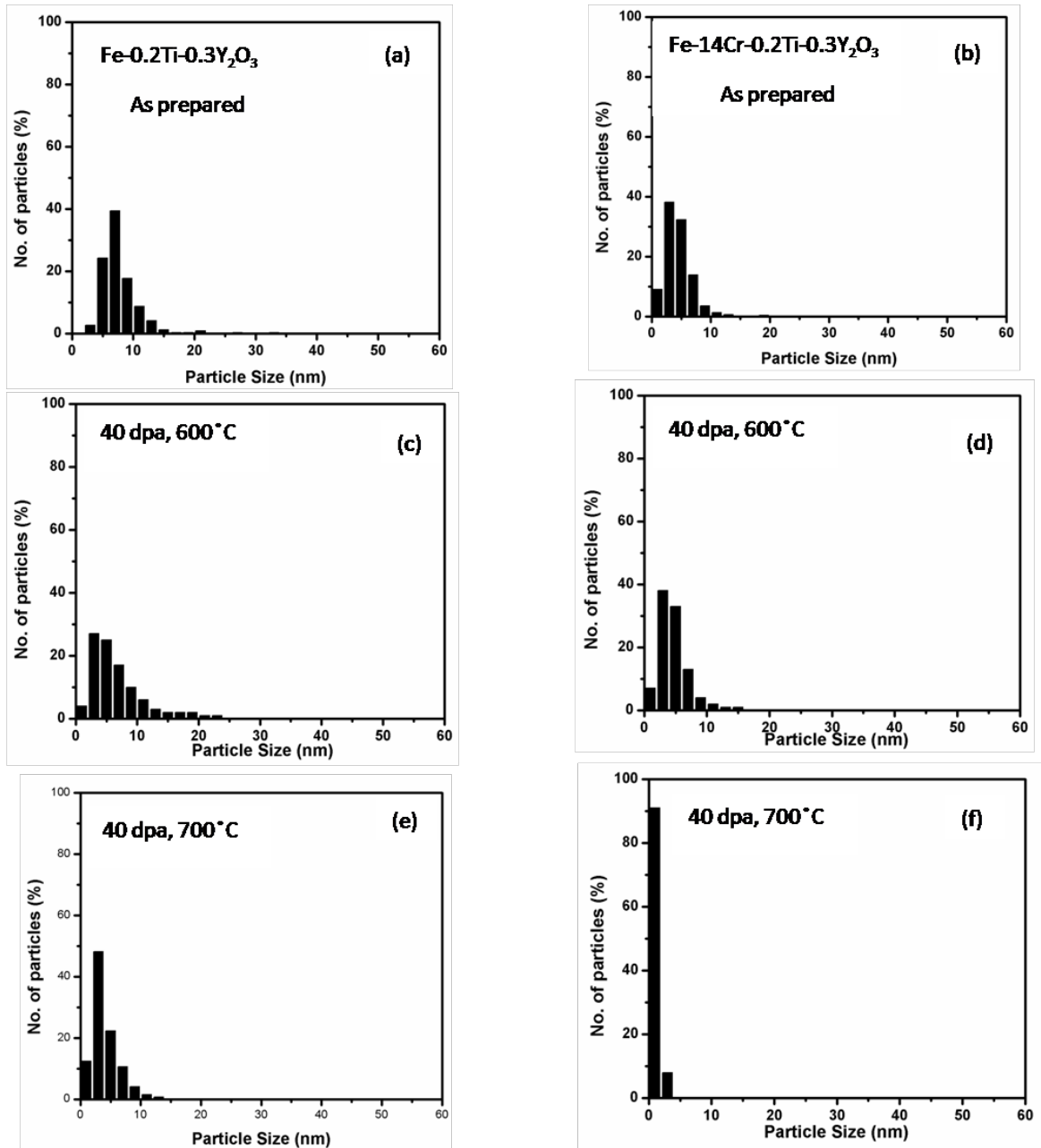


Figure 5.4 Oxide particle size distribution of Fe-0.2Ti-0.3Y₂O₃ alloy (a) as-prepared, and 5 MeV Ni²⁺ ion irradiated alloy samples for the dose of 40 dpa (c) at 600 °C; (e) at 700 °C. Oxide particle size distribution of Fe-14 Cr-0.2Ti-0.3Y₂O₃ alloy (b) as-prepared and 5 MeV Ni²⁺ ion irradiated alloy samples for the dose of 40 dpa (d) at 600 °C; (f) at 700 °C.

The particle density of the as-prepared alloy Fe-14Cr-0.2Ti-0.3Y₂O₃ was $4.3 \times 10^{22}/\text{m}^3$ which upon ion irradiation up to the dose of 40 dpa increased to $5.8 \times 10^{22}/\text{m}^3$ and $8.0 \times 10^{23}/\text{m}^3$ at irradiation temperatures of 600 and 700 °C respectively. In the annealed Fe-0.2Ti-0.3Y₂O₃ alloy (at 700 °C) particle density was calculated to be $5.4 \times 10^{21}/\text{m}^3$. Similarly the particle density evolution was also studied in Fe-0.2Ti-0.3Y₂O₃ alloy and the obtained values are tabulated in table 5.3 [151].

Table 5.3 Particle Size, density and volume fraction of the as-prepared and ion irradiated ODS alloys [151].

Alloy	Condition	Temperature (°C)	Average particle size (nm)	Particle Density (particles /m ³)	Particle volume fraction (%)
Fe-0.2Ti-0.3Y ₂ O ₃	As-prepared	-	8 ± 3	4.3 × 10 ²¹	0.5
	40 dpa	600	5 ± 4	3.5 × 10 ²²	0.8
	40 dpa	700	4 ± 2	12 × 10 ²²	2.1
	Annealed	700	13±6	11.8 × 10 ²¹	2.0
Fe-14Cr-0.2Ti-0.3Y ₂ O ₃	As-prepared	-	4 ± 2	4.3 × 10 ²²	0.2
	40 dpa	600	4 ± 2	5.8 × 10 ²²	0.7
	40 dpa	700	1 ± 1	8.0 × 10 ²³	0.07
	Annealed	700	12±9	5.4 × 10 ²¹	2.4

5.4. Discussion

5.4.1. Stability of particles

Variants of ODS steels have been bombarded with different ion beams, electrons or neutrons and stability of the oxide particles are confirmed in several reports. Dispersoids of size ~ 4 nm were found as stable in 150 keV Fe⁺ ion irradiated 12YWT alloy at 0.7 dpa [161]. Fast neutron irradiated 9Cr and 12Cr ODS alloys (dose: 2.5 to 15 dpa) at 330-500 °C were found with stable particles of size ~ 10 nm [168]. Kinoshita et al. [81] irradiated 13Cr ODS using 1 MeV electron beam up to 15 dpa at two different temperature of 350 and 450 °C and reported stable oxide particles. 13Cr ODS alloy was irradiated with 52 MeV Cr⁶⁺ and 4 MeV He⁺ ion beams up to 50 dpa at 475 °C and stable oxides were reported by Little et al. [69]. Rogozhkin et al. [169] irradiated a 13.5 Cr ODS without Ti using 4.8 MeV Ti ions up to 1 dpa and 3 dpa at room temperature and 300 °C. The authors found a notable increase of particle no. density for smaller (less than 4 nm) ones and shrinkage of bigger particles.

Typically clusters of size 2-6 nm are reported to remain stable under irradiation. Reports [160,161,164] and the foregoing discussion indicates that nano-particles of diameter 2 to 9 nm remain stable from a dose of 0.7 to 60 dpa from room temperature to 500 °C.

However, irradiation and temperature induced instability of oxide particles are also reported. 11 Cr-IDS & 13 Cr-IDK ODS after exposed to fast neutron in JOYO reactor at 450-561 °C up to 21 dpa were studied by Yamashita *et al.* [170] and their results reveals

that fine particles cease to exist as temperature and dose increases which results in increase in average particle size. Dubuisson *et al.* [171,172] studied PHENIX-irradiated 13Cr ODS steel at 81 dpa, 400-580 °C and the authors found that smaller oxides undergo complete dissolution and partially dissolved coarser oxides gets surrounded by halo of smaller oxides as can be seen from Fig. 5.5.

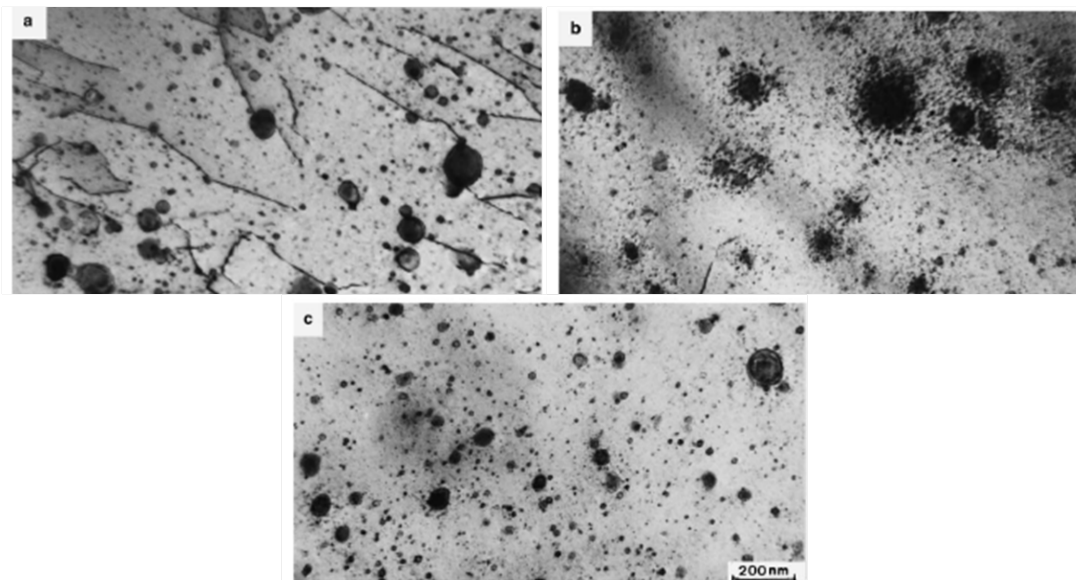


Figure 5.5 The oxide dispersion in the DY ODS steel following 600 hour neutron irradiation, showing halos of smaller particles around larger particles: (a) before irradiation, (b) after irradiation at 532 °C to 78.8 dpa, (c) after irradiation at 580 °C to 30.5 dpa. (BF-TEM micrographs scale bar of (c) applies for (a) and (b) also)[172].

Dissolution of very fine particles and stability of large size particles was reported in 12 Cr ODS at 47 dpa produced by electron bombardment (25-450 °C) [173]. Study of triple ion beam (Fe^{5+} , He^+ , H^+) irradiated 14 Cr ODS at 30 dpa, 600 °C revealed slight coarsening of finer oxides with diameter <5 nm [174].

Lu et al studied evolution of particles with dose in 9 Cr ODS and found gradual dissolution of oxide particles with sequential changes in morphology. The initially spherical oxides (prior irradiation) became irregular, next needle shaped and finally fine small particles as the damage level increased from 135, 188 and 300 dpa respectively [175]. Yano *et al.* [176] fabricated micro compression pillars from Fe^{2+} ion irradiated model Fe-9Cr ODS alloy and performed in-situ compression test under TEM. The authors observed minimal change in yield strength at 3, 100 dpa (irradiation temp. 500 °C) and commented that irradiation induced strengthening was probably offset by softening due to partial dissolution of oxide particles [176]. Robertson et al. [136] investigated high temp

dose stability of yttria particles in pure Fe under dual beam irradiation (Fe & He ion beam) at 600 °C. They confirmed particle stability up to 25 dpa with 40 ppm He but observed pronounced change in particle size at 80 dpa with 360 ppm He. Allen et al. used 5 MeV Ni ion irradiated 9Cr ODS to determine particle stability over a temp range of 500-700 °C up to dose level of 150 dpa. They observed that average particle size decrease and density increases with dose [84]. Zhanbing et al. [177] employed ion accelerator and HVEM (High Voltage Electron Microscope) to implant 50 ppm/dpa hydrogen ion and create 15 dpa damage respectively in a 12Cr ODS. They observed irradiation induced irregularization of large sized particle and matrix interface at 15 dpa, 350 °C to 550 °C. Wharry et al. [178] reviewed irradiation induced evolution of oxide particles in Fe-Cr (bcc) system. They could not draw any correlation between particle size, temperature of irradiation and irradiation induced damage level. The authors pointed out that explanations offered to understand irradiation induced changes in nanoparticles revolve around four main themes i.e. 1) ballistic dissolution, 2) Ostwald ripening, 3) irradiation enhanced diffusion and 4) homogeneous nucleation.

The present study shows that at 40 dpa and 600 °C, the particle size of the Fe-0.2Ti-0.3Y₂O₃ alloy gets reduced. A further reduction is observed at 700 °C but only slightly. However, the standard deviation lessens at 700 °C. This indicates a notable tapering of the particle size distribution range at 700 °C.

In the Cr added alloy, average particle size does not change upon irradiation at 40 dpa, 600 °C. But at 700 °C, average particle size drastically reduces with increase in particle density as can be found from table 5.3. However, annealing induced Oswald ripening or increase in particle size was observed in both the alloys. Hence, the refinement of particle size under irradiation at different temperatures was entirely because of the ion irradiation.

The present work clearly shows that at 40 dpa, as the irradiation temp increases from 600 to 700 °C particle size decreases appreciably. Fig 5.4 shows non existence of the larger particles of size more than 20nm at 600 °C in both the alloys although they were found before irradiation. This effect is remarkable at 700 °C. The results suggest that high temperature irradiation plays an important role in dissolution of coarser oxide particles which then generates new finer particles. These particles add on to the pre-existing fine particles (increasing finer particles count) and move the histogram in the direction of lower particle size.

In case of Oswald ripening process, larger particles grows at the expense of smaller ones through dissolution of the later and re-deposition on the former species. This is opposite to what observed in present study. The present observations suggest that upon irradiation, dissolution of the particles takes place via ballistic effect (through recoils and inducing disorder) and re-precipitation occurs at higher temperature through diffusion process [151].

Table 5.3 gives an overview of oxide particle volume fraction obtained from TEM data analysis. The volume fraction was found as 0.5% and 0.2% in as prepared Fe-0.2Ti-0.3Y₂O₃ and Fe-14Cr-0.2Ti-0.3Y₂O₃ alloy respectively. Volume fraction of particles was more in the Cr added alloy which shows consistency with the higher number density of particles found in Cr added alloy as compared to Fe-0.2Ti-0.3Y₂O₃ alloy.

In Fe-0.2Ti-0.3Y₂O₃ alloy, an increase in volume fraction by 0.3% is observed when irradiated up to 40 dpa at 600 °C. At 40 dpa, 700 °C, volume fraction becomes 2% with increase in particle number density. A simultaneous reduction in particle size suggests dissolution caused by irradiation followed by re-precipitation at high temperature determine the particle evolution in Fe-0.2Ti-0.3Y₂O₃ alloy.

In Fe-14Cr-0.2Ti-0.3Y₂O₃ alloy when irradiated up to 40 dpa, 600 °C, particle number density increases slightly with increase in volume fraction to 0.7 %. At 40 dpa, 700 °C volume fraction became 0.07% only showing a large reduction accompanied by a large increase in particle number density. The reduction in volume fraction implies dissolution. But simultaneous increase in number density of particles indicates presence of extremely fine particle size. This suggests that initially present particles get almost dissolved and some of the ejected atoms act as new nucleation centres [151].

K. Kondo et al. [179] tried to draw correlation between irradiation induced microstructure and irradiation hardening through theoretical calculation using dispersed barrier hardening model from the following relation [180,181]:

$$\Delta\sigma = \alpha\mu Mb (\Delta Nd)^{1/2}$$

Equation 5.1

where, $\Delta\sigma$: increase of yield strength, α : dislocation-defect interaction strength (=0.5), μ : shear modulus (=82 GPa), M : Taylor factor (=3.06), b : dislocation burgers vector (~0.25 nm), N : number density, and d : mean size of defect clusters induced by irradiation [181]. The calculated yield stress ($\Delta\sigma$) can be converted to vickers hardness (ΔHV) can then be

obtained from the conversion relation $\Delta\sigma = 3.06\Delta HV$ as was suggested by Busby et al. [182].

Applying the above equations in the present study, 39.5 and 59.5 HV was the estimated increase in hardness at 600 and 700 °C respectively in Fe-0.2Ti-0.3Y₂O₃ alloy at 40 dpa. Similarly 24.6 and 87.8 HV was the estimated increase in hardness at 600 and 700 °C respectively in Fe-14Cr-0.2Ti-0.3Y₂O₃ alloy at 40 dpa. The increase in hardness derived from particle size refinement with increase in number density can improve high temperature creep properties of the alloy components during service.

5.4.2. Effect of Alloying element in particle dissolution process

N. Li *et al.* [173] studied an ion irradiated tri-layer thin film of Fe-20 at% Cr and Y₂O₃ and observed partial amorphization of the Y₂O₃ layer driven by Cr enrichment along with void formation showing effect of Cr in phase transition. In the present study, it is found that the average particle size decreases at 40 dpa in both the Fe-0.2Ti-0.3Y₂O₃ and Fe-14Cr-0.2Ti-0.3Y₂O₃ alloy at 700 °C irradiated alloys but histogram tail of the particle size distribution is quite distinct for the Fe-0.2Ti-0.3Y₂O₃ and Fe-14Cr-0.2Ti-0.3Y₂O₃ alloy.

In the Cr alloy the limited range of particle size distribution compress the histogram width appreciably. But, in the Fe-0.2Ti-0.3Y₂O₃ alloy, frequency of larger particles lessens but is found to exist. Hence, Cr makes a substantial impact in dissolution of the coarser particles present in the ODS alloy. The preferred dissolution of particles in Cr alloy could be explained through the following:

I) In as received condition, Cr added alloy had finer particles as compared to those present in Fe-0.2Ti-0.3Y₂O₃ alloy. The fraction of the larger particles (with diameter >20 nm) was 1.5% and 0.4% in the Fe-0.2Ti-0.3Y₂O₃ and Fe-14Cr-0.2Ti-0.3Y₂O₃ alloy respectively. Under irradiation, these coarser particles will start dissolving increasing the frequency of the finer ones. The process of gradual dissolution of these coarser particles (at the same irradiation dose and temperature) will enhance the frequency of the finer particles much faster in that alloy which offers initial coarse particles of comparatively smaller size [151]. Thus dissolution process can be speedy in alloy containing Cr offering relatively finer particles.

II) Dissolution of Y₂O₃ can take place only when both the Y and O atoms are supplied with required amount of displacement energy [81]. This energy value is 57 eV in Y₂O₃ [183,184]. Displacement energy of Fe is 40 eV [84]. If one assumes that Y-Ti-O

complex oxides also have similar displacement energy, then number of vacancies produced in Fe matrix upon irradiation will dominate. This concentration gradient of vacancies will create resultant vacancy diffusion towards particle. Absorption of these vacancies will release particle atoms leading to dissolution or mass loss. Displacement energy of Cr is even less (34 eV) than that for Fe as reported by Setyawan *et al.* [185]. All the oxide particles in the as prepared Fe-14Cr-0.2Ti-0.3Y₂O₃ alloy were detected with Cr rich shell around the particle core region through APT study [145].

Thus, it is expected that vacancies will be easily produced surrounding the oxide particles of Cr alloy under irradiation. This suggest that presence of Cr shell around the core-ODS particle can help in particle dissolution.

5.5. Conclusions

Ion irradiation response of two model ODS alloys of composition Fe-0.2Ti-0.3Y₂O₃ and Fe-14Cr-0.2Ti-0.3Y₂O₃ was studied. Evolution of oxide particles under ion irradiation was investigated for a damage level of 40 dpa at irradiation temp of 600 and 700 °C in both the alloys. Irradiation at 700 °C substantially decreases the particle size. In presence of Cr, the size reduction becomes much more pronounced. Two possible reasons were figured out to explain the role of Cr in speeding up the oxide particle dissolution process:

I) Cr added alloy had comparatively smaller particles in the as prepared state. Dissolution of these particles upon irradiation promptly increases the frequency of much finer particles.

II) Cr forms shell around particles and gets displaced at lower energy. This can be responsible for a net vacancy bias towards particle favoring dissolution/mass loss. Estimation of irradiation induced hardness showed an appreciable increase. This may be advantageous in view of high temperature creep resistance of the clad/wrapper application.

References

- [1] Ansolabehere S., Deutch J., Driscoll Gray P.E.E.M., Holdren J.P., Joskow P.L., Lester R.K., Christopher Jones E.P.E.J.M.N.E.T.E.S.B.N.H., The future of nuclear power , An interdisciplinary MIT study, *Cambridge, MA USA*, (2009)
- [2] Raj B., Mudali U.K., Materials science and technology: Research and challenges in nuclear fission power, *Proc. Indian Natl. Sci. Acad.*, (2015), **81**, 801–826
- [3] He P., On the structure-property correlation and the evolution of nanofeatures in 12-13.5% Cr oxide dispersion strengthened ferritic steels, Karlsruhe Instituts für Technologie, China, (2013)
- [4] François Gauché, GIF R&D Outlook for Generation IV Nuclear Energy Systems 2018 Update, (2018)
- [5] Board-GIF, Generation IV Systems, Webpage, (2020), 3–4
- [6] Allibert M. et al, Handbook of Generation IV Nuclear Reactors, *Woodhead publishing, Elsevier*, (2016)
- [7] Sinha R.K., Chellapandi P., Srinivasan G., Dulera I., Vijayan P.K., Chande S.K., Generation IV concepts: India, *Elsevier Ltd*, (2016)
- [8] Murty K.L., Charit I., Structural materials for Gen-IV nuclear reactors: Challenges and opportunities, *J. Nucl. Mater.*, (2008), **383**, 189–195
- [9] Hilger I., Influence of mixrostructure features on the irradiation behaviour of ODS Fe-14Cr alloys, Dissertation, Institute of Ion-Beam Physics and Materials Research at the Helmholtz- Zentrum Dresden-Rossendorf, (2017)
- [10] Chant I., Murty K.L., Structural materials issues for the next generation fission reactors, *Jom*, (2010), **62**, 67–74
- [11] Yvon P., Le Flem M., Cabet C., Seran J.L., Structural materials for next generation nuclear systems: Challenges and the path forward, *Nucl. Eng. Des.*, (2015), **294**, 161–169
- [12] Kirk M.A., Robertson I.M., Jenkins M.L., English C.A., Black T.J., Vetrano J.S., The collapse of defect cascades to dislocation loops, *J. Nucl. Mater.*, (1987), **149**, 21–28
- [13] Jenkins M.L., Kirk M.A., Phythian W.J., Experimental studies of cascade phenomena in metals, *J. Nucl. Mater.*, (1993), **205**, 16–30
- [14] A. Strang, R.D. Conroy, W.M. Banks, M. Blackler, J. Leggett, G.M. McColvin, S. Simpson M.S., Parsons 2003, engineering issues in turbine machinery, power plant and renewables, In: Proceedings of the Sixth International Charles Parsons Turbine Conference 16-18 September Trinity College Dublin, Ireland, (2003)
- [15] Klueh R.L., Elevated temperature ferritic and martensitic steels and their application to future nuclear reactors, *Int. Mater. Rev.*, (2004), **50**, 287–310
- [16] Carlan Y. de, Bechade J.L., Dubuisson P., Seran J.L., Billot P., Bougault A., *et al.*, CEA developments of new ferritic ODS alloys for nuclear applications, *J. Nucl. Mater.*, (2009), **386–388**, 430–432
- [17] Zinkle S.J., Busby J.T., Structural materials for fission & fusion energy, *Mater. Today*, (2009), **12**, 12–19

- [18] Cheon J.S., Lee C.B., Lee B.O., Raison J.P., Mizuno T., Delage F., Carmack J., Sodium fast reactor evaluation: Core materials, *J. Nucl. Mater.*, (2009), **392**, 324–330
- [19] Tselishchev A. V., Ageev V.S., Budanov Y.P., Ioltukhovskii A.G., Mitrofanova N.M., Leontieva-Smirnova M. V., Shkabura I.A., Zabud'Ko L.M., Kozlov A. V., Mal'Tsev V. V., Povstyanko A. V., Development of structural steel for fuel elements and fuel assemblies of sodium-cooled fast reactors, *At. Energy*, (2010), **108**, 274–280
- [20] Odette G.R., Alinger M.J., Wirth B.D., Recent Developments in Irradiation-Resistant Steels, *Annu. Rev. Mater. Res.*, (2008), **38**, 471–503
- [21] Ratti M., Development of new ferritic / martensitic steels for fuel cladding in fast neutron reactors, Institut Polytechnique de Grenoble, 38, France, (2009)
- [22] Russell K.C., Brown L.M., A dispersion strengthening model based on differing elastic moduli applied to the iron-copper system, *Acta Metall.*, (1972), **20**, 969–974
- [23] Wasilkowska A., Bartsch M., Messerschmidt U., Herzog R., Czyrska-Filemonowicz A., Creep mechanisms of ferritic oxide dispersion strengthened alloys, *J. Mater. Process. Technol.*, (2003), **133**, 218–224
- [24] Ribis J., De Carlan Y., Interfacial strained structure and orientation relationships of the nanosized oxide particles deduced from elasticity-driven morphology in oxide dispersion strengthened materials, *Acta Mater.*, (2012), **60**, 238–252
- [25] Schäublin R., Ramar A., Baluc N., de Castro V., Monge M.A., Leguey T., Schmid N., Bonjour C., Microstructural development under irradiation in European ODS ferritic/martensitic steels, *J. Nucl. Mater.*, (2006), **351**, 247–260
- [26] Was G.S., Fundamentals of Radiation Materials Science, *Springer Berlin Heidelberg, Berlin, Heidelberg*, (2019)
- [27] Norgett M.J., Robinson M.T., Torrens I.M., A proposed method of calculating displacement dose rates, *Nucl. Eng. Des.*, (1975), **33**, 50–54
- [28] Averback R.S., Atomic displacement processes in irradiated metals, *J. Nucl. Mater.*, (1994), **216**, 49–62
- [29] Janeschitz G., Boccaccini L., Fietz W.H., Goldacker W., Ihli T., Meyder R., Moeslang A., Norajitra P., Development of fusion technology for DEMO in Forschungszentrum Karlsruhe, *Fusion Eng. Des.*, (2006), **81**, 2661–2671
- [30] Bai X.M., Voter A.F., Hoagland R.G., Nastasi M., Uberuaga B.P., Efficient annealing of radiation damage near grain boundaries via interstitial emission, *Science*, (2010), **327**, 1631–1634
- [31] Miller M.K., Russell K.F., Hoelzer D.T., Characterization of precipitates in MA/ODS ferritic alloys, *J. Nucl. Mater.*, (2006), **351**, 261–268
- [32] Amirthapandian S., Ion Beam Synthesis and Characterization of Nanoscale Granular Magnetic Materials, Thesis, University of Madras, (2004)
- [33] Jegadeesan P., Radiation effects in oxides used in nuclear applications, Thesis, Homi Bhabha National Institute, IGCAR, (2019)
- [34] Gokhman A., Bergner F., Cluster dynamics simulation of point defect clusters in neutron irradiated pure iron, *Radiat. Eff. Defects Solids*, (2010), **165**, 216–226

-
- [35] Was G.S., Allen T., Radiation-induced segregation in multicomponent alloys: Effect of particle type, *Mater. Charact.*, (1994), **32**, 239–255
- [36] Malerba L., Caro A., Wallenius J., Multiscale modelling of radiation damage and phase transformations: The challenge of FeCr alloys, *J. Nucl. Mater.*, (2008), **382**, 112–125
- [37] Was G.S., Jiao Z., Getto E., Sun K., Monterrosa A.M., Maloy S.A., Anderoglu O., Sencer B.H., Hackett M., Emulation of reactor irradiation damage using ion beams, *Scr. Mater.*, (2014), **88**, 33–36
- [38] Ghoniem N.M., Fusion Conditions: Radiation Damage Correlation No Title, *Encycl. Mater. Sci. Technol. (Second Ed.)*, (2001), 3413–3417
- [39] Abromeit C., Aspects of simulation of neutron damage by ion irradiation, *J. Nucl. Mater.*, (1994), **216**, 78–96
- [40] Was G.S., Averback R.S., Radiation damage using ion beams, *Compr. Nucl. Mater.*, (2012), **1**, 195–221
- [41] Mansur L.K., Coghlan W.A., Mechanisms of helium interaction with radiation effects in metals and alloys: A review, *J. Nucl. Mater.*, (1983), **119**, 1–25
- [42] Gilbert M.R., Transmutation and He Production in W and W-alloys, *Culham Science Centre, Abingdon, Oxfordshire, OX14 3DB, UK*, (2010)
- [43] Dai Y., Odette G.R., Yamamoto T., The effects of helium in irradiated structural alloys, *Compr. Nucl. Mater.*, (2012), **1**, 141–193
- [44] Gai X., Lazauskas T., Smith R., Kenny S.D., Helium bubbles in bcc Fe and their interactions with irradiation, *J. Nucl. Mater.*, (2015), **462**, 382–390
- [45] Kaspar T.C., Bowden M.E., Wang C.M., Shutthanandan V., Overman N.R., Van Ginhoven R.M., Wirth B.D., Kurtz R.J., Epitaxial Fe/Y₂O₃ interfaces as a model system for oxide-dispersion-strengthened ferritic alloys, *J. Nucl. Mater.*, (2015), **457**, 352–361
- [46] Mathew M.D., Lecture 1 irradiation effects, *Ppt*, (2012)
- [47] Christopher David, a Study on the Effect of Titanium on Void Swelling Behavior of, University of Madras, (2013)
- [48] Odette G.R., On mechanisms controlling swelling in ferritic and martensitic alloys, *J. Nucl. Mater.*, (1988), **155–157**, 921–927
- [49] Sniegowski J.J., Wolfer W.G., On the physical basis for the swelling resistance of ferritic steels, In: In Top Conf. Ferritic Alloys Use Nucl. Energy Technol., *New York*, (1984), 579–586
- [50] Boulnat X., FAST high-temperature consolidation of Oxide-Dispersion Strengthened (ODS) steels : process, microstructure, precipitation, properties., *Thesis*, (2014), 202
- [51] Ukai S., Harada M., Okada H., Inoue M., Nomura S., Shikakura S., Asabe K., Nishida T., Fujiwara M., Alloying design of oxide dispersion strengthened ferritic steel for long life FBRs core materials, *J. Nucl. Mater.*, (1993), **204**, 65–73
- [52] Klimiankou M., Lindau R., Möslang A., TEM characterization of structure and composition of nanosized ODS particles in reduced activation ferritic-martensitic steels, *J. Nucl. Mater.*, (2004), **329–333**, 347–351
-

-
- [53] Iwata N.Y., Kasada R., Kimura A., Okuda T., Inoue M., Abe F., Ukai S., Ohnuki S., Fujisawa T., Characterization of mechanically alloyed powders for high-Cr oxide dispersion strengthened ferritic steel, *ISIJ Int.*, (2009), **49**, 1914–1919
- [54] Sakasegawa H., Chaffron L., Legendre F., Boulanger L., Cozzika T., Brocq M., de Carlan Y., Correlation between chemical composition and size of very small oxide particles in the MA957 ODS ferritic alloy, *J. Nucl. Mater.*, (2009), **384**, 115–118
- [55] Dave T., Effect of hot rolling and intermittent annealing on the texture evolution of monotectoid BCC Zr-Nb, Georgia Institute of Technology, (2017)
- [56] Sahoo B., Recrystallization texture development in CP-Titanium, Thesis, NIT, Rourkela, (2013)
- [57] C. S. Barrett T.B.M., Structure of metals, 3rd ed., *McGraw-Hill Book Company*, New York, (1966)
- [58] McNelley T.R., Swisher D.L., Prez-Prado M.T., Deformation bands and the formation of grain boundaries in a superplastic aluminum alloy, *Metall. Mater. Trans. A Phys. Metall. Mater. Sci.*, (2002), **33**, 279–290
- [59] Suwas S., Gurao N.P., Crystallographic texture in materials, *J. Indian Inst. Sci.*, (2008), **88**, 151–177
- [60] Wang Y.N., Huang J.C., Texture analysis in hexagonal materials, *Mater. Chem. Phys.*, (2003), **81**, 11–26
- [61] Bunge H. J., No Title, *Z. Met.*, (1965), **56**, 872–874
- [62] Roe R.J., Description of crystallite orientation in polycrystalline materials. III. General solution to pole figure inversion, *J. Appl. Phys.*, (1965), **36**, 2024–2031
- [63] JA Szpunar H.B., Texture, Anisotropy in Magnetic Steel, Directional Properties of Materials, *Cuvllier Verlag Gttingen*, (1988), 129
- [64] Bessieres, J. H., JJ and Eberhardt A., No Title, *Textures Microstruct.*, (1991), **14**, 157
- [65] Kestens L.A.I., Pirgazi H., Texture formation in metal alloys with cubic crystal structures, *Mater. Sci. Technol. (United Kingdom)*, (2016), **32**, 1303–1315
- [66] Hirsch J., Lücke K., Description and Presentation Methods for Textures, *Textures Microstruct.*, (1988), **8**, 131–151
- [67] Oñorbe E., Hernández-Mayoral M., Morrison A., Serrano M., Study of the microstructure and small punch behavior of a 9Cr ODS tube, *Nucl. Mater. Energy*, (2019), **20**, 100698
- [68] Huet J.J., Coheur L., De Bremaecker A., De Wilde L., Gedopt J., Hendrix W., Vandermeulen W., Fabrication and Mechanical Properties of Oxide Dispersion Strengthening Ferritic Alloy Canning Tubes for Fast Reactor Fuel Pins., *Nucl. Technol.*, (1985), **70**, 215–219
- [69] Gelles D.S., Nanstad R.K., Kumar A.S., Little E.A., Effects of Radiation on Materials: 17th International Symposium, *Eff. Radiat. Mater. 17th Int. Symp.*, (1996), **STP1270**
- [70] Ukai S., Nishida T., Okuda T., Yoshitake T., R&D of oxide dispersion strengthened ferritic martensitic steels for FBR, *J. Nucl. Mater.*, (1998), **258–263**, 1745–1749
-

- [71] Narita T., Ukai S., Kaito T., Ohtsuka S., Kobayashi T., Development of two-step softening heat treatment for manufacturing 12Cr-ODS ferritic steel tubes, *J. Nucl. Sci. Technol.*, (2004), **41**, 1008–1012
- [72] Ukai S., Mizuta S., Yoshitake T., Okuda T., Fujiwara M., Hagi S., Kobayashi T., Tube manufacturing and characterization of oxide dispersion strengthened ferritic steels, *J. Nucl. Mater.*, (2000), **283–287**, 702–706
- [73] Chou T.S., Bhadeshia H.K.D.H., Crystallographic texture in mechanically alloyed oxide dispersion-strengthened MA956 and MA957 steels, *Metall. Trans. A*, (1993), **24**, 773–779
- [74] Capdevila C., Chen Y.L., Lassen N.C.K., Jones A.R., Bhadeshia H.K.D.H., Heterogeneous deformation and recrystallisation of iron base oxide dispersion strengthened PM2000 alloy, *Mater. Sci. Technol.*, (2001), **17**, 693–699
- [75] Okada H., Ukai S., Inoue M., Effects of Grain Morphology and Texture on High Temperature Deformation in Oxide Dispersion Strengthened Ferritic Steels, *J. Nucl. Sci. Technol.*, (1996), **33**, 936–943
- [76] H. Regle and A. Alamo, Secondary recrystallization of oxide dispersion strengthened ferritic alloys, *J. Phys IV*, (1993), **C7**, 727
- [77] Murali D., Panigrahi B.K., Valsakumar M.C., Chandra S., Sundar C.S., Raj B., The role of minor alloying elements on the stability and dispersion of yttria nanoclusters in nanostructured ferritic alloys: An ab initio study, *J. Nucl. Mater.*, (2010), **403**, 113–116
- [78] Ukai S., Fujiwara M., Perspective of ODS alloys application in nuclear environments, *J. Nucl. Mater.*, (2002), **307–311**, 749–757
- [79] Yamashita S., Akasaka N., Ukai S., Ohnuki S., Microstructural development of a heavily neutron-irradiated ODS ferritic steel (MA957) at elevated temperature, *J. Nucl. Mater.*, (2007), **367–370 A**, 202–207
- [80] Gelles D.S., Microstructural examination of commercial ferritic alloys at 200 dpa, *J. Nucl. Mater.*, (1996), **233–237**, 293–298
- [81] Kinoshita H., Akasaka N., Takahashi H., Shibahara I., Onose S., Microstructural change on electron irradiated oxide dispersion strengthened ferritic steels, *J. Nucl. Mater.*, (1992), **191–194**, 874–878
- [82] Certain A., Kuchibhatla S., Shutthanandan V., Hoelzer D.T., Allen T.R., Radiation stability of nanoclusters in nano-structured oxide dispersion strengthened (ODS) steels, *J. Nucl. Mater.*, (2013), **434**, 311–321
- [83] Mohan S., Balaji S., Amirthapandian S., David C., Panigrahi B.K., Effect of heavy ion irradiation at low temperature in Fe-14Cr-0.2Ti-0.3Y₂O₃, *Adv. Mater. Lett.*, (2015), **6**, 442–445
- [84] Allen T.R., Gan J., Cole J.I., Miller M.K., Busby J.T., Shutthanandan S., Thevuthasan S., Radiation response of a 9 chromium oxide dispersion strengthened steel to heavy ion irradiation, *J. Nucl. Mater.*, (2008), **375**, 26–37
- [85] Lescoat, M. L., J. Ribis, Y. Chen, E. A. Marquis, E. Bordas, P. Trocellier, Y. Serruys, A. Gentils, O. Kaïtasov, Y. de Carlan A.L., Radiation-induced Ostwald ripening in oxide dispersion strengthened ferritic steels irradiated at high ion dose, *Acta Mater.*, (2014), **78**, 328–340

- [86] Swenson M.J., Wharry J.P., The comparison of microstructure and nanocluster evolution in proton and neutron irradiated Fe-9%Cr ODS steel to 3 dpa at 500 °c, *J. Nucl. Mater.*, (2015), **467**, 97–112
- [87] Vijay R., Nagini M., Sarma S.S., Ramakrishna M., Reddy A. V., Sundararajan G., Structure and properties of Nano-scale oxide-dispersed iron, *Metall. Mater. Trans. A Phys. Metall. Mater. Sci.*, (2014), **45**, 777–784
- [88] Sundararajan G., Vijay R., Reddy A. V., Development of 9Cr ferritic-martensitic and 18Cr ferritic oxide dispersion strengthened steels, *Curr. Sci.*, (2013), **105**, 1100–1106
- [89] Williams D.B., Carter C.B., Transmission Electron Microscopy A Textbook for Materials Science, *Springer Sci.*, (2009), 179
- [90] Wilkinson A.J., Britton T. Ben, Strains, planes, and EBSD in materials science, *Mater. Today*, (2012), **15**, 366–376
- [91] Ferreira T., Rasband W., ImageJ User Guide User Guide ImageJ, *Image J User Guid.*, (2012), **1.46r**
- [92] Hasan L.M., lecture on hardness test, *Lect. 6 Hardness*, https://uomustansiriyah.edu.iq/media/lectures/5/5_2020_03_19/06_35_43_PM.pdf, n.d.
- [93] Kinchin, The displacement of atoms in solids during irradiation, *Solid State Phys.*, (1956), **2**, 307
- [94] Niels Bohr, XXII . The Penetration of Atomic Particles through Matter, (1948), **8**
- [95] Brinkman J.A., On the nature of radiation damage in metals, *J. Appl. Phys.*, (1954), **25**, 961–970
- [96] Silcox J., Hirsch P.B., Dislocation loops in neutron-irradiated Copper, *Philos. Mag.*, (1959), **48**, 1356–1374
- [97] Jenkins M.L., Kirk M.A., Characterization of Radiation Damage by Transmission Electron Microscopy, *Institute of Physics Publishing, Bristol and Philadelphia, U.S.*, (2015)
- [98] Averback, R. S. B.R. and M.K.L., Ion irradiation studies of the damage function of copper and silver, (1978), **32**, 147–156
- [99] Diaz de la Rubia T., Averback R.S., Benedek R., King W.E., Role of Thermal Spikes in Energetic Collision Cascades, *Phys. Rev. Lett.*, (1987), **59**, 1930–1933
- [100] Norgett M.J., Robinson M.T., Torrens I.M., A proposed method of calculating displacement dose rates, *Nucl. Eng. Des.*, (1975), **33**, 50–54
- [101] London A.J., Irradiation Damage of Oxide Dispersion Strengthened Steels, (2015)
- [102] Stoller R.E., Toloczko M.B., Was G.S., Certain A.G., Dwaraknath S., Garner F.A., On the use of SRIM for computing radiation damage exposure, *Nucl. Instruments Methods Phys. Res. Sect. B Beam Interact. with Mater. Atoms*, (2013), **310**, 75–80
- [103] Minosresearch A., Saclay C.E.A., European J.H.R., Cadarache C.E.A., JANNuS Saclay irradiation platform, (2019), 7–8
- [104] Toualbi L., Cayron C., Olier P., Logé R., De Carlan Y., Relationships between mechanical behavior and microstructural evolutions in Fe 9Cr-ODS during the

- fabrication route of SFR cladding tubes, *J. Nucl. Mater.*, (2013), **442**, 410–416
- [105] Jonas T.U. and J.J., Modeling Texture Change during the Recrystallization of an IF Steel, *ISIJ Int.*, (1994), **34**, 435–442
- [106] Bocos J.L., Novillo E., Petite M.M., Iza-Mendia A., Gutierrez I., Aspects of orientation-dependent grain growth in extra-low carbon and interstitial-free steels during continuous annealing, *Metall. Mater. Trans. A Phys. Metall. Mater. Sci.*, (2003), **34**, 827–839
- [107] Jonas J.J., Kestens L., Modelling the effects of nucleation and growth on texture formation in commercial steels, *Mater. Sci. Forum*, (1996), **204–206**, 155–168
- [108] Jirou B., Shimizu R., Distribution of {110}001 Oriented Grains in the Primary Recrystallized 3% Si-Fe Alloy CSL, (1988), **29**, 388–398
- [109] Ushigami Y., Kubota T., Takahashi N., Mechanism of Orientation Selectivity of Secondary Recrystallization in Fe-3%Si Alloy, *ISIJ Int.*, (1998), **38**, 553–558
- [110] Hayakawa Y., Szipunar J.A., A new model of Goss texture development during secondary recrystallization of electrical steel, *Acta Mater.*, (1997), **45**, 4713–4720
- [111] Hayakawa Y., Szipunar J.A., The role of grain boundary character distribution in secondary recrystallization of electrical steels, *Acta Mater.*, (1997), **45**, 1285–1295
- [112] Oxford Instruments HKL, Channel 5, (2007), 475
- [113] Nursalam, 2016 metode penelitian, Materials Issues for Generation IV Systems, (2013)
- [114] Kim T.K., Noh S., Kang S.H., Park J.J., Jin H.J., Lee M.K., Jang J., Rhee C.K., Current Status and Future Prospective of Advanced Radiation Resistant Oxide Dispersion Strengthened Steel (ARROS) Development for Nuclear Reactor System Applications, *Nucl. Eng. Technol.*, (2016), **48**, 572–594
- [115] Yang, No Title, *J. NanomedNanotechol*, (2013), **4**
- [116] Titorov D.B., Orientational relationship between the textured matrix in the alloy Fe-3% Si, and grains growing into it, *Phys Met Met.*, (1973), **35**, 165–168
- [117] Titorov D.B., Prediction of recrystallization texture, *Phys Met Met.*, (1973), **36**, 82–87
- [118] Leng B., Ukai S., Sugino Y., Tang Q., Narita T., Hayashi S., Wan F., Ohtsuka S., Kaito T., Recrystallization texture of cold-rolled oxide dispersion strengthened ferritic steel, *ISIJ Int.*, (2011), **51**, 951–957
- [119] Dillamore I.L., Katoh H., The Mechanisms of Recrystallization in Cubic Metals with Particular Reference to Their Orientation-Dependence, *Met. Sci.*, (1974), **8**, 73–83
- [120] Every R.L., Hatherly M., Oriented Nucleation in Low-Carbon Steels., *Texture*, (1974), **1**, 183–194
- [121] Kim S.W., Shobu T., Ohtsuka S., Kaito T., Inoue M., Ohnuma M., Kinetic approach for growth and coalescence of nano-size oxide particles in 9Cr-ODS steel using high-energy synchrotron radiation X-rays in SPring-8, *Mater. Trans.*, (2009), **50**, 917–921
- [122] Ukai S., Kaito T., Ohtsuka S., Narita T., Fujiwara M., Kobayashi T., Production and

- Properties of Nano-scale Oxide Dispersion Strengthened (ODS) 9Cr Martensitic Steel Claddings, *ISIJ Int.*, (2003), **43**, 2038–2045
- [123] Ukai S., Mizuta S., Fujiwara M., Okuda T., Kobayashi T., Development of 9cr-ods martensitic steel claddings for fuel pins by means of ferrite to austenite phase transformation, *J. Nucl. Sci. Technol.*, (2002), **39**, 778–788
- [124] Hsiung L., Fluss M., Tumey S., Kuntz J., El-Dasher B., Wall M., Choi B., Kimura A., Willaime F., Serruys Y., HRTEM study of oxide nanoparticles in K3-ODS ferritic steel developed for radiation tolerance, *J. Nucl. Mater.*, (2011), **409**, 72–79
- [125] Chen J., Jung P., Hoffelner W., Ullmaier H., Dislocation loops and bubbles in oxide dispersion strengthened ferritic steel after helium implantation under stress, *Acta Mater.*, (2008), **56**, 250–258
- [126] Hayashi T., Sarosi P.M., Schneibel J.H., Mills M.J., Creep response and deformation processes in nanocluster-strengthened ferritic steels, *Acta Mater.*, (2008), **56**, 1407–1416
- [127] Häussler D., Bartsch M., Messerschmidt U., Reppich B., HVTEM in situ observations of dislocation motion in the oxide dispersion strengthened superalloy MA 754, *Acta Mater.*, (2001), **49**, 3647–3657
- [128] Kimura Y., Takaki S., Suejima S., Uemori R., Tamehiro H., Ultra Grain Refining and Decomposition of Oxide during Super-heavy Deformation in Oxide Dispersion Ferritic Stainless Steel Powder, *ISIJ Int.*, (1999), **39**, 176–182
- [129] Dai L., Liu Y., Dong Z., Size and structure evolution of yttria in ODS ferritic alloy powder during mechanical milling and subsequent annealing, *Powder Technol.*, (2012), **217**, 281–287
- [130] Couvrat M., Chaffron L., Nunes D., Bonnaillie P., Mathon M.H., Perrut M., Microstructure evolution of mechanically alloyed ODS ferritic steels during hot extrusion, *Solid State Phenom.*, (2011), **172–174**, 721–726
- [131] Miller M.K., Hoelzer D.T., Kenik E.A., Russell K.F., Nanometer scale precipitation in ferritic MA/ODS alloy MA957, *J. Nucl. Mater.*, (2004), **329–333**, 338–341
- [132] Alinger M.J., Odette G.R., Hoelzer D.T., On the role of alloy composition and processing parameters in nanocluster formation and dispersion strengthening in nanostructured ferritic alloys, *Acta Mater.*, (2009), **57**, 392–406
- [133] Ukai S., Ohtsuka S., Nano-mesoscopic structure control in 9Cr-ODS ferritic steels, *Energy Mater.*, (2007), **2**, 26–35
- [134] Odette G.R., Hoelzer D.T., Irradiation-tolerant nanostructured ferritic alloys: Transforming helium from a liability to an asset, *Jom*, (2010), **62**, 84–92
- [135] Odette G.R., Miao P., Edwards D.J., Yamamoto T., Kurtz R.J., Tanigawa H., Helium transport, fate and management in nanostructured ferritic alloys: In situ helium implanter studies, *J. Nucl. Mater.*, (2011), **417**, 1001–1004
- [136] Robertson C., Panigrahi B.K., Balaji S., Kataria S., Serruys Y., Mathon M.H., Sundar C.S., Particle stability in model ODS steel irradiated up to 100 dpa at 600°C: TEM and nano-indentation investigation, *J. Nucl. Mater.*, (2012), **426**, 240–246
- [137] Skandan G., Foster C.M., Frase H., Ali M.N., Parker J.C., Hahn H., Phase characterization and stabilization due to grain size effects of nanostructured Y₂O₃,

- Nanostructured Mater.*, (1992), **1**, 313–322
- [138] Ratti M., Leuvre D., Mathon M.H., de Carlan Y., Influence of titanium on nano-cluster (Y, Ti, O) stability in ODS ferritic materials, *J. Nucl. Mater.*, (2009), **386–388**, 540–543
- [139] Claisse A., Ab Initio based Multi-Scale Simulations of Oxide Dispersion Strengthened Steels, KTH VETENSKAP OCH KONST, (2012)
- [140] De Castro V., Marquis E.A., Lozano-Perez S., Pareja R., Jenkins M.L., Stability of nanoscale secondary phases in an oxide dispersion strengthened Fe-12Cr alloy, *Acta Mater.*, (2011), **59**, 3927–3936
- [141] T. B. Massalski, H. Okamoto, P. R. Subramanian L.K., Binary Alloy Phase Diagrams, 2nd Edition (3 Volume Set), *Materials Park, Ohio : ASM International*, ©1990., (1990)
- [142] Pauling L., Shappell M.D., 8. The Crystal Structure of Bixbyite and the C-Modification of the Sesquioxides, *Zeitschrift Für Krist. - Cryst. Mater.*, (2015), **75**
- [143] Guo B., Luo Z.P., Particle size effect on the crystal structure of Y₂O₃ particles formed in a flame aerosol process, *J. Am. Ceram. Soc.*, (2008), **91**, 1653–1658
- [144] Chang W., Cosandey F., Hahn H., Electron microscopy studies of phase transformations in nanostructured Yttriumoxide, *Nanostructured Mater.*, (1993), **2**, 29–35
- [145] London A.J., Santra S., Amirthapandian S., Panigrahi B.K., Sarguna R.M., Balaji S., Vijay R., Sundar C.S., Lozano-Perez S., Grovenor C.R.M., Effect of Ti and Cr on dispersion, structure and composition of oxide nano-particles in model ODS alloys, *Acta Mater.*, (2015), **97**, 223–233
- [146] M. Yamamoto, S. Ukai S.H., Formation of Residual Ferrite in 9Cr-ODS Ferritic Steels, *Mater. Sci. Eng. A*, (2010), **527**, 4418
- [147] Kim S., Ohtsuka S., Kaito T., Yamashita S., Inoue M., Asayama T., Shobu T., Formation of nano-size oxide particles and δ -ferrite at elevated temperature in 9Cr-ODS steel, *J. Nucl. Mater.*, (2011), **417**, 209–212
- [148] Yazawa Y., Furuhashi T., Maki T., Effect of matrix recrystallization on morphology, crystallography and coarsening behavior of vanadium carbide in austenite, *Acta Mater.*, (2004), **52**, 3727–3736
- [149] Klueh R.L., Harries D.R., High-Chromium Ferritic and Martensitic Steels for Nuclear Applications: Monograph 3, *American Society for Testing and Materials, U.S.A.*, (2001)
- [150] Klueh R.L., Gelles D.S., Jitsukawa S., Kimura A., Odette G.R., Van der Schaaf B., Victoria M., Ferritic/martensitic steels - Overview of recent results, *J. Nucl. Mater.*, (2002), **307–311**, 455–465
- [151] Santra S., Amirthapandian S., Balaji S., Panigrahi B.K., Serruys Y., Robertson C., Ion irradiation stability of oxide nano-particles in ODS alloys: TEM studies, *J. Nucl. Mater.*, (2020), **528**, 151861
- [152] Lindau R., Möslang A., Schirra M., Schlossmacher P., Klimenkov M., Mechanical and microstructural properties of a hiped RAFM ODS-steel, *J. Nucl. Mater.*, (2002), **307–311**, 769–772

- [153] Pasebani S., Charit I., Burns J., Alsagabi S., Butt D.P., Cole J.I., Price L.M., Shao L., Microstructural stability of a self-ion irradiated lanthana-bearing nanostructured ferritic steel, *J. Nucl. Mater.*, (2015), **462**, 191–204
- [154] Barnard L., Odette G.R., Szlufarska I., Morgan D., An ab initio study of Ti-Y-O nanocluster energetics in nanostructured ferritic alloys, *Acta Mater.*, (2012), **60**, 935–947
- [155] He J., Wan F., Sridharan K., Allen T.R., Certain A., Shutthanandan V., Wu Y.Q., Stability of nanoclusters in 14YWT oxide dispersion strengthened steel under heavy ion-irradiation by atom probe tomography, *J. Nucl. Mater.*, (2014), **455**, 41–45
- [156] Certain A.G., Field K.G., Allen T.R., Miller M.K., Bentley J., Busby J.T., Response of nanoclusters in a 9Cr ODS steel to 1 dpa, 525 °C proton irradiation, *J. Nucl. Mater.*, (2010), **407**, 2–9
- [157] Liu C., Yu C., Hashimoto N., Ohnuki S., Ando M., Shiba K., Jitsukawa S., Microstructure and micro-hardness of ODS steels after ion irradiation, *J. Nucl. Mater.*, (2011), **417**, 270–273
- [158] Hin C., Wirth B.D., Formation of Y₂O₃ nanoclusters in nano-structured ferritic alloys: Modeling of precipitation kinetics and yield strength, *J. Nucl. Mater.*, (2010), **402**, 30–37
- [159] Ribis J., Lozano-Perez S., Nano-cluster stability following neutron irradiation in MA957 oxide dispersion strengthened material, *J. Nucl. Mater.*, (2014), **444**, 314–322
- [160] Rogozhkin S. V., Aleev A.A., Zaluzhnyi A.G., Nikitin A.A., Iskandarov N.A., Vladimirov P., Lindau R., Möslang A., Atom probe characterization of nano-scaled features in irradiated ODS Eurofer steel, *J. Nucl. Mater.*, (2011), **409**, 94–99
- [161] Pareige P., Miller M.K., Stoller R.E., Hoelzer D.T., Cadel E., Radiguet B., Stability of nanometer-sized oxide clusters in mechanically-alloyed steel under ion-induced displacement cascade damage conditions, *J. Nucl. Mater.*, (2007), **360**, 136–142
- [162] Yutani K., Kasada R., Kishimoto H., Kimura A., Irradiation hardening and microstructure evolution of ion-irradiated ODS ferritic steels, *J. ASTM Int.*, (2007), **4**, 2–4
- [163] Kimura A., Cho H.S., Toda N., Kasada R., Yutani K., Kishimoto H., Iwata N., Ukai S., Fujiwara M., High Burnup Fuel Cladding Materials R and D for Advanced Nuclear Systems, *J. Nucl. Sci. Technol.*, (2007), **44**, 323–328
- [164] Kishimoto H., Kasada R., Hashitomi O., Kimura A., Stability of Y-Ti complex oxides in Fe-16Cr-0.1Ti ODS ferritic steel before and after heavy-ion irradiation, *J. Nucl. Mater.*, (2009), **386–388**, 533–536
- [165] Kishimoto H., Yutani K., Kasada R., Hashitomi O., Kimura A., Heavy-ion irradiation effects on the morphology of complex oxide particles in oxide dispersion strengthened ferritic steels, *J. Nucl. Mater.*, (2007), **367–370 A**, 179–184
- [166] Ribis J., Bordas E., Trocellier P., Serruys Y., De Carlan Y., Legris A., Comparison of the neutron and ion irradiation response of nano-oxides in oxide dispersion strengthened materials, *J. Mater. Res.*, (2015), **30**, 2210–2221
- [167] Ziegler J.F., Biersack J.P., SRIM-2008, Stopping Power and Range of Ions in Matter, *Nucl. Instrum. Methods*, (2008), **268**, 1818–1823

- [168] Akasaka N., Yamashita S., Yoshitake T., Ukai S., Kimura A., Microstructural changes of neutron irradiated ODS ferritic and martensitic steels, *J. Nucl. Mater.*, (2004), **329–333**, 1053–1056
- [169] S. Rogozhkin, A. Bogachev, O. Korchuganova, A. Nikitin, N. Orlov, A. Aleev, A. zaluzhnyi, M. Kozodaev, T. Kulevov, B. chalykh, Lindau R., Hoffmann J., Möslang A., Vladimirov P., Klimenkov M., Heilmaier M., Wagner J., Seils S., Kulevoy T., Chalykh B., Nanostructure evolution in ODS steels under ion irradiation, *Nucl. Mater. Energy*, (2016), **9**, 66–74
- [170] Yamashita S., Oka K., Ohnuki S., Akasaka N., Ukai S., Phase stability of oxide dispersion-strengthened ferritic steels in neutron irradiation, *J. Nucl. Mater.*, (2002), **307–311**, 283–288
- [171] P. Dubuisson R. schill, Effects of radiation on materials: 20th international symposium, *18th Int. Symp. ASTM STP*, (1999), **1325**, 882
- [172] Monnet I., Dubuisson P., Serruys Y., Ruault M.O., Kaïtasov O., Jouffrey B., Microstructural investigation of the stability under irradiation of oxide dispersion strengthened ferritic steels, *J. Nucl. Mater.*, (2004), **335**, 311–321
- [173] Oka K., Ohnuki S., Yamashita S., Akasaka N., Ohtsuka S., Tanigawa H., Structure of nano-size oxides in ODS steels and its stability under electron irradiation, *Mater. Trans.*, (2007), **48**, 2563–2566
- [174] Šćepanović M., de Castro V., Leguey T., Auger M.A., Lozano-Perez S., Pareja R., Microstructural stability of ODS Fe–14Cr (–2W–0.3Ti) steels after simultaneous triple irradiation, *Nucl. Mater. Energy*, (2016), **9**, 490–495
- [175] Lu C., Lu Z., Wang X., Xie R., Li Z., Higgins M., Liu C., Gao F., Wang L., Enhanced Radiation-tolerant Oxide Dispersion Strengthened Steel and its Microstructure Evolution under Helium-implantation and Heavy-ion Irradiation, *Sci. Rep.*, (2017), **7**, 1–7
- [176] Yano K.H., Swenson M.J., Wu Y., Wharry J.P., TEM in situ micropillar compression tests of ion irradiated oxide dispersion strengthened alloy, *J. Nucl. Mater.*, (2017), **483**, 107–120
- [177] Zhanbing Y., Benfu H., Kinoshita H., Takahashi H., Watanabe S., Effect of hydrogen ion/electron dual-beam irradiation on microstructural damage of a 12Cr-ODS ferrite steel, *J. Nucl. Mater.*, (2010), **398**, 81–86
- [178] Wharry J.P., Swenson M.J., Yano K.H., A review of the irradiation evolution of dispersed oxide nanoparticles in the b.c.c. Fe-Cr system: Current understanding and future directions, *J. Nucl. Mater.*, (2017), **486**, 11–20
- [179] Kondo K., Aoki S., Yamashita S., Ukai S., Sakamoto K., Hirai M., Kimura A., Ion irradiation effects on FeCrAl-ODS ferritic steel, *Nucl. Mater. Energy*, (2018), **15**, 13–16
- [180] Zinkle S.J., Matsukawa Y., Observation and analysis of defect cluster production and interactions with dislocations, *J. Nucl. Mater.*, (2004), **329–333**, 88–96
- [181] Deo C., Tomé C., Lebensohn R., Maloy S., Modeling and simulation of irradiation hardening in structural ferritic steels for advanced nuclear reactors, *J. Nucl. Mater.*, (2008), **377**, 136–140
- [182] Busby J.T., Hash M.C., Was G.S., The relationship between hardness and yield

- stress in irradiated austenitic and ferritic steels, *J. Nucl. Mater.*, (2005), **336**, 267–278
- [183] Rehtin M.D., Wiedersich H., Effects of ion bombardment at high temperature on the microstructure of Y₂O₃, *Radiat. Eff.*, (1977), **31**, 181–184
- [184] Zinkle S.J., Kinoshita C., Defect production in ceramics, *J. Nucl. Mater.*, (1997), **251**, 200–217
- [185] Setyawan W., Selby A.P., Juslin N., Stoller R.E., Wirth B.D., Kurtz R.J., Cascade morphology transition in bcc metals, *J. Phys. Condens. Matter*, (2015), **27**, 225402
- [186] Mohan S., Kaur G., Panigrahi B.K., David C., Amarendra G., Effect of Zr and Al addition on nanocluster formation in oxide dispersion strengthened steel - An ab initio study, *J. Alloys Compd.*, (2018), **767**, 122–130